XUV Diagnostics Tailored to Resolve Short-Pulse-Laser-Driven Ultrafast Plasma Dynamics

Dissertation

zur Erlangung des akademischen Grades
Doctor rerum naturalium (Dr. rer. nat.)

vorgelegt dem Rat der
Physikalisch-Astronomischen Fakultät
der Friedrich-Schiller-Universität Jena

eingereicht von
Herr Dipl.-Phys. Vinzenz Johannes Hilbert
geboren am 07.09.1982 in Friedrichroda

1. Dezember 2016

Gutachter

1. **Prof. Dr. Eckart Förster**
   Institut für Optik und Quantenelektronik
   Friedrich-Schiller-Universität Jena

2. **Prof. Dr. Georg Pretzler**
   Laser- und Plasmaphysik
   Universtät Düsseldorf

3. **Prof. Dr. Thomas Wilhein**
   Institute for X-Optics
   RheinAhrCampus Remagen

Tag der öffentlichen Verteidigung: 09. März 2017

Abstract

With the advent of free-electron lasers (FEL), such as the **F**ree-electron **LAS**er in **H**amburg (FLASH) in 2005 and the **L**inac **C**oherent **L**ight **S**ource (LCLS) in 2009, the research of matter under extreme conditions has experienced a substantial boost. Using such large-scale facilities or others, it is now possible to generate and investigate plasmas from liquid density up to solid density with unprecedented accuracy. Such plasmas are found for example in Jupiter-like planets, the Earth's core or in brown dwarfs. Photons in the extreme ultraviolet (XUV) range are of particular interest since they penetrate solid density and thereby contribute to the exploration of the plasma interior. Thus, important information on energy transport and exchange between electrons and ions in plasmas can be obtained. Furthermore, predictions from simulations can be benchmarked experimentally and the applicability of different fundamental models can be tested. Also, due to its spatial and temporal coherence properties FEL radiation is well suited for scattering and diffraction experiments. The high degree of coherence suggests the use of interferometric methods, which provide information on dielectric properties, such as the refractive index of dense matter. Beyond the use of XUV radiation as a tool to create and probe dense plasmas, it can also be observed in the self-emission of thermal plasmas, for example after excitation of a solid-state sample with an optical laser. Here, the spatially resolved analysis of spectral lines reveals information on density, temperature and spatial extent of the free-electron plasma. The aim of this work is the development and application of innovative instrumentation at free-electron lasers for the research of dense matter under extreme conditions and its interaction with intense laser fields. The instrumentation uses diffraction gratings, multilayer mirrors and multilayer beam splitters and is focused in particular on experiments at FELs, regarding the source size and the expected signal and repetition rates. For discovery-class experiments at large-scale facilities like synchrotrons or FELs, the experimental setup and the procedure is individually adapted to the local conditions. When using several devices simultaneously these are calibrated with respect to each other. Optically relevant subcomponents of such custom-designed instruments are properly characterized and extensively calibrated beforehand.

Zusammenfassung

Mit der Entwicklung Freier-Elektronen-Laser (FEL), wie FLASH (**F**reie Elektronen **LAS**er in **H**amburg) seit 2005 oder LCLS (**L**inac **C**oherent **L**ight **S**ource) seit 2009, die im Röntgen und extrem ultravioletten Bereich (XUV) arbeiten, erlebte die Erforschung von Materie unter extremen Bedingungen einen besonderen Schub. Mit Hilfe solcher und anderer Großforschungsanlagen ist es nun möglich, Plasmen mit Flüssigkeitsdichte beziehungsweise bis über Festkörperdichte hinaus zu erzeugen und mit bisher unerreichter Genauigkeit zu untersuchen. Solche Plasmen kommen beispielsweise in jupiterähnlichen Planeten, im Erdkern oder in brauen Zwergen vor. Photonen im XUV kommt dabei eine besondere Bedeutung zu, da sie in der Lage sind, dichte Plasmen zu durchdringen und so zur Erforschung des Plasmainneren beitragen können. Somit werden wichtige Erkenntnisse über Energietransport und -austausch zwischen Elektronen und Ionen in Plasmen gewonnen. Außerdem lassen sich Voraussagen von Simulationen experimentell überprüfen und die Anwendbarkeit verschiedener Grundmodelle testen. Neben der Anwendung von XUV Strahlung zur Erzeugung dichter Plasmen kann diese auch in Emission angeregter Plasmen beobachtet werden, beispielsweise nach Anregung eines Festkörpers mit einem optischen Laser. Die ortsaufgelöste Analyse der Spektrallinien gewährt Aufschluss über Dichte, Temperatur und räumliche Ausdehnung des freien Elektronen Plasmas. Auch aufgrund seiner räumlichen und zeitlichen Kohärenzeigenschaften ist FEL Strahlung gut geeignet für Streu- und Beugungsexperimente. Die hohe Kohärenz erlaubt zudem den Einsatz interferometrischer Methoden, welche Aufschluss über dielektrische Eigenschaften, wie beispielsweise den Brechungsindex dichter Materie geben können.

Ziel dieser Arbeit ist die Entwicklung und Anwendung innovativer Instrumentierung an FELs zur Erforschung von dichter Materie unter extremen Bedingungen und ihre Wechselwirkung mit intensiven Laserfeldern. Die Instrumentierung mit Beugungsgittern, Vielschicht-Spiegeln und Vielschicht-Strahlteilern wird dabei speziell auf Experimente an XUV FELs abgestimmt, insbesondere mit Rücksicht auf Quellgröße und zu erwartende Signal- und Repetitionsraten. In dieser Arbeit wird

beschrieben, wie der experimentelle Aufbau und die Vorgehensweise für neuartige Grundlagenexperimente an Großforschungsanlagen an die Gegebenheiten vor Ort angepasst werden kann. Bei eventuellem Einsatz mehrerer Geräte werden diese miteinander abgeglichen. Die optisch relevanten Einzelteile solcher maßgeschneiderten Aufbauten werden dafür zunächst umfassend charakterisiert und kalibriert.

Contents

1 Motivation and Structure **4**

2 Fundamentals of XUV Optics **9**

2.1 Refractive Index and Dispersion 9

2.2 Sources of XUV Radiation 14

2.2.1 Laboratory XUV Tube 14

2.2.2 Laser-Plasma Sources 15

2.2.3 Synchrotron and Undulator Radiation 15

2.2.4 High-Gain FELs 17

2.2.5 High Harmonics of Lasers 18

3 Design and Characterization of an XUV Spectrometer **19**

3.1 Motivation 19

3.2 Overall Scheme and Spectrometer Design 20

3.3 The Variable Line Space Diffraction Grating 21

3.4 Collection Mirror Setup 25

3.5 Design Parameters and Technical Implementation 28

3.6 Focal Point and Virtual Source 31

3.7 Measurement and Calibration 33

4 XUV Spectrometry of Plasmas **40**

4.1 Multi Angle Spectroscopy of a Laser Generated Al Plasma 40

4.2 Simultaneous Multi-Angle XUV Spectroscopy 45

4.2.1 Experimental Procedure 45
4.2.2 Summary of the Section 54
4.3 Determination of Free Electron Temperature from XUV – Bremsstrahlung Spectroscopy 57
4.3.1 Setup and Experiment 57
4.3.2 Experimental Results 59
4.3.3 Comparison to Simulations 61
4.4 Equilibration Dynamics and Conductivity of Warm Dense Hydrogen . 64
4.4.1 Setup and Experiment 64
4.4.2 Experimental Results 65
4.4.3 Interpretation of the Data 66
4.5 Summary of the Spectrometry Chapter 68

5 A Multi-Angle XUV Diode Array 70
5.1 Description of Individual Parts and Geometry 70
5.2 Calibration 72
5.3 A Pump – Probe Experiment Using the Diode Array 73

6 XUV Interferometry 75
6.1 An XUV Michelson Interferometer 75
6.1.1 Basic Interferometer Concept 75
6.1.2 Interferometer Setup 77
6.1.3 Experimental Proof of Principle 79
6.1.4 Membrane Surface Curvature 81
6.1.5 Potential Applications at XUV FELs 82
6.2 Coherence of the Free Electron Laser FLASH 86
6.2.1 Setup at the Free Electron Laser 87
6.2.2 Static Piezos – Correlation VIS-STD 88
6.2.3 Temporal and Spatial Coherence 90
6.3 Summary of the Interferometry Chapter 93

7 Conclusion and Outlook 95

Bibliography **98**

Ehrenwörtliche Erklärung **110**

Danksagung **111**

1. Motivation and Structure

The investigation of dense plasma is a diverse field of research which offers insight into the physics of stars and planets [1; 2]. To study these astrophysical objects theoretically, so-called ab initio methods were developed amongst others, that simulate the extreme conditions and processes at these distant objects [3]. Nevertheless, there are still blank spots on this extraordinary field of science, which can only be filled by combination of different fields of research such as laser plasma physics, astrophysics, and high pressure physics. Simulations need benchmarking with experimental results. Besides the static equation of state, special attention is drawn to dynamical properties like thermal and electrical conductivity, and ionization and recombination dynamics, which are mostly known for some pure substances like hydrogen, helium, carbon, aluminum or water, but are also important for mixtures when it comes to extraterrestrial objects or even the Earth's core [4; 5].

Along with the advent of free-electron lasers (FELs) in the last decade a whole new field of research emerged [6; 7] in the wavelength range of 4–40 nm, which is called the extreme ultraviolet (XUV). In parallel, the development and improvement of dedicated instruments which are sensitive to this wavelength range and are applicable at the specific beamlines was promoted [8; 9]. FEL pulses are ultra short in time ($\lesssim 300$ fs) and can be provided at a comparatively high repetition rate, while they bear an unprecedented ultrahigh brilliance [6].

Using FELs as diagnostic tools, x-ray scattering techniques can be used to examine warm dense matter (WDM) dynamics on nanosecond [10; 11] and picosecond time scales [12]. To achieve this, pump-probe experiments are carried out, where a first pulse excites matter into a plasma state, which is afterwards probed via a

second pulse. The time delay between the pulses is well defined and can be as short as a few ten femtoseconds [13]. Volumetric heating via XUV-photons allows for the preparation of a homogeneously heated dense sample [14; 15]. A comparable uniformity and time resolution cannot be reached with an optical laser as the driving source for the heating process, because solid density is optically thick for visible light [16; 17]. Observation of scattering properties in time allows for determination of plasma parameters and thus reveals insight into thermodynamic properties. This is particularly interesting for matter under extreme conditions to model, for example, the interior of planets and stars [18], as well as for inertial confinement fusion experiments [19]. Currently, the modeling of those systems is hampered by the limited knowledge about transport properties and equilibration dynamics. To overcome these problems, sub picosecond probing of a uniformly heated sample is necessary. This allows for determination of equilibration and collision times between electrons and ions, i.e. dynamic properties of matter which are closely connected to thermal and electrical conductivity, as well as reflectivity. On a larger scale the depth of mixing layers of Jovian planets are effected [20], and furthermore the assembly of a stable thermonuclear fuel layer in ICF implosions [21; 22]. To determine these parameters the response of a strongly pumped system needs to be probed with high temporal resolution.

FEL experiments exploiting high energy density states can give valuable information and help to determine the correct equation of states for hydrodynamic simulations. They can provide reference points to validate ionization models for WDM states. Comparing experimental results to results from hydrodynamic simulations allows for the determination of plasma temperatures with a single- and two-temperature approach and consequently for the calculation of the structure factor for x-ray scattering. The combination of molecular dynamic simulation and two-temperature density functional theory ultimately provides information about conductivity models for partially ionized plasmas.

In order to perform scattering experiments at XUV wavelengths with a sufficiently high signal level, spectrometers, optics, dispersive elements, and detectors with a

typical collection efficiency $> 10^{-6}$ and highly brilliant XUV sources such as FELs are needed. The reason for this lies in the comparatively low scattering fraction in the order of 10^{-6} in a typical solid density plasma sample of a few $10^3\,\mu\mathrm{m}^3$ and in a small Thomson scattering cross section of the electrons. Thus, along with the development of novel XUV sources during the last years, the field of efficient XUV sensitive instrumentation has also prospered. Especially, the lithographically relevant wavelength of $\lambda = 13.5\,\mathrm{nm}$ has drawn the attraction of design engineers and developers of XUV sources and optics [23]. In contrary to spectrometers in the visible regime, XUV spectrometers have to be vacuum compatible, which poses an extra challenge to the technical design. Moreover, the use of either total external reflection optics, which will work only for low deflection angles or the application of multilayer-coated substrates that support only a narrow bandwidth call for technical solutions that adapt to the specific experimental conditions.

Another approach to access the parameter space of a dense plasma in the laboratory is the heating of a liquid or solid state target via optical lasers. Nonetheless, a detailed description of the interaction between laser and matter is complicated since it is highly nonlinear. This particularly complicates the calculation of plasma parameters such as density and temperature on short time scales $< 10\,\mathrm{ps}$, from a laser-generated plasma. In these high intensity regimes, free electrons in the skin depth are accelerated within the laser field. The inner part of the target is heated via impact ionization [24; 25]. It is a challenging task to model the non linear absorption of optical lasers and solid or liquid targets in hydrodynamic simulations. Benchmarking experiments that experimentally determine the temperature of the plasma are desperately needed. In such experiments spectroscopic analysis of the emission lines classically allows to determine both the plasma temperature and ion abundance from the line ratios. In order not to be limited to surface diagnostics of the partially ionized, degenerated plasma, spectroscopy in the XUV range is the favorable choice. This relevant effect supports the understanding of laser generated plasmas on sub-picosecond time scales [26; 27], as well as the excitation of clusters [28; 29].

In addition to the high intensity and brilliance on ultrashort time scales FEL radiation is coherent in time and space [30; 31; 32]. Consequently, it can be used in interferometric experiments and for single particle coherent diffraction experiments [33; 34]. In this content, diffraction experiments can help to examine the inner structure of single particles and also non-crystalline matter. Valuable contributions to the subjects of XUV-imaging, holography, and microscopy can be expected [35].

Interferometric methods applied at coherent XUV sources could shed light upon dielectric properties of solid density matter [36]. Particularly, the determination of the refractive index n is a challenging task since it is typically close to unity in the XUV spectral range. Interferometric methods employing coherent XUV radiation can for example be applied at dense plasmas for a time-resolved measurement of the refractive index [33; 34]. Knowledge about the transport of radiation in warm dense matter and plasmas would be increased by such experiments. Along with that various fields like dense plasma, physics of planets, and inertial confinement fusion could profit from the insights.

For an estimation of the coherence properties of FEL radiation it should be noted that it is closely connected either to the self-amplified spontaneous emission (SASE) or the seeding process, which may start the lasing process. A significant difference between the spatio-temporal coherence properties of a monochromatized pulse and a pulse at full SASE bandwidth is expected, because of its composition of multiple spectral modes [37]. In addition to the aforementioned high resolution high throughput spectrometers, a Michelson interferometer can be attached routinely to an experiment to determine the coherence properties of the radiation [38]. Another possible application is the determination of the coherence properties of high harmonics, which serve frequently as an XUV source.

This work is structured as follows, chapter 2 serves as a theoretical introduction where selected fundamentals of XUV optics are described. Namely, the specifics of refractive index and dispersion in the XUV wavelength range are explained to achieve a better understanding of the requirements for dedicated optical instruments.

In chapter 3 a concept of a multi-angle scattering spectrometer is presented. After optimization of the design parameters in simulations and separate performance tests

of some optical components, the XUV-sensitive spectrometer is built, calibrated, and subject to spectral resolution tests.

The newly built spectrometer is then used in different configurations in various experiments, which are discussed in chapter 4. In a proof-of-principle experiment in chapter 4.1 the size of the laser generated plasma is determined employing the multi-angle spectrometer. A method for the in-situ cross calibration of several XUV spectrometers is presented in chapter 4.2. In chapter 4.3 I present results of an experiment where XUV spectroscopy of laser generated bremsstrahlung was used to determine the free electron temperature of the plasma. An XUV pump – XUV probe scattering experiment employing a liquid hydrogen target at an FEL is discussed in chapter 4.4.

Based on these findings the design of a multi angle diode array is presented in chapter 5. After calibration of the diodes, the array is installed at an FEL in a pump-probe experiment and its performance is reviewed.

In chapter 6 an XUV Michelson interferometer as a complementary diagnostic to the XUV spectrometer from the preceding sections is introduced. Specific requirements of the optical components and a comprehensive test at a synchrotron source is discussed in chapter 6.1. Simulations concerning the applicability at a free electron laser are carried out. In chapter 6.2 the interferometer is applied at an FEL to determine its coherence. Results are compared to theoretical predictions.

An overview of the main results of this work and their impact on current fields of research is concluded in chapter 7.

2. Fundamentals of XUV Optics

2.1 Refractive Index and Dispersion

This chapter follows the argumentation of references [39] and [40].

Extreme ultraviolet (XUV) radiation covers a broad wavelength range in the electromagnetic spectrum. There are various definitions of the exact energy range of the corresponding photons and often the borders are seamless. This work follows a commonly used definition of extreme ultraviolet light extending from photon energies of about 30 eV to 250 eV, or in wavelengths between 40 nm and 5 nm. XUV radiation as all kinds of electromagnetic radiation consists of photons with the energy $E = \frac{hc}{\lambda}$, with Planck's constant h. The vacuum wavelength λ and the angular frequency ω of such a photon are connected via $c = \lambda\frac{\omega}{2\pi}$, with c the speed of light in vacuum. XUV wavelengths play a relevant role in large scale industrial research since XUV lithography has become a candidate for the succession of photo lithography in the semiconductor industry. The production of microelectronic devices using wavelengths as short as 13.5 nm has taken place on the wish list of research and development departments during the last years. Due to comparatively high photon energies, XUV radiation is strongly absorbed by most of the solid state materials and therefore yields the potential for structural analysis with nm-resolution.

A closer look at the interaction between XUV photons and matter is required to understand the specific requirements for XUV optical devices such as mirrors, detectors, beam splitters, and others. The refractive index n is apparently one of the most important material properties when it comes to interaction between solid state materials and photons. It is a dimensionless material dependent number, that

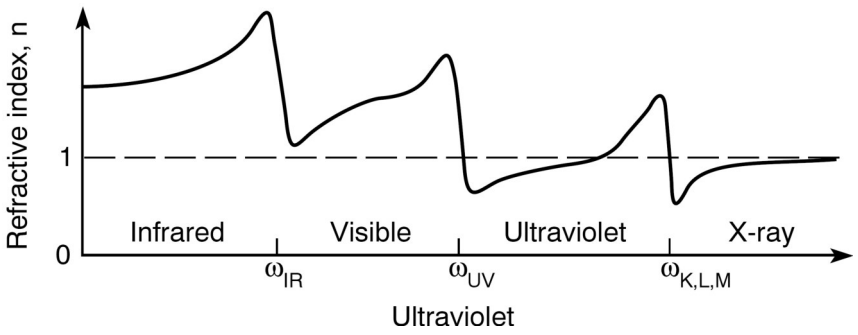

Figure 2.1: A sketch of the real part of the refractive index depending on the light frequency ω [39]. It shows that $n \approx 1$ in the region of XUV wavelengths

can be written as a complex number $n = n' + i\,n''$. Figure 2.1 shows a sketch of the real part n' of the refractive index for different photon frequencies. The frequency dependency of the refractive index shows that the real part is slightly smaller than unity in the XUV regime. Hence, the refractive index in the XUV is commonly written as

$$n(\omega) = 1 - \delta + i\beta. \tag{2.1}$$

Both δ and β in equation 2.1 are positive dimensionless numbers, where the coefficient β as the imaginary part describes the attenuation of light traveling through a medium. With this, the complex dispersion relation reads as

$$\frac{\omega}{k} = \frac{c}{n} = \frac{c}{1 - \delta + i\beta} \tag{2.2}$$

where k denotes the wave number.

To account for the frequency dependence, the refractive index is typically approximated as

$$n(\omega) = 1 - \frac{\omega_p^2}{2} \sum_s \frac{g_s}{(\omega^2 - \omega_s^2) + i\gamma\omega} \tag{2.3}$$

with the different resonance frequencies ω_s of the material, and a dissipative factor γ. The plasma frequency ω_p represents the quantity $\omega_p = \left(\frac{e^2 n_e}{\epsilon_0 m_e}\right)^{1/2}$ with the elementary charge e, the permittivity of the free space ϵ_0, and the electron density and mass, n_e and m_e. In equation 2.3 the term g_s denotes the so called *oscillator strength*, which in the semi-classical model can simply be understood as the num-

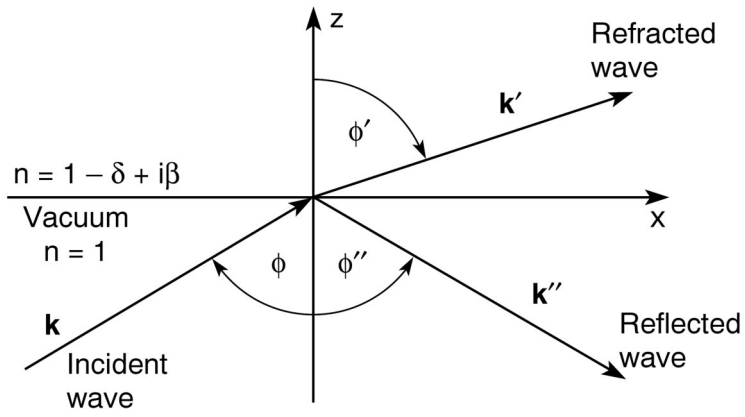

Figure 2.2: A sketch of the geometry for incident, refracted and reflected rays [39].

ber of electrons which are attributed to a certain resonance frequency ω_s. Due to its frequency dependency the refractive index is called *dispersive*, because waves of different frequencies will propagate at different velocities through the medium and disperse. For $\omega < \omega_s$ the term of normal or positive dispersion is used. We speak of anomalous or negative dispersion if $\omega > \omega_s$. In fig. 2.1 the characteristic steep slopes of the refractive index and the strong variations at the infrared (IR), the ultraviolet (UV), and the x-ray region mark different atomic resonances ω_s. At $\omega \approx \omega_s$, the dispersion changes from normal to anomalous dispersion. It should be mentioned that photons in the range of the atomic resonance frequencies ω_s are strongly absorbed by the material. In this spectral range, the photon energies are similar to binding energies of the electrons and therefore likely absorbed by the material. As a consequence, low penetration depths are stated.

In comparison to the visible wavelength range, reflection optics in the XUV exhibit typically a much lower reflectivity. This problem can be encountered by the use of multilayer optics or grazing incidence optics. In case of the latter, the mechanism of total external reflection is used to achieve an adequate reflectivity. Figure 2.2 shows a scheme of an interface, where reflection and refraction takes place. The angle of the incident wave Φ is measured from the z-axis, the surface normal. Snell's law describes the behavior of a wave at the interface of two isotropic media, each

with a complex refractive index as follows

$$\frac{\sin\Phi'}{n_{vac}} = \frac{\sin\Phi''}{n_{vac}} = \frac{\sin\Phi}{n}\,. \tag{2.4}$$

With the fact that $n_{vac} = 1$ for all wavelengths, the first information from equation 2.4 is that incident and reflected angles Φ and Φ'' are equal. Moreover, together with equation 2.2 the absolute value of the wavevector $\mathbf{k}$ in vacuum amounts to

$$k = |\mathbf{k}'| = |\mathbf{k}''| = \frac{\omega}{c}\,. \tag{2.5}$$

For a closer look at the incidence angle of total external reflection, I will assume that β in equation 2.1 is close to zero, i.e. absorption is neglected, and Snell's law simplifies to

$$\sin\Phi' = \frac{\sin\Phi}{1-\delta} \tag{2.6}$$

Since $\delta > 0$, for Φ close to $\pi/2$, the refracted angle Φ' approaches the value of $90\,^\circ$ faster than the incidence angle. For the critical incidence angle $\Phi_c = \Phi$, where the refraction angle reaches $\Phi' = 90\,^\circ$ and $\sin\Phi' = 1$

$$\sin\Phi_c = 1 - \delta \tag{2.7}$$

is obtained. In this case the refracted wave no longer propagates through the medium, but rather along the surface. For an interpretation of equation 2.7, it should be noted again that δ is very small and thus Φ_c is close to $90\,^\circ$. Introducing the complimentary angle θ with $\Phi + \theta = 90\,^\circ$, the critical angle can also be expressed by

$$\cos\theta_c = 1 - \delta\,. \tag{2.8}$$

The small angle approximation now leads to $1 - \frac{\theta_c^2}{2} + \ldots = 1 - \delta$ and finally to

$$\theta_c = \sqrt{2\delta}\,. \tag{2.9}$$

Following the description in reference [39] the dependency of the critical angle for

total external reflection on the real part of the index of refraction yields a proportionality of

$$\theta_c \propto \lambda\sqrt{Z} \tag{2.10}$$

with the atomic number Z. The interpretation of this relation is straight forward and shows that for a desired large critical angle a longer wavelength or a material with larger atomic number Z should be chosen. Substrates for XUV applications such as mirrors or gratings are therefore often coated with heavier elements such as gold. The need of low incidence angles for high reflectivity also results in comparably low collection solid angles for possible XUV experiments, such as plasma diagnostics as discussed in chapters 4.2, 4.3, 4.4.

Total external reflection optics reflect over a broad spectral range at moderate reflectivities. In the XUV regime total external reflection R is still well below unity due to strong absorption. For applications where high reflectivity under a desired angle is needed, the choice of multilayer optics comes into play. Furthermore, the spectral bandwidth can be well designed by the choice of suitable design parameters of the multilayer stack. During the manufacturing process of such a multilayer a periodical stack of layers is deposited on a substrate. If the substrate itself is transparent in the XUV range, the choice of the suitable amount of layers results in the construction of a beam splitter. The reflection of such a beam splitter depends on the design of the multilayer stack, whereas the transmission also includes the substrates or support foil transmission. For both mirrors and beam splitters an optical flatness of a fraction of the wavelength is needed. This flatness has to be maintained over the diameter of the beam. For the short XUV wavelengths this is a challenging task in the manufacturing process. An experiment to determine the optical flatness of an XUV beam splitter is described in chapter 6.1. Multilayer optical elements are also successfully used in an experiment that determines the coherence properties of an FEL in chapter 6.2.

2.2 Sources of XUV Radiation

Dependent on the application there is a variety of XUV sources that largely differ in photon flux, spectral bandwith, spatial and temporal coherence of the radiation, and possible pulse characteristics, i.e. duration, repetition rate, shape. The choice of a suitable XUV source for a specific purpose is governed by the experimental demands of the application and of course also by financial limitations and space constraints. Hereafter, I will present a few concepts of XUV sources that were also used for this work.

2.2.1 Laboratory XUV Tube

Compared to large scale XUV sources, such as synchrotrons and FEL, the laboratory XUV source is a compact sized instrument. It is basically a microfocus x-ray tube with a Silicon anode, that can easily be operated by one person in the laboratory. However, it provides only a small spectral bandwidth and low emittance compared to synchrotron sources and FELs. XUV radiation is created from electron bombardment of a solid target. In case of this work the target material is silicon, and thus the emitted spectrum follows the spectrum of silicon L-shell radiation ($L_{2,3}$) [41]. For Si L-shell radiation, the emission band reaches from 12.5 nm to 15 nm with a peak at 13.5 nm. To optimize the XUV photon flux, the current and the acceleration voltage for the electrons can be adjusted. Moreover, the electrons are focused via an electron lens to a spot size of $\approx 20\,\mu$m on the Si target, yielding a small source size and homogeneous emission in a radiation opening angle of $12\,^\circ$ and an emission power in the XUV emission band of $> 20\,\mu$W (2π sr, 2 % bw) [41].

A laboratory XUV tube as described here was used for the characterization of the XUV spectrometer in chapter 3.

2.2.2 Laser-Plasma Sources

To generate XUV radiation in a comparatively wide spectral window along with a hands-on table top setup, laser generated XUV sources can be the method of choice. For this approach, typically a high intensity ultra short pulse laser is focused onto a solid or gas target. Nonlinear processes like multiphoton absorption create a plasma state with moderate free electron densities. XUV radiation is then created from recombination of the electrons into deeper atomic shells or from bremsstrahlung of the free electrons. The emitted spectral shape strongly depends on the intensity and the wavelength of the incoming laser and the target material [15]. A point source will typically result in radiation emittance over a large solid angle. XUV radiation is not limited to optical or IR-laser driven plasmas, but can also be emitted by FEL generated plasmas [42].

Short-pulse IR-laser generated and FEL-generated XUV radiation is used to characterize different XUV spectrometers in chapter 3 and 4.2. Additionally, in chapter 4.1 the extend of a laser-generated aluminum plasma is determined from its XUV emission. XUV bremsstrahlung spectroscopy from laser-generated dense hydrogen plasma is used to determine the free-electron temperature in chapter 4.3.

2.2.3 Synchrotron and Undulator Radiation

If an electric charge is accelerated it will emit radiation. This fundamental effect is used in synchrotrons, where electrons are accelerated to relativistic speeds and then are slightly diverted from their path using single magnetic fields or periodically alternating magnetic fields. To account for the relativistic speed of the electron the relativistic factor γ is introduced

$$\gamma \equiv \frac{1}{\sqrt{1 - v^2/c^2}} \,, \tag{2.11}$$

with c the vacuum speed of light and v the speed of the electron. At relativistic speed the radiation will be emitted in a cone with opening angle of $1/\gamma = \theta$. Thus,

the faster the electron moves, the smaller will be the emission cone (*emittance angle*) and radiation will be emitted strongly in forward direction. Different designs of synchrotrons and their magnetic structures will result in different spectral and temporal properties of the created radiation. Bending magnets will create a uniform magnetic field and cause an electron movement on a sector of a circle. The emission can be compared in a simple way to a sweeping searchlight. Besides bending magnets, there is also the possibility to use periodically inverted magnetic fields to create synchrotron radiation. Two cases can be distinguished: A relatively weak alternating magnetic field will cause a harmonic oscillation of the relativistic electrons. The amplitude of the *undulation* of the electron is small. Due to coherent superposition of on-axis emission, the radiation can be tuned to exhibit a moderately low angular divergence and to be spectrally narrow. For strong magnetic fields, the electron oscillates with a much bigger amplitude along the *wigglers*, as the magnetic structures are called for this case, where there is no coherent superposition. Due to the creation of higher harmonics in wigglers, the created radiation displays higher photon energies than for an undulator. The radiation cone and the spectrum of a wiggler is similar to that of a bending magnet, but with a higher photon flux, due to the mentioned comb of high harmonics.

In contrast to wiggler radiation, the amplitude of the electron motion passing the magnetic field in an undulator should be small. If the angular excursion θ_e of the electrons meet the condition that $\theta < 1/2\gamma$ we speak of undulator radiation. The emitted wavelength λ depends not only on the period length of the magnet structure λ_u but also on the relativistic factor γ. In the reference frame of the moving electron a Lorentz contraction of the period length λ_u of the undulator can be stated as $\lambda' = \lambda_u/\gamma$. The moving electron will then oscillate on its path along the undulator and emit dipole radiation. Switching back to the laboratory frame the emitted wavelength is further decreased by Doppler shifting. Since the Doppler shift depends on relative velocities, it depends on the observation angle θ and the emitted wavelength amounts in first order to $\lambda = \frac{\lambda_u}{2\gamma^2}(1 + \gamma^2\theta^2)$. Note that off-axis radiation exhibits a slightly longer wavelength than the central parts of the radiation cone.

To obtain a suitable approximation for the created wavelength, the influence of the magnetically induced undulation has to be taken into account.

The influence of the magnetic field strength is characterized by the dimensionless undulator parameter K

$$K = \frac{eB_0\lambda_u}{2\pi m_e c} = 0.934 \cdot B_0[T] \cdot \lambda_u[cm] \tag{2.12}$$

and in first order approximation the emitted wavelength λ amounts to

$$\lambda = \frac{\lambda_u}{2\gamma^2}\left(1 + \frac{K^2}{2} + \frac{\gamma^2}{\theta^2}\right) \tag{2.13}$$

in the laboratory system. As can be seen from the undulator equation 2.13, tuning of the emitted wavelength can be achieved via change of the K value. When passing the undulator, the electron path is slightly prolonged due to the excursions in the magnetic field strength K. This results in a reduced mean axial velocity and consequently in a reduced Doppler shift, i.e. longer wavelengths. Technically this is done by adjustment of the gap between the undulator magnets to change the magnetic field strength B_0. Thus created radiation is linearly polarized in the plane of the electron undulation, which is perpendicular to the magnetic field and to the electron motion.

Radiation from an undulator is used to characterize an XUV Michelson interferometer in chapter 6.1.

2.2.4 High-Gain FELs

A special case of an undulator source is a free-electron laser (FEL). In this case electron bunches are compressed to spatially short bunches and their density is modulated along the bunch. This process appears in long undulators and is called microbunching. If the modulation period matches the emission wavelength, coherent radiation is created. In the following I will give a brief overview of the characteristics of this kind of undulator radiation.

In contrary to XUV radiation emitted by wigglers and bending magnets, XUV-

FEL radiation is characterized by a comparatively high coherence in space and time. The coherence is caused by the interaction of the co-propagation of the optical field with the relativistic electron bunch. The optical field acts back on the electron beam and thereby microbunches are formed in the electron beam. Many electrons radiate coherently which increases the intensity of the FEL drastically compared to undulator radiation. For the intensity I_N of the radiation field of N coherent particles each radiating at I_1 it can be stated that $I_N = N^2 I_1$. For incoherent particles the intensity only amounts to $I = NI_1$. Since emission takes mainly place in areas with high electron density and the size of the microbunches is of the order of the radiation wavelength (before Doppler correction), this process leads to the emission of coherent radiation [40].

XUV-FEL radiation is used to create a free electron plasma from liquid hydrogen in chapter 4.4. In chapter 6.1 an XUV Michelson interferometer is described which is used in chapter 6.2 to determine the coherence properties of XUV-FEL radiation.

2.2.5 High Harmonics of Lasers

Another possibility to create XUV radiation is via the generation of very high harmonics of the fundamental optical laser radiation. For this purpose an intense ultrashort laser pulse is focused preferably into a noble gas and harmonics are created from the non-linear interaction of the electrons in the atomic field and the electric field of the laser [43]. The parameters of the laser are chosen, such that the atoms of the gas are just about to be ionized. In this process a large number of atoms is simultaneously involved and in phase with the laser field. Thus, the created harmonics are in phase and coherent to the laser field and are emitted in a narrow cone in the direction of the laser field. In this non-linear process only odd harmonics are created and the resulting spectrum resembles a frequency comb with a typical cut-off energy in the XUV, that is mostly below 13 nm.

3. Design and Characterization of an XUV Spectrometer

A spectrometer for the XUV spectral range of $\lambda = 4.1\,\mathrm{nm} - 17.1\,\mathrm{nm}$ is presented in this chapter and the technical details of this **X**UV-**M**ulti-**A**ngle scattering **s**pectrometer (**XMAS**) are summarized. First the design parameters are presented including simulations with the ray tracing program ZEMAX (Zemax, LLC, Kirkland, WA, USA). Based on these simulations the components of the spectrometer are designed and constructed and finally assembled. Toroidally curved mirrors focus the source onto an intermediate plane acting as a virtual source for the flat-field grating. Introducing a variable slit into this plane allows for adjustment of the virtual source size and control over aberration in the focal plane. This is a powerful tool to merge seamlessly between spectral resolution and optical throughput. The two configurations of the spectrometer, with and without the collection mirrors are then operated at FEL experiments and their performance is evaluated. Note that the XMAS represents a complementary diagnostics to the multi angle diode array which is presented in chapter 5.

3.1 Motivation

During recent XUV experiments a variety of XUV spectrometers has been used, mostly one at a time [44; 45]. In these experiments intensity and spectroscopic measurements were performed only under one observation angle due to the lack of several XUV spectrometers that can be applied simultaneously during an FEL experiment.

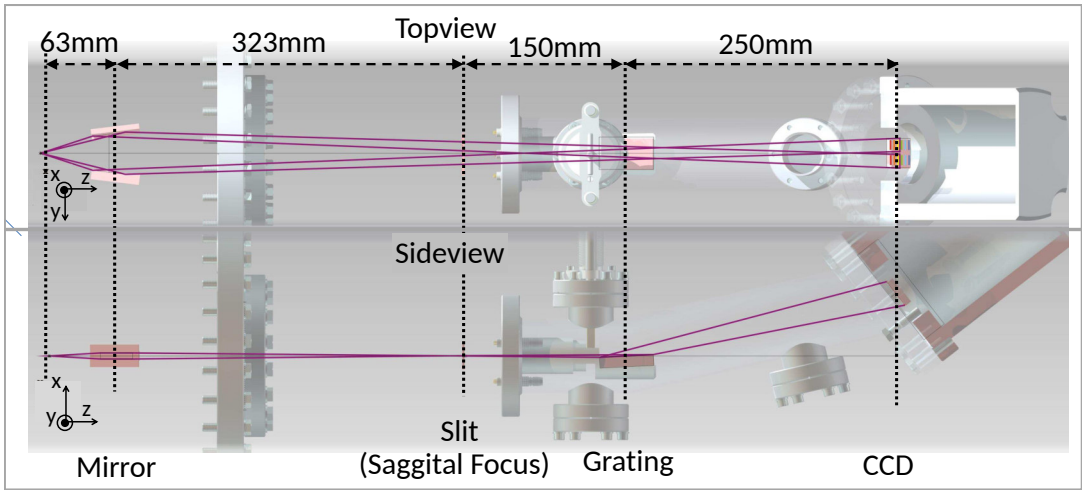

Figure 3.1: Schematics of the spectrometer in combination with construction design that shows vacuum flanges and feedthroughs. The upper part shows a topview of the spectrometer and the lower part displays a sideview.

Often the confined space at an FEL end station limits the amount of bulky vacuum compatible spectrometers. However, simulations show angle-dependent spectra spanning over a broad spectral range. These considerations call for an improved angle-dependent observation with high spectral resolution over a wide spectral range [46]. Such a newly designed spectrometer has to fit in the setup of multiple other diagnostics and safety precautions such as a laser safety tent enclosing the entire experimental setup. The total length of the spectrometer can therefore not exceed 1 m.

3.2 Overall Scheme and Spectrometer Design

An overall scheme of the spectrometer including all optical components is displayed in figure 3.1. Note that the upper part shows a topview and the lower part a sideview of the same spectrometer scheme. Starting from left to the right, the source emits photons in all directions. Two toroidal mirrors collect light which is emitted from the source into different directions. Position and curvature of the mirrors are optimized in such a way, that the 1-dimensional focal line in the sagittal plane serves as a virtual source for the variable line spacing (VLS) grating. An adjustable slit is

introduced in the plane of the sagittal focus to tune between spectral resolution and throughput. The saggital focus acts as a virtual source which is dispersed by a VLS grating and detected by a charge-coupled device (CCD). The source-grating-CCD distances deviate from the parameters provided by the manufacturer due to experimental and technical constraints. To account for the shift of the focus flat field, the CCD is tilted. In the following I will give a detailed overview of the most important spectrometer parts.

3.3 The Variable Line Space Diffraction Grating

In this chapter I will describe the VLS grating. At first emphasis is placed on a simulation of the VLS that reproduces the parameters provided by the manufacturer correctly. As a follow up efficiency measurements that are carried out at a tunable XUV source are presented.

An aberration-corrected concave grating for flat-field spectrographs serves as the dispersive element [47] in many spectrally resolving XUV apparatus. Specific design parameters of the grating such as surface curvature, coating, blaze angle, and line spacing are chosen in such a way that XUV radiation in the respective wavelength range is focused along an almost flat plane. The typically flat XUV sensitive CCD detectors can be set up along the focal plane of the VLS and detect the dispersed radiation. For this experiment a VLS grating from HITACHI is chosen. The surface is spherically curved with a radius of $R = 5649\,\mathrm{mm}$. Light in the spectral range of $\lambda = 7\,\mathrm{nm} - 22\,\mathrm{nm}$ impinging under 3° onto the grating can be spectrally resolved. The $30\,\mathrm{mm}\times 50\,\mathrm{mm}$ surface is coated with a gold layer to achieve a high reflectivity. See fig. 3.2 (left) for a simulation of the reflectivity of a flat gold surface and the bare substrate. Across the length of the grating the line density varies from 1015 to 1449 lines/mm with a central groove spacing of 1200 lines/mm. Each groove has a length of 30 mm and a blaze angle of $3.2^\circ \pm 0.5^\circ$. To obtain a flat-field focus in the focal plane, the local groove spacing σ at the distance w from the center of the

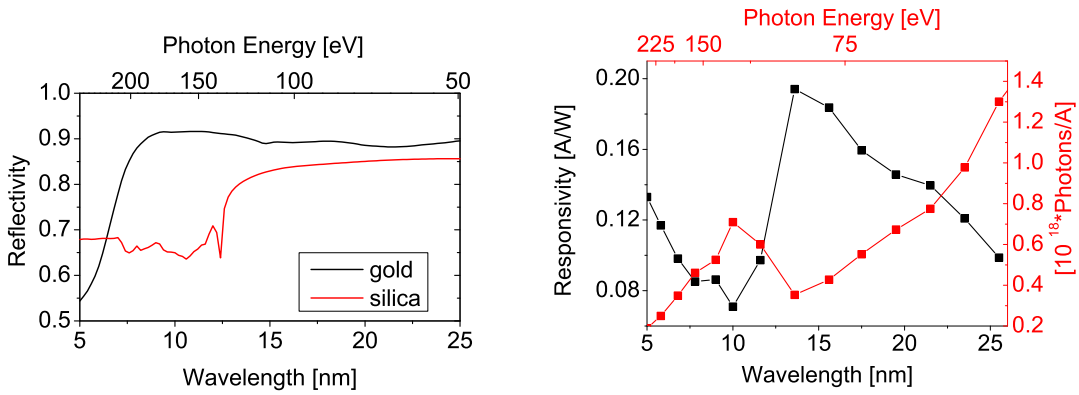

Figure 3.2: *Left:* Calculated reflectivities of a gold surface in the XUV range under low incidence angles of 3° [48]. *Right:* Responsivity of the XUV-Diode

grating follows the equation:

$$\sigma(w) = \frac{\sigma_0}{1 + \frac{2b_2 w}{R} + \frac{3b_3 w^2}{R^2} + \frac{4b_4 w^3}{R^3}} \tag{3.1}$$

where, $\sigma_0 = 1/1200\,\text{mm}$, $b_2 = -20.0$, $b_3 = 4.558 \times 10^2$, $b_4 = -1.184 \times 10^4$.

Precise knowledge of the grating efficiency is crucial for the characterization of the spectrometer. The unknown efficiency of the VLS grating needs to be determined experimentally for different wavelengths. An XUV sensitive photo diode is used to measure the photo current of incoming and diffracted light. In a first step the sensitivity of the diode has been measured in the respective wavelength range. Figure 3.2 (right) displays both responsivity (black) and the corresponding number of photons per current (red). A very unsteady gradient can be stated from this diagram, which is caused by the Si-L absorption edge at 12.3 nm. Thus, a measurement method that rules out the strong wavelength dependence of the diode current is suggested.

The grating efficiency was determined at the synchrotron source DORIS (DESY Hamburg, Germany) at beamline BW3 [49], which is equipped with a monochromator to pick the desired photon energy. Energies of 70 eV (17.71 nm), 100 eV (12.40 nm), 130 eV (9.54 nm), 160 eV (7.75 nm), and 190 eV (6.53 nm) were picked

to determine the grating efficiency in the specified range. Due to the constant decrease of the ring current in the synchrotron the initial condition, i.e. the incoming XUV radiation on the grating changes continuously. Thus, during the experiment both ring current and diode current are logged simultaneously. The grating itself is placed on a high precision goniometer that enables rotation of the grating in steps of $(1/4000)^\circ$. Since the synchrotron beam direction is fixed, this goniometer allows for different incidence angles onto the grating. Incidence angles of 2°, 3°, 4° are chosen for the experiment, where 3° is recommended by the manufacturer. In addition the grating is placed on a motorized stage which moves perpendicular to the photon beam, so that the grating can be moved out of the beam to measure the direct beam current I_0. To measure the XUV intensity in different diffraction orders, the XUV diode is also placed on a goniometer that allows for the diode to be rotated around the grating in steps with $(1/4000)^\circ$ precision. For this experiment intensities in an angular range from 4° to 40° in steps of 1.75° were measured. To prevent saturation of the diode in the direct beam an 800 nm Ti-foil was placed in front of the diode during the entire experiment. For each photon energy and incidence angle the grating efficiency was determined as follows. At first the grating was moved out of the beam so that the diode measures the direct photon current I_0, corresponding to the ring current I_{0ring} of the synchrotron. Then the grating was moved into the beam and rotated such that the respective incidence angle was set. The diode was then rotated around the grating and the photon current I_θ was measured, as well as the corresponding ring current I_{ring}. The efficiency was calculated as:

$$\text{Efficiency} = \left(\frac{I_\theta - I_{dark}}{I_{ring}}\right) / \left(\frac{I_0 - I_{dark}}{I_{0ring}}\right) \tag{3.2}$$

Note that measurements of the diode are corrected by the dark current I_{dark}, which is measured with blocked synchrotron radiation.

Figure 3.3 displays the grating efficiency for different incidence angles of the radiation. For each photon energy there are two peaks in the curve. In this case the peak for lower angles represents the zeroth diffraction order and thus simply the reflection of the grating. A comparison of this first peak to the simulated reflection

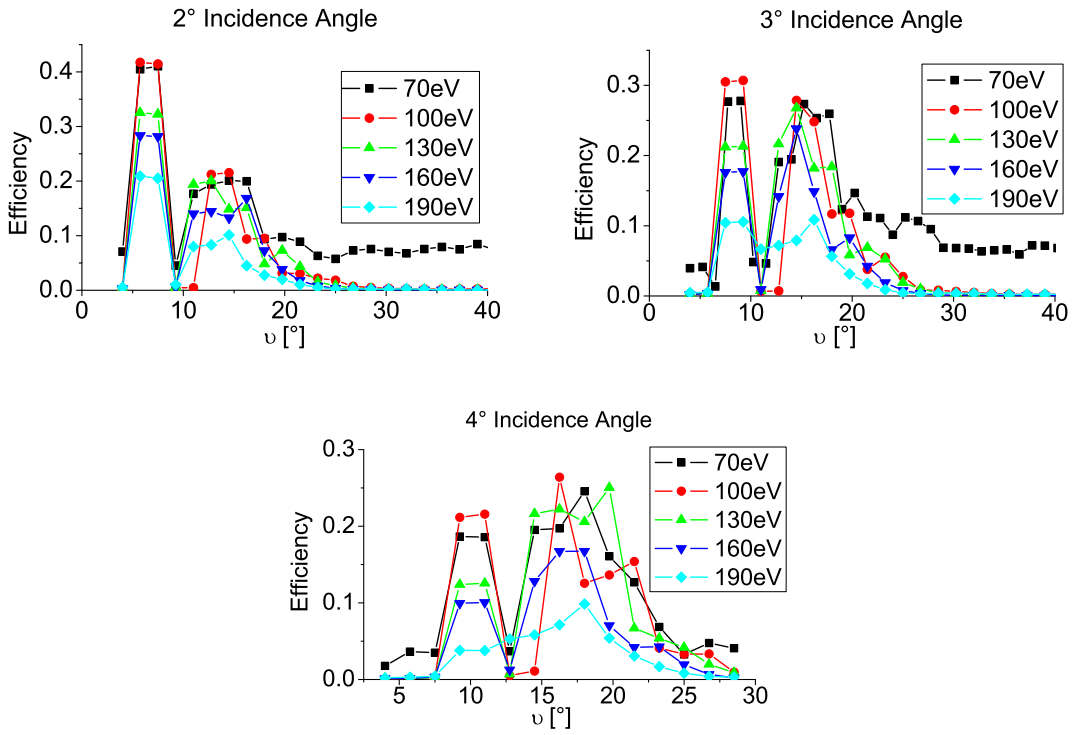

Figure 3.3: Efficiency of the grating for different incidence angles 2°, 3°, 4°. ν denotes the observation angle with respect to the direction of the incoming light from the synchrotron source.

in fig. 3.2 shows a lower value than expected for the zeroth order reflection, which can be attributed to the blazing of the grating surface, which is intended to maximize diffraction into the first order. The second peak in the efficiency curve represents the first order diffraction.

Figure 3.4 displays the wavelength dependent peak efficiencies of the first order diffraction for each incidence angle. For the manufacturer-recommended incidence angle of 3° the highest efficiency of up to 28 % is measured in the lower photon energy range whereas for a very shallow incidence the efficiency drops down to about 22 %. For higher energetic photons the incidence angle is not affecting the efficiency which is constantly about 11 %. This shows, that the blaze angle is optimized for incidence under 3°, which is also stated by the manufacturer.

In reference [50] a different method was used to determine the absolute efficiency

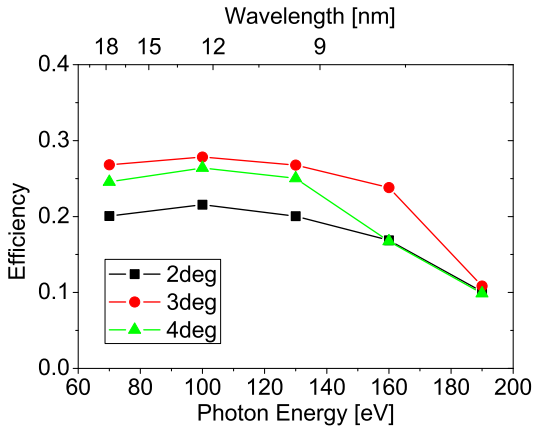

Figure 3.4: Measured grating efficiency for different incidence angles.

of a similar grating. An efficiency of 8.5 % for 6.8 nm and 12 % for 17 nm in first order was published in 1984, which is lower than the newly measured values. The remaining discrepancy can be attributed to an improved manufacturing process over the last 20 years (as stated in a personal note by the manufacturer). A more accurate control of the ruling process results in a lower noise level of the line spacing and hence in an improved efficiency. This again underlines the importance of this re-measurement of these values, to update previously published values.

3.4 Collection Mirror Setup

A detailed section of the source mirror setup is shown in fig. 3.5. The source (orange) emits XUV light which is collected by the toroidally curved mirrors. The incident angle of the XUV radiation onto the mirrors varies between 7.06 ° and 11.27 ° and thus can be treated in the grazing incidence regime resulting in a moderate reflection of about $60 - 80$ % (see fig. 3.6 (right)). In this setup the radiation emitted from the source can be observed simultaneously under angles of 14.16 ° to 18.37 ° and −14.16 ° to −18.37 °. Together with the lateral height of 5.6 mm of the mirrors this amounts to a total collection solid angle of $6.56 \times 10^{-3}\, sr$ per mirror or $1.31 \times 10^{-2}\, sr$ in total. To determine the optimum curvature of the toroidal mirror the ray tracing

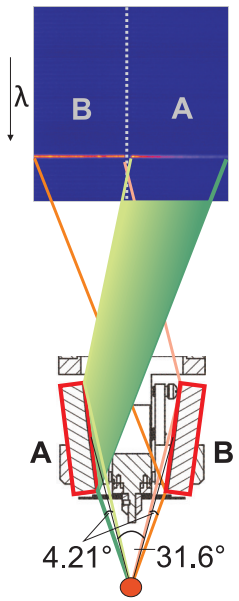

Figure 3.5: Simplified scheme of the mirror setup. Light is emitted from the source (orange) onto the mirrors A and B. Each mirror reflects onto a separate half of the detector, which is shown in the blue inset. Spectra of Si-L-radiation collected by different mirrors are separated along the grey dashed line. For clarification of this issue, all other optical elements are left out in this scheme.

software ZEMAX is used. Fitting parameters are set in such a way that the vertical focus in the meridional plane is as narrow as possible at the slit and that the width of the beam in meridional plane covers half of the CCD. This way, a single detector can cover the signal from both mirrors. In the simulation, the optimum curvature of the mirrors is $R_M = -16.5\,\text{mm}$ in the meridional plane and $R_S = -950\,\text{mm}$ in the saggital plane. The mirrors cover a length of 5.6 mm in the saggital plane and 30 mm in the meridional direction. The blue inset in fig. 3.5 shows the spectrum of Si-L-shell radiation as a line on the chip, detected by both mirrors and illustrates the separation on the detector along the grey dashed line.

To image the source onto the slit in the meridional plane and to converge the beam onto the camera in the saggital plane the mirrors need to be shaped toroidally which at the same time introduces a strong astigmatism. For this purpose multi-layer reflection mirrors are not suitable, because of the required wide spectral range of several *nm*. Instead, the reflectivity for different single layer coatings commonly

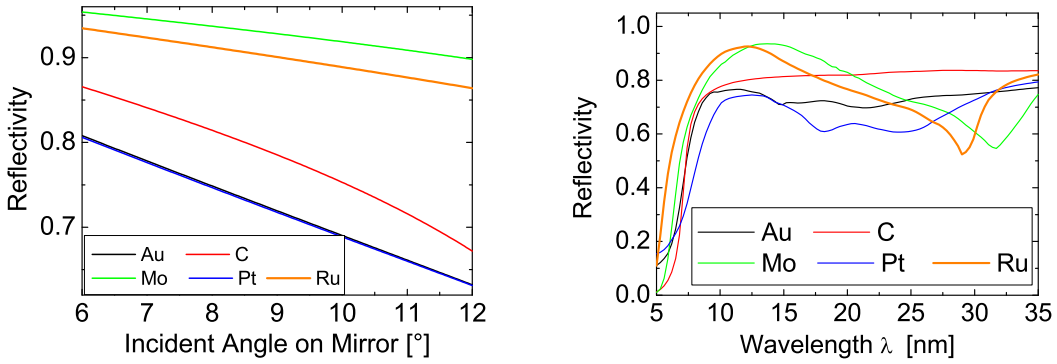

Figure 3.6: *Left:* Calculated angle dependent reflectivity for different coatings at $\lambda = 13.5\,\text{nm}$. *Right:* Calculated wavelength dependent reflectivity for different coatings at $8.2\,^\circ$, RMS roughness 1 nm

used in high precision optics is calculated from the *Henke* tables [48]. In the left part of fig. 3.6 the reflectivity depending on the incidence angle is calculated for different materials. In the range of $6\,^\circ$ to $12\,^\circ$ these reflectivities reach from 95 % to 60 % with a higher reflectivity for ruthenium and molybdenium as compared to gold, silver, platinum, and carbon. In general the reflectivity decreases for larger incidence angles by about 5 % to 20 %. In the right part of fig. 3.6 the wavelength dependent reflectivity for a fixed incidence angle is calculated for different coatings. All materials exhibit a reflectivity of less than 20 % for wavelengths as short as 5 nm with a steep increase of reflectivity towards wavelengths of 7 nm and longer. For these wavelengths the reflectivity ranges from 60 % to 95 %. In this work ruthenium is chosen as coating material due to its overall high reflectivity and its good processability for the mirror coating procedure.

Such curved and coated mirrors were supplied by the Institute for Applied Physics - University Jena/Germany.

3.5 Design Parameters and Technical Implementation

The VLS in Matlab

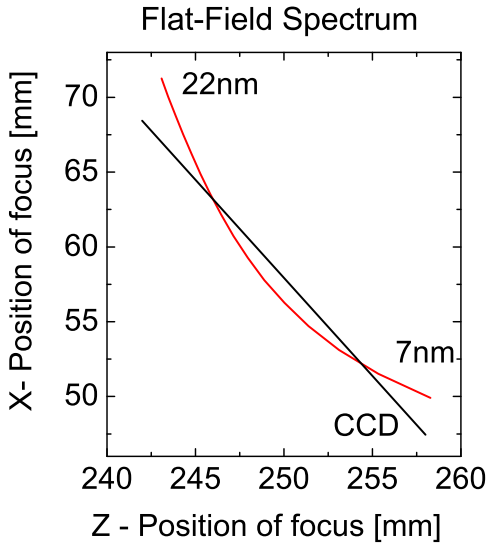

Figure 3.7: Simulated focal plane (red) with a source to grating distance of 150 mm. The black line marks the optimum position of the CCD. In this configuration the detector is tilted by 37 °.

Given the design parameters, the grating performance is simulated with MATLAB (The MathWorks, Inc.; Natick, MA, USA) to discover the optimal detector position and tilt for a sufficiently short source-grating-CCD setup. Due to safety restrictions, that require a laser shielding tent, the experimental setup at FLASH has a limited amount of space. The XUV spectrometer in question will be mounted to an already existing experimental setup, whose geometry and size is mainly defined by the FEL beam path and several measurement instruments. In combination, these restrictions require the design of a spectrometer which is short in length. While the optimal source to grating distance is given by $r_{des} = 237\,\text{mm}$ resulting in a grating to CCD distance of $r'_{des} = 235.3\,\text{mm}$, here a source to grating distance of $r = 150\,\text{mm}$ is chosen. Such a shortened r leads to a slightly longer grating-CCD distance of

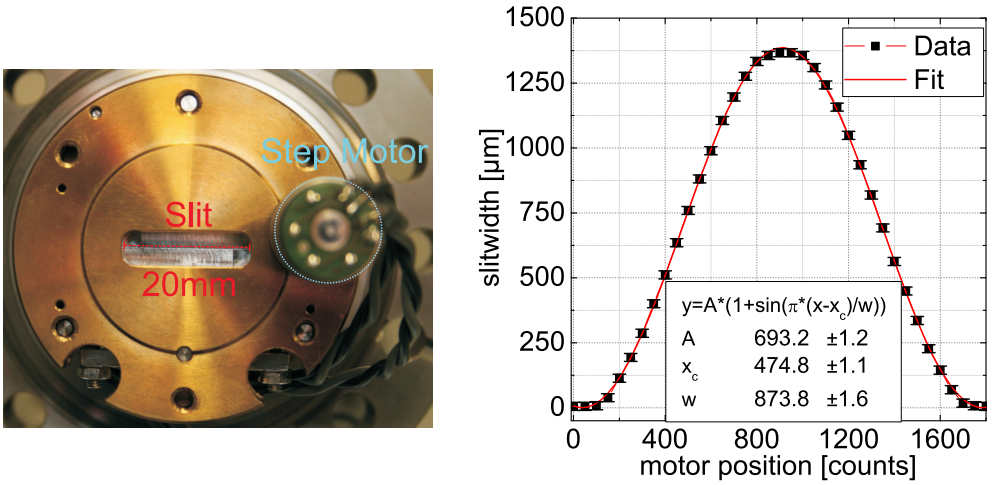

Figure 3.8: *Left:* Photograph of the adjustable slit unit. The width of the slit is 20 mm and the height of the slit is adjustable between 0 and 1000 μm with an accuracy of 15 μm. The slit is closed in this image. A blue circle marks the step motor to adjust the slit size. *Right:* Relation between step motor counts and slit opening. A sin-function is fitted to the data, which results from the fact that the slit is driven by an excenter wheel

$r = 250$ mm and a tilt of the image plane by 37°. Figure 3.7 displays the simulated position of the focused XUV-wavelengths. The black line marks the position of the CCD tilt by 37°. Such a shortened source-grating-CCD setup saves about 70 mm in length or 15% of the original total length. Defocusing or possible decrease in spectral resolution can be prevented by tilting the detector.

Important Optical Features

Figure 3.8 shows the adjustable slit, which is introduced in the plane of the virtual source. Its size can be adjusted between 0 μm and 1000 μm with an accuracy of 15 μm. The diagram on the right side of fig. 3.8 shows the correlation between stepper motor counts and slit opening, which has been measured with a microscope. The reason for the sin-like function lies in the excenter drive of the opening mechanism. Since the toroidal surface of the mirror exhibits a strong astigmatism, the slit has to be introduced. By adjusting the source size, seen by the grating, the balance between optical throughput and spectral resolution can be chosen. Behind the slit, optical filters and a customized vacuum shutter are introduced.

CCD

A cooled Andor iKon CCD with 2048×2048 pixels of 13.5×13.5 μm^2 size and a sensor size of 27.6×27.6 mm^2 serves as a detector. To attach the CCD to XUV in-vacuum experiments a CF100 flange is fixed to its front. Cooling of the back-illuminated chip down to $-90\,°C$ is possible via 4-stage peltier elements. Choosing suitable cooling temperature to minimize thermal noise is an important issue in experiments with low signal rate. Depending on the vacuum conditions and the presence of residual gases, the cooling temperature should be limited in order to to prevent freezing onto the chip. To merge between fast readout and low readout noise the pixel readout rate can be adjusted between 5 MHz and 50 kHz. Binning and region-of-interest readout mode can be applied to further increase the sampling frequency of the detector. Since the chip is also sensitive to lower photon energies it has to be protected from visible light, e.g. by thin film metal filters.

3.6 Focal Point and Virtual Source

To determine the influence of the collection mirror aberration on the spectral resolution, the source-mirror-slit configuration has been simulated using the ray tracing software ZEMAX. In this configuration the mirror curvature radius in saggital plane is optimized for smallest focus at the slit position. Figure 3.9 shows the simulated focal spots for 13.5 nm behind the slit for different slit sizes. Note that the slit is extended in meridional direction, so that the entire beam can pass the slit. Since the slit acts as a virtual source for the VLS grating, the source extension in saggital direction hampers the possible spectral resolution. As can be seen from fig. 3.9, an increase of spectral resolution is traded in for a decreased optical throughput.

The left part of fig. 3.10 shows an image of the filter holder, which is attached to a vacuum feedthrough. The thumb wheel allows for four different beam pass options. In closed position the lever on top of the thumb wheel allows for vacuum-tight sealing of the rear part of the spectrometer. The rear part of the spectrometer contains the VLS-grating and the CCD. Hence, the spectrometer can be attached to a vacuum chamber which may be vented for various reasons, e.g. target replacement, change of setup, while sensitive devices can be kept under vacuum conditions. In

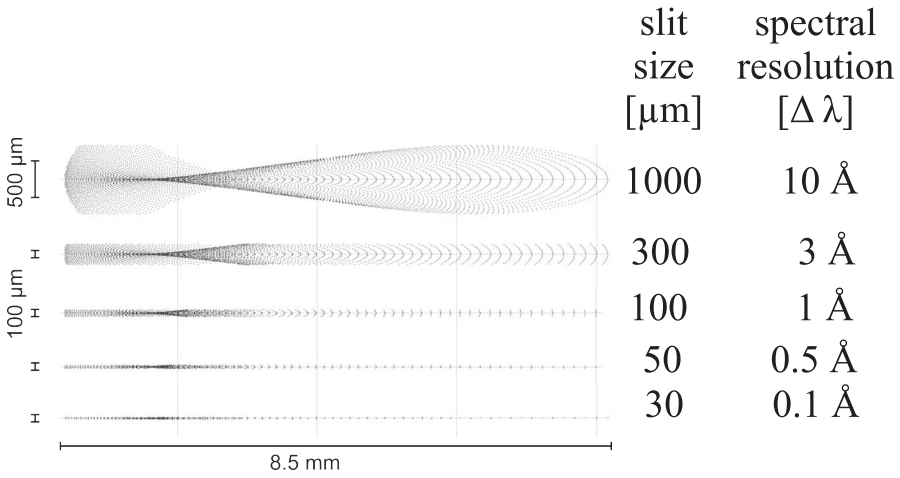

Figure 3.9: Simulated spot sizes behind the slit. Depending on the slit size different spectral resolution for an ideal grating can be estimated using the ray tracing software ZEMAX. At the slit, the focus has a width of 8.5 mm

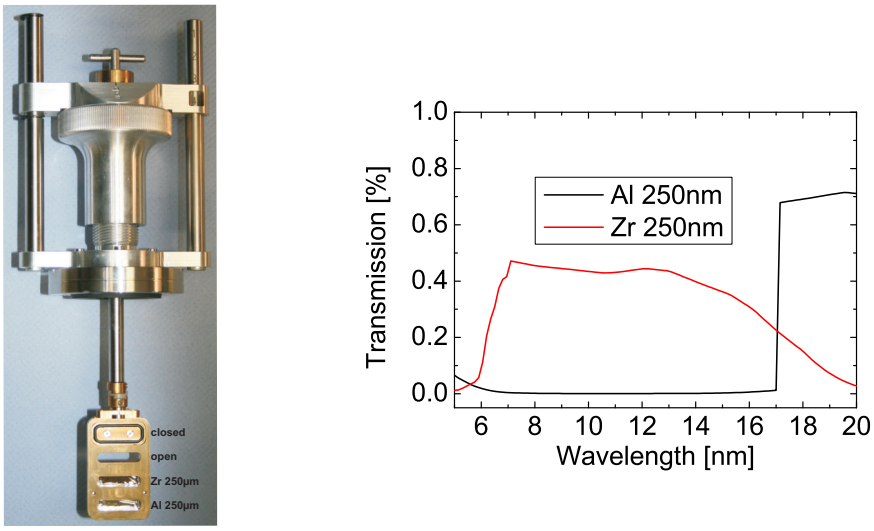

Figure 3.10: *Left:* Photograph of the vacuum feedthrough. The thumb wheel on top allows for four different interceptions of the beam path. 1. beam is blocked, 2. unhindered 3. 250 nm Zr-foil, 4. 250 nm Al-foil. *Right:* Transmittance of a 250 nm Zr-foil and a 250 nm Al-foil. Both foils may shield the detector from visible light and are transparent in complementary XUV spectra. [48]

the second position the filter holder is open and the beam passes without blocking or attenuation. In the third position a Zr-foil of 250 nm thickness allows for blockage of visible light, while XUV wavelengths are transmitted. An Al-foil of 250 nm thickness can be inserted in the beam path via the fourth filter position. This Al-foil shields visible light from the CCD and transmits XUV wavelengths. The right part of fig. 3.10 displays the simulated transmittance of the foils in the relevant XUV wavelength range. While the Zr-foil transmits XUV photons almost over the entire wavelength range of the spectrometer, there is no transmission of the Al filter for photon energies below 72.7 eV. Therefore, the Al-filter can be used to benchmark the spectral resolution of the spectrometer by evaluation of the Al absorption edge width. The position of the absorption edge is known to be at 17.2 nm.

3.7 Measurement and Calibration

Calibration Source

To determine the dispersion of the spectrometer a source with well known spectral properties over a broad wavelength range is needed. In this work the emission spectrum of an aluminum plasma with its numerous lines in the XUV wavelength range is chosen. Wavelengths of the respective electron transitions are well known [48].

To generate a sufficiently hot plasma, a Titanium:Sapphire (Ti:Sa) laser at a wavelength of 800 nm with a pulse energy of 2.5 mJ and a pulse duration of 60 fs is used. A gold coated off-axis parabola focuses the beam down to a spot size of 5 μm (FWHM) onto a high purity Al foil (99.5 %) with a thickness of 6.5 μm. To store the acquired spectra after each laser pulse, the laser is operated in single shot mode. Target replacement is ensured via a three-axis positioning stage moving the target both into the focus of the laser beam and orthogonal to the laser direction to ensure that the laser hits an undamaged area of the foil at each shot. When the laser pulse hits the Al-foil, a plasma is created at the surface of the foil. Depending on existing ionization states, free electron temperature T_e and free electron density n_e in the plasma, a spectrum with typical emission lines of electron transitions in the Al electron shell can be observed. Due to the strong absorption of the XUV light in the 6.5 μm thick Al foil, only light in direct line of sight from the plasma can be observed.

Dispersion

A typical single shot Al emission spectrum is depicted in fig. 3.11. Qualitatively, the spectra from both mirrors A and B look alike. The spectrum shows a number of distinct sharp emission lines in the observed spectral range that rise above a bremsstrahlung pedestal. Lines that are marked with a black triangle in fig. 3.11, were identified as Al emission lines and their tabulated transition energies [51] are shown in table 3.1.

After identifying the most prominent emission lines in the measured spectrum,

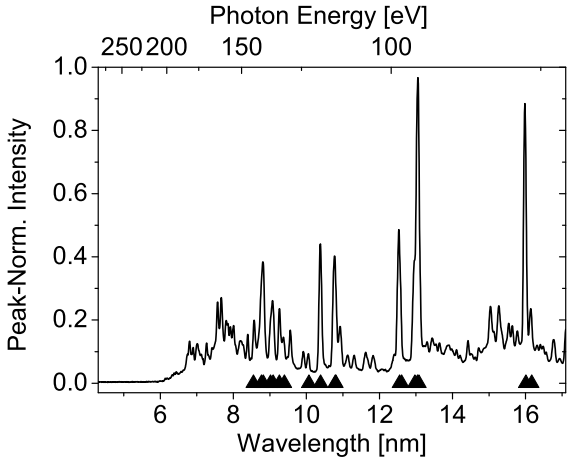

Figure 3.11: XUV intensity as a function of wavelength, emitted by the single shot laser-irradiated Al-foil. The black triangles represent the lines used for fitting the dispersion functions. Wavelengths of Al-spectral lines are also listed in table 3.1.

Table 3.1: The strongest observed XUV lines, as identified from the NIST atomic spectra database (ASD) [51], for Al ions.

Observed Wavelength [nm]	NIST ASD Wavelength [51] [nm]	Ion	Transition Configurations
10.50 ± 0.06	10.07	Mg VI	$2s^2 2p^3$ - $2s^2 2p^2(^3P)3d$
16.165 ± 0.06	16.17	Al IV	$2s^2 2p^6$ - $2s^2 2p^5(^2P^\circ)3s$
16.00 ± 0.06	16.01	Al IV	$2s^2 2p^6$ - $2s^2 2p^5(^2P^\circ)3s$
13.03 ± 0.05	13.04	Al V	$2s^2 2p^5$ - $2s^2 2p^4(^3P)3s$
13.07 ± 0.06	13.08	Al V	$2s^2 2p^5$ - $2s^2 2p^4(^3P)3s$
12.96 ± 0.05	12.97	Al IV	$2s^2 2p^6$ -$2s^2 2p^5(^2P^\circ)3d$
12.60 ± 0.05	12.61	Al V	$2s^2 2p^5$ - $2s^2 2p^4(^1D)3s$
12.54 ± 0.05	12.55	Al V	$2s^2 2p^5$ - $2s^2 2p^4(^1D)3s$
10.83 ± 0.05	10.81	Al V	$2s^2 2p^5$ - $2s^2 2p^4(^3P)3d$
10.79 ± 0.05	10.79	Al V	$2s^2 2p^5$ - $2s^2 2p^4(^3P)3d$
10.39 ± 0.05	10.39	Al V	$2s^2 2p^5$ - $2s^2 2p^4(^1D)3d$
9.38 ± 0.05	9.3955	Al V	$2s^2 2p^5$ - $2s^2 2p^4(^3P)4d$
9.27 ± 0.05	9.26	Al VI	$2s^2 2p^4$ - $2s^2 2p^3(^4S)3d$
9.09 ± 0.05	9.09	Al VI	$2s^2 2p^4$ - $2s^2 2p^3(^2D)3d$
8.82 ± 0.05	8.82	Al VI	$2s^2 2p^4$ - $2s^2 2p^3(^2D)3d$
8.76 ± 0.05	8.77	Al VI	$2s^2 2p^4$ - $2s^2 2p^3(^2D)3d$
8.56 ± 0.05	8.55	Al VI	$2s^2 2p^4$ - $2s^2 2p^3(^2P)3d$

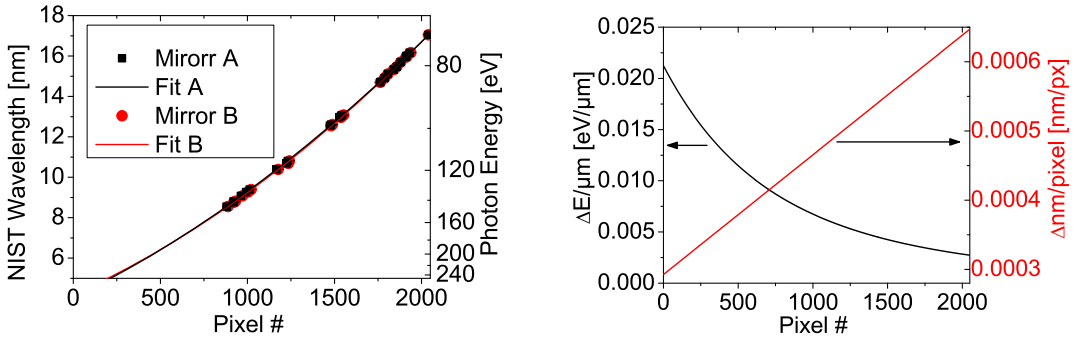

Figure 3.12: *Left:* Dispersion function of the spectrometer for both mirrors. The abscissa shows the absolute CCD pixel position. The ordinate displays the nm (left) and eV (right) of the identified transition lines. Tabulated values are taken from the atomic spectra database of NIST [51]. Fitting parameters for the curves are: A:λ[nm] = $(4.05 \pm 0.14) + (4.17 \pm 0.20)10^{-3}x + (1.078 \pm 0.071)10^{-6}x^2$ and B: λ[nm] = $(4.19 \pm 0.10) + (3.85 \pm 0.15)10^{-3}x + (1.204 \pm 0.052)10^{-6}x^2$ *Right:* From the Dispersion and the pixel size (13.5 μm) the energy spread per pixel is calculated.

their position on the CCD is plotted against the tabulated wavelengths. In the left part of fig. 3.12 a second order polynomial is fitted to either data set. The second order dispersion functions are thus:

$$\lambda_A[\text{nm}] = (4.05 \pm 0.14) + (4.17 \pm 0.20) \times 10^{-3}\text{x} + (1.078 \pm 0.071) \times 10^{-6}\text{x}^2$$
$$\lambda_B[\text{nm}] = (4.19 \pm 0.10) + (3.85 \pm 0.15) \times 10^{-3}\text{x} + (1.204 \pm 0.052) \times 10^{-6}\text{x}^2$$

where x is the pixel position on the CCD. According to the dispersion function, the CCD spans over a wavelength range for each mirror as follows:

pixel	A [nm]	A [eV]	B [nm]	B [eV]
0	4.05	306	4.19	296
2048	17.19	72.5	17.12	72.4

Note that especially shorter wavelengths will be difficult to observe in this setup! This is due to the fact that the transmission of the visible light blocking Zr foil decreases significantly for wavelengths shorter than 7 nm.

Comparing the design values and the dispersion from the ray tracing simulation

to the dispersion function from the experiment, there is a disagreement. While the shape of the dispersion curve can be well approximated to a second order polynomial, there is an offset which results in a shifted total wavelength range towards shorter wavelengths. This deviation is likely caused by the fabrication process of the spectrometer parts and during the assembly. Uncertainties can be introduced in different ways, such as soldering of vacuum flanges and tubes and the mechanical mounting of filters and grating. Especially the relative position of the virtual source, i.e. the slit, and the grating has a major influence on the dispersion.

The right part of fig. 3.12 shows the energy spread per μm (left) in black and the wavelength change in nm per pixel (right) in red depending on the position on the CCD. Since this plot represents basically the first derivation of the dispersion function, it shows that longer wavelengths will be separated further on the detector than short wavelengths.

Resolution

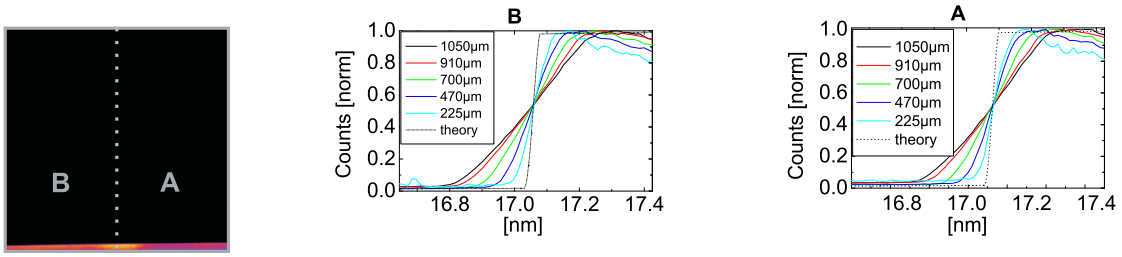

Figure 3.13: Spectral resolution at the Al absorption edge of 17.055 nm *Left:* Si-bremsstrahlung with a 250 nm Al foil in front of the CCD. Grey rectangles mark the areas of either of the mirrors. *Middle, Right:* Normalized profile of Al L-absorption edge for the mirrors B-(middle) and A-(right). The slit width is varied between 225 μm and 1050 μm

To determine the spectral resolution of the spectrometer depending on the different slit sizes a source with a narrow spectral emission line is needed. Alternatively the Al L-absorption edge at 17.055 nm (72.7 eV) of the 250 nm Al filter can be used. Si-bremsstrahlung from a laboratory XUV tube described in chapter 2.2.1 serves as the source of broadband XUV radiation while the Al-filter is introduced in the beam

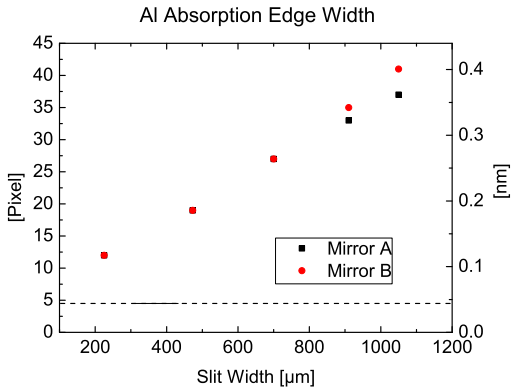

Figure 3.14: Width of the Al L-absorption edge at 17.055 nm for different slit widths. The dashed line below 5 px marks the natural line width of ≈ 0.05 nm (0.2 eV) the Al-absorption edge.

path. Due to the absorption in the L-shell of Al a step like decrease of intensity can be observed in the spectrum as can be seen in the left part of fig. 3.13. The edge width of the absorption edge is now analyzed for both mirrors and different slit sizes between 225 μm and 1050 μm. To account for the decreased throughput at smaller slit sizes the number of accumulations for each spectrum is adapted to achieve a comparable count rate for the respective setting. Figure 3.13 (middle, right) shows the steepening of the edge and thus the increase of spectral resolution for a decreased slit size.

Figure 3.14 displays the width of the L-absorption edge for different slit widths for both mirrors. At the expense of a relatively low throughput the spectral resolution can be raised to 0.12 nm at 17.055 nm which leads to a spectral resolution of $E/\Delta E = 144$.

To analyze the spectral resolution at other XUV wavelengths the emission of a laser generated Al plasma was observed with a 250 nm Zr foil as a visible light block in front of the detector. Different slit sizes between 510 μm and 1330μm where adjusted. Spectrally resolved images of different Al plasma emission lines were evaluated. Figure 3.15 shows profiles of the doublet at 16.0 nm (77.4 eV) and of 4 separate emission lines at 13.1 nm (94.6 eV) for different slit sizes. While the

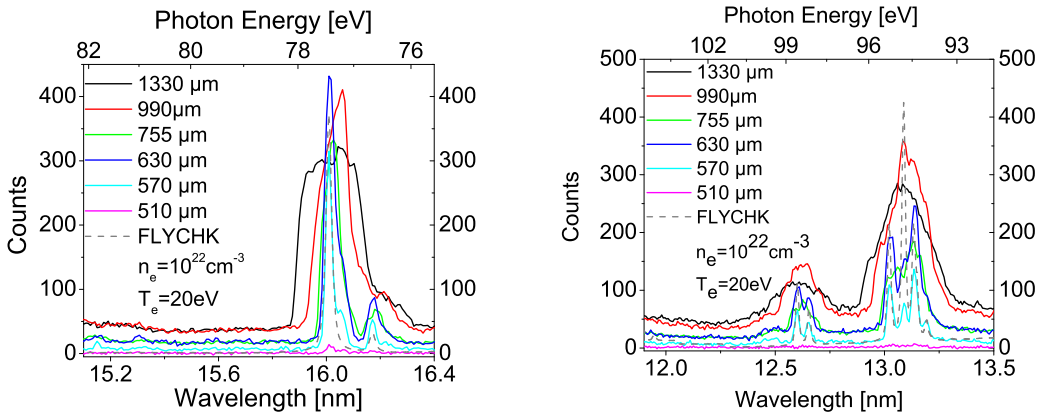

Figure 3.15: Spectral resolution of different Al plasma emission lines for different slit sizes. The dashed grey line marks the FLYCHK [52] simulation for a free electron density $n_e = 10^{23}\,cm^{-3}$ and a free electron temperature of $T_e = 10\,\mathrm{eV}$.

lines are not resolved for a wide opened slit, they can be discriminated for slit widths of 630 μm and smaller. No spectral lines can be detected for slit sizes smaller than 510 μm, since the transmission through the slit is too low.

Throughput

Figure 3.16 shows the wavelength dependent photon transmission of the different spectrometer components. Note that the term "transmission" can also be understood as reflectivity in this context. The black line marks the reflectivity of a ruthenium coated mirror for an incidence angle of 8.2 ° and zero surface roughness (see also fig. 3.6). A red line marks the measured grating efficiency from fig. 3.4. The transmission of the visible light shielding Zr foil from fig. 3.10 is marked in green here. Manufacturer information about the quantum efficiency of the CCD is reproduced in the dark blue line, while the light blue line shows the transmission of a 50 nm Si dead layer on the CCD. It can be understood by means of photo absorption of silicon inside the CCD chip. The distinct edge at 12.3 nm marks the absorption edge of the Si L-shell.

All transmission and reflectivity effects are included in the dashed line. For wavelengths shorter than 7 nm the total efficiency drops by one order of magnitude

which is mainly caused by the decreased grating efficiency and transmission of the Zr foil. Removing the Zr foil would require careful shielding of the experimental setup from scattered visible light and is not always possible, since visible light can also originate from the XUV source point, e.g. at laser plasma experiments. In the central wavelength range the trend of the total efficiency is mainly determined by the transmission of the Si dead layer with an effective thickness of 50 nm on the CCD. In the long-wavelength limit there is no limitation from optical components. The limited size of the CCD is the reason why the spectrometer range does not extend further into that wavelength range.

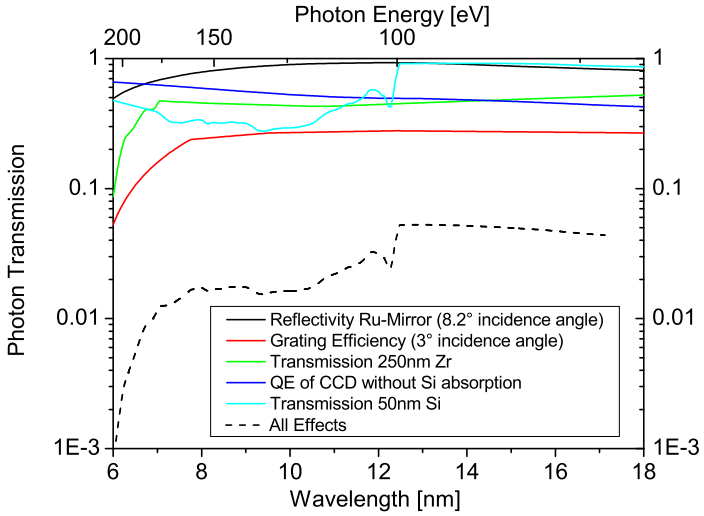

Figure 3.16: Displayed are the different efficiencies and transmissions of optical elements in the beam path. Not included is the slit and its influence on the edge of the focus.

4. XUV Spectrometry of Plasmas

4.1 Multi Angle Spectroscopy of a Laser Generated Al Plasma

A proof of principle experiment that uses the two collecting mirrors of the XMAS simultaneously is presented in this chapter.

For the multi angle spectroscopy experiment the same setup as for the determination of the dispersion, which is described in chapter 3.7 was used. An ultra short ($\approx 50\,\mathrm{fs}$) Ti:Sa laser pulse with a pulse length of 60 fs, a pulse energy of 2.5 mJ, and a wavelength of 800 nm is focused onto an Al foil of 6.5 μm thickness. At moderate laser intensities an Al plasma is created at the foil surface. Depending on existing ionization states, free electron temperature T_e and free electron density n_e in the plasma, a spectrum with typical emission lines of electron transitions in the Al electron shell can be observed. Only the mirror facing the front side of the foil observes plasma emission, if the laser pulse impinges well below the edge of the foil. Since the plasma extends over a certain area across the foil surface, a spectrum can also be observed by the mirror facing the rear side of the foil under certain circumstances. As shown in the left part of fig. 4.1, emission from the edge of the plasma will reach over the edge of the foil, and thus can be detected by the rear side mirror, if the laser is focused in the vicinity of the Al foil edge. To observe also emission from the central parts of the plasma, the laser focus needs to be pointed further to the edge of the Al foil as can be seen in the middle and right parts of fig. 4.1. Since the wavelength range of the spectrometer extends over emission lines of several ioniza-

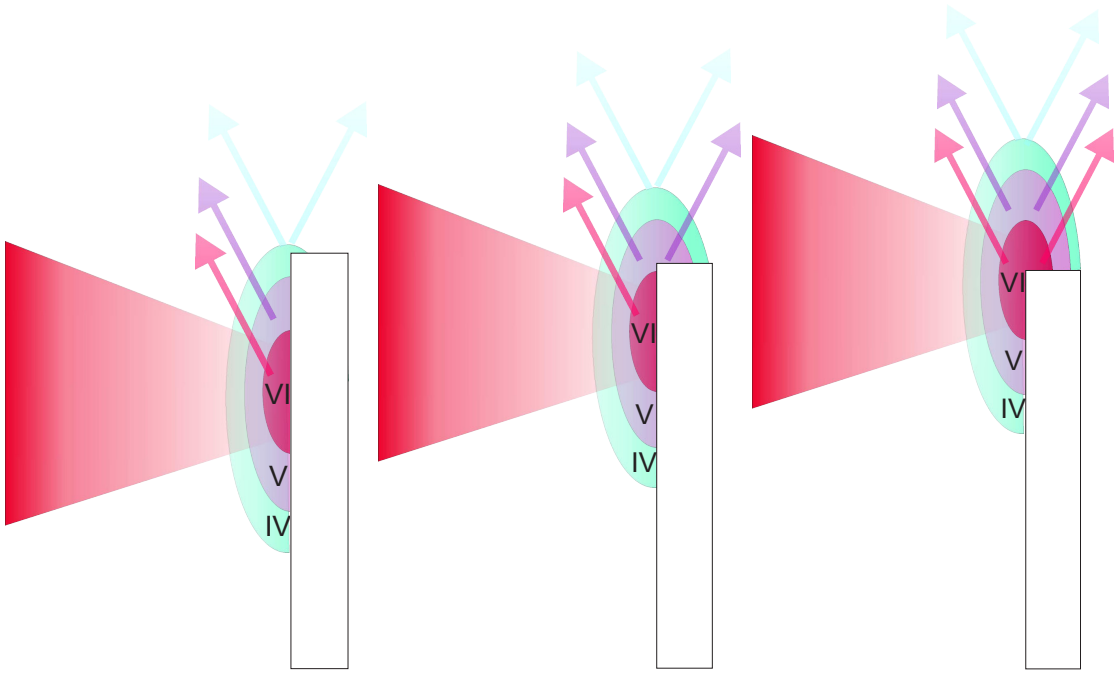

Figure 4.1: Plasma emission scheme of the experiment. The laser coming from the left side creates an extended plasma at the surface of the 6.5 μm foil. *Left:* Due to the absorption of the Al foil plasma emission will mainly be observed by the front side mirror. *Middle:* If the laser focus hits the foil close to edge, the plasma will extend over the edge of the foil and emission will be observed by the rear side mirror. *Right:* Both mirrors will observe the same spectra, if the laser pulse hits the foil directly at the edge of the foil. No shadowing by the foil itself is observed in this case.

tion states of Al, the plasma in fig. 4.1 is split into three different ionization zones, IV, V, and VI. The temperature and density profile is expected to be smooth and with T_e and n_e decreasing from the center to the edge. The inner zones contain mixtures of all kinds of ionization states, and thus will emit photons of different Al transitions. The rear side mirror will observe plasma that heats up, as the laser focus moves closer to the edge, in contrast to the front side mirror which observes the entire plasma for each shot and thus an integrated signal over all temperatures. Since a profile of the respective detector images is used to determine the spectral emission, there is no spatial resolution of the plasma temperature within a single mirror image.

Figure 4.2 (top left) shows typical spectra of front and rear side mirror for the

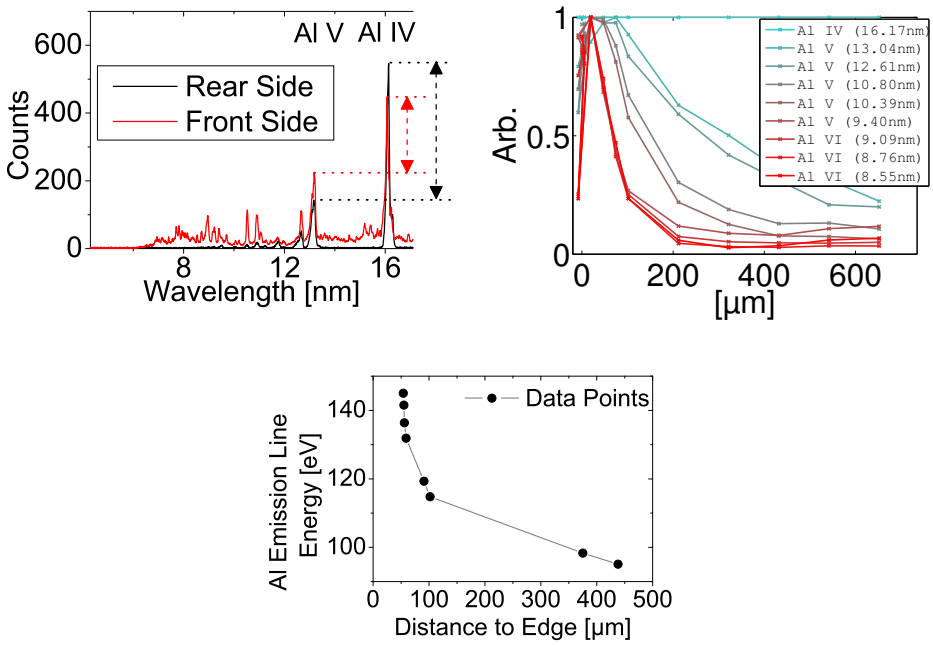

Figure 4.2: *Top Left:* Typical spectra from front and rear side mirrors for the same shot. The emission lines at 16.17 nm and 13.04 nm and their respective intensity relation are marked. *Top Right:* Normalized intensity relation of the different emission lines and the Al IV emission line at 16.17 nm for the rear side mirror. Normalization is carried out with respect to the corresponding front side relation. X-axis shows the distance of the laser focal spot to the edge of the foil. *Bottom:* Observation of most energetic Al emission lines at distances to the foil edge.

same shot. While the front side mirror shows a spectrum with many Al emission lines also from higher ionization states, the rear side mirror observes only a few emission lines for lower ionization states, indicating a plasma with lower T_e. To make this observation accessible to a detailed analysis, the intensity ratio of the emission line at 16.1 nm and other emission lines are calculated. This ratio is normalized by the respective ratio of the same emission lines from the front side mirror to compare the data to other laser shots on the Al foil. Normalizing the data rules out shot to shot fluctuations caused by different laser pulse intensities or differing focal conditions of the laser. This data processing is now done for different emission lines over the full wavelength range of the spectrometer and for different distances between the laser focus and the edge of the foil, as shown in fig. 4.2 (top right).

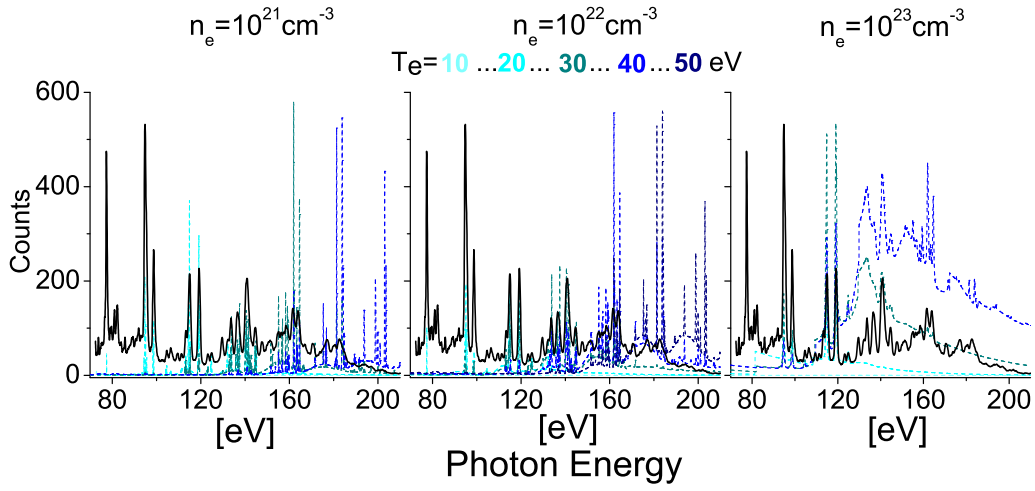

Figure 4.3: To estimate the free electron density n_e the measured spectrum (black solid line) is compared to simulated emission spectra of different free electron temperatures (blue dashed lines). Especially for higher photon energies the simulation for $n_e = 10^{21}\,cm^{-3}$ (left) does not reproduce the characteristic bumps. For $n_e = 10^{23}\,cm^{-3}$ (right) the simulated spectra superelevate these bumps to a plateau that contains a less structured shape. For $n_e = 10^{22}\,cm^{-3}$ (middle) both emission lines and the underlying shape are well reproduced by the simulation. Simulations were done with FLYCHK [52].

It can be noted that short wavelengths, ergo emission from higher charged ions, can only be observed by the rear side mirror if the laser hits close enough to the edge of the foil. This is equivalent to the fact, that the hot regions of the plasma emerge only close to the center of the laser focus. The half width of the curve for each emission line of fig. 4.2 (top right) is determined. Results are depicted in fig. 4.2 (bottom). A fast decrease of emission intensity for higher energy photons with energies above 120 eV can be stated. These photons stemming from ionization states Al IV and Al V are only emitted up to a distance of 60 μm from the laser focus center. Lower energy photons are emitted at distances between 100 μm ($E_{ph} <$ 120 eV) and 450 μm. The spectra are now compared to simulated emission spectra obtained by the simulation software FLYCHK [52], which calculates ionization states and emission spectra of an element for a given T_e and n_e. A free-electron density of $n_e = 1 \cdot 10^{22}\,cm^{-3}$ is estimated from the general composition of the emission

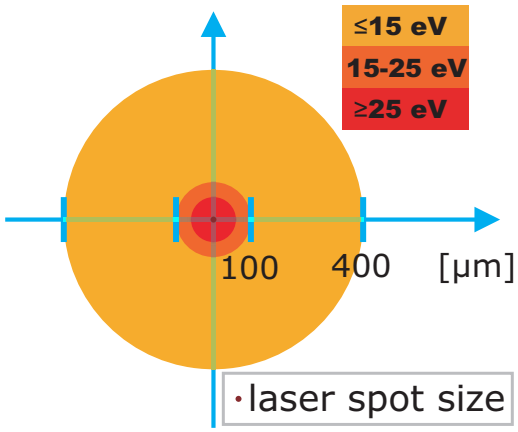

Figure 4.4: Simplified scheme of the free electron temperature T_e distribution in the plasma.

spectrum. Further explanation of this estimation can be found in fig. 4.3. Emission of photons with energies above 120 eV can only be expected for plasmas with a free-electron temperature exceeding $25 - 30$ eV. Emission of photon energies between $110 - 120$ eV is expected to be observed for a plasma at $T_e \approx 20$ eV and hotter. The lowest observed photon energies between $78 - 100$ eV will be emitted by a plasma of temperature $T_e \approx 15$ eV, according to the simulation.

Figure 4.4 displays a simplified scheme of the sizes of the measured temperature zones. An even higher free-electron temperature is expected for the center of the plasma. Since the focus of the laser spot is by two orders of magnitude smaller than the centroid of the 25 eV temperature zone, most of the laser pulse energy will be deposited in a small area around the focus. To gain more knowledge of the hot central part of the plasma a spectrometer that extends further into the short wavelength range would be necessary.

4.2 Simultaneous Multi-Angle XUV Spectroscopy

In this chapter an experiment to determine the non-linear dispersion function simultaneously for three different spectrometers is described. The experiment was carried out at the FLASH facility at DESY (Hamburg) in preparation of an XUV pump probe experiment. All spectrometers are equipped with an XUV flat field grating similar to the one described in chapter 3.3. Data and results in the following chapter have been basis for the publication *"In-situ determination of dispersion and resolving power in simultaneous multiple-angle XUV spectroscopy"* in *Journal of Instrumentation* [53]. A thus calibrated spectrometer can be used for experiments described in chapters 4.3 and 4.4.

In the experiment a commonly present material such as technical aluminum is used to create plasma emission lines from Al and Mg. Therefore an ultra short laser pulse at 800 nm is focused onto the aluminum block. Consequently spectral calibration of the spectrometers in the wavelength range from $10 - 19$ nm is possible. The μm sized plasma is observed simultaneously under different viewing angles by the spectrometers, enabling an in-situ cross-calibration of dispersion and spectral resolution. Subsequent laser plasma experiments do not require a change of the experimental setup. A comparison of the measured dispersion to ray tracing simulations is given at the end of the chapter.

4.2.1 Experimental Procedure

Dispersive Elements

Total external reflection gratings serve as a suitable dispersive element for the XUV wavelength range. In comparison to free-standing transmission gratings they do not imprint additional structures from a periodic support grid on the spectrum [42; 54]. In addition, the blazing of the gratings significantly increase the efficiency and a variable line spacing (VLS) leads to focusing of the spectral lines on a flat field [47; 55]. The efficiency of such a VLS grating for different incidence angles has been

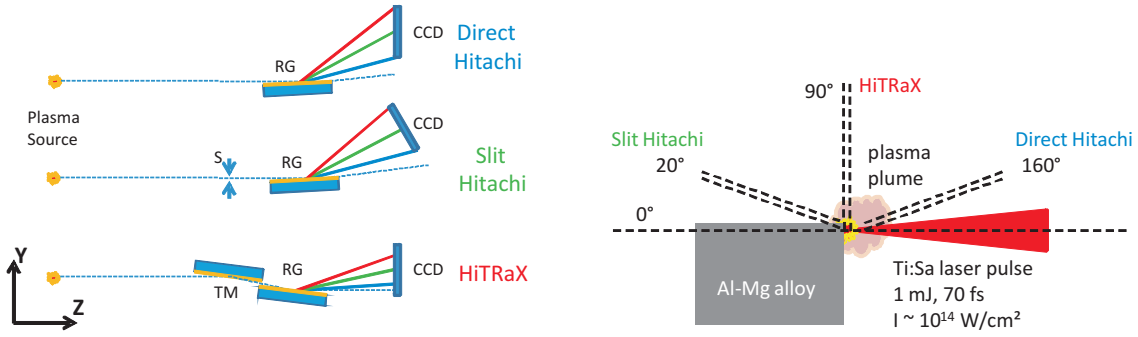

Figure 4.5: *Left:* Different schemes of XUV spectrometers that use a flat-field grating (RG): (Top) No further optical elements between the plasma source and the spectrometer, (Middle) A virtual source is introduced via an adjustable slit (S), (Bottom) A toroidal mirror (TM) in front of the grating images the source onto a CCD. *Right:* Scheme of the experimental setup. The laser pulse coming from the right is focused on the edge of a piece of technical aluminum. The plasma emission is observed under three different viewing angles by the XUV spectrometers [53].

measured and is further discussed in chapter 3.3.

Grating Spectrometers

In the following the three different spectrometer setups that have been used for the experiment discussed in this chapter will be described. All of them employ flat field VLS reflection gratings.

In the upper left part of fig. 4.5 the most simple scheme of a spectrometer is realized. In this case the plasma itself serves as the real source point. As a dispersive element serves the concave VLS grating (RG) [55], which properties are extensively discussed in chapter 3.3. It is commercially available. As described in chapter 3.3, the ideal source to grating distance is about 25 cm combined with an incidence angle of 3°. Due to mechanical limitations at the experimental station at FLASH the source to grating distance was set to 237 mm and the accompanying incidence angle on the grating was set to 3.4°. This way the flat field could be maintained. An Andor DO420 CCD was used as a detector for this spectrometer. The chip size is 1024×255 pixels and the pixel size is $26 \times 26\ \mu m^2$. In the non-dispersive direction the detector read-out was set to full vertical binning. For an improved signal to

noise ratio, an optical light filter in form of a 880 nm thick Zr-foil was mounted in front of the CCD.

The advantage of such a spectrometer setup is the large collection solid angle. In turn, the position of the source directly impacts the incidence angle on the VLS grating and thereby the dispersion and efficiency. I will refer to this spectrometer as the *Direct Hitachi*.

In the middle left in fig. 4.5 a simplified version of the spectrometer from chapter 3 is shown. Due to spatial restrictions of the experiment at FLASH the toroidal collection mirrors before the slit have been unmounted. Thus, the spectromter setup consists of the adjustable slit (S), the VLS grating (RG) [55] and a detector. A detailed description of distances and angles of the optical components from the slit to the CCD can be found in chapter 4.5. In comparison to the Direct Hitachi the detection solid angle is reduced due to the limited opening of the slit. In turn the spectral resolution can be increased when reducing the slit size. This also reduces the sensitivity towards source instabilities and extended source sizes. Long-time accumulations with a stable resolution can be achieved with a fixed slit size. In this experiment the slit size was set to 100 μm. A Zr-filter of 200 nm thickness is introduced in front of the VLS grating to block visible light. The detector, an Andor iKon CCD with with 2048×2048 pixels and a pixel size of 13.5×13.5 μm^2 was set to full vertical binning. As a consequence an asymmetric line profile could reduce spectral resolution and influence the dispersion if a plasma emission line is not perfectly straight on the CCD. To exclude such an influence, the straightness of a plasma emission line was observed in imaging mode of the detector and was found to be better than 3 pixels over the entire height of the camera. I will refer to this spectrometer as the *Slit Hitachi*.

In the bottom left of fig. 4.5 another spectrometer scheme is shown. This setup combines a toroidal mirror (TM) with a flat field grating and has been extensively discussed in reference [8]. An incidence angle of 7.5° on the grating and the proximity of the mirror to the source ensure a large solid detection angle. For the supression of optical light a Zr-filter of 250 nm thickness can be introduced in front of the detector.

An 800 l/mm grating (HORIBA) serves as a dispersive element. In combination with the toroidal mirror it is possible to observe both 0th order and dispersed diffraction orders on the detector, which makes it also a suitable XUV imaging system. A Princeton Instrument PIXIS CCD with 2048×512 pixels and a pixel size of 13.5×13.5 μm^2 serves as a detector. To reduce the read-out time, the detector is set to region-of-interest read-out mode. I will refer to this spectrometer as *Hitrax*.

To minimize thermal noise for all detectors, the CCDs were cooled to -50°C by air-cooled, fan-assisted, multi-staged Peltier elements.

Setup for Multi Spectrometer Characterization

A crucial part for the design and manufacturing of spectrometers is the performance of the dispersive element. In the case of XUV reflection gratings the parameters, such as line spacing, curvature [47; 55] or reflection efficiency, as measured in chapter 3.3 are typically well known. Hence, a detailed simulation and ray tracing analysis is feasible to determine possible spectrometer parameters such as distances and angles of optical elements. The performance of parameters that differ from standard values can also be evaluated.

Nevertheless, a detailed experimental performance check has to be conducted for every spectrometer built in the mechanical workshop. As can be seen from the results in chapter 3.3, careful adjustment of the incidence angle is needed for a reliable dispersion function. Along with that comes a detailed test of the detectable spectral window and the resolving power.

For the plasma spectroscopy experiments that will be discussed in chapters 4.3 and 4.4 strict time constraints applied at the user facility FLASH. In such a case the spectrometer is typically assembled right before the actual experiment, which bears the risk of mechanical uncertainties and consequently in uncertainties of the spectrometer performance.

As explained in chapter 3 a suitable calibration source for an XUV spectrometer should emit spectrally narrow lines at tabulated wavelengths. In addition, the source size needs to be fairly small in the range of a few ten-μm, in order to de-

termine the spectral resolution. The emittance of such an ideal calibration source should be isotropic in order to illuminate the entire toroidal mirror in case of the Hitrax spectrometer or the whole grating aperture in case of the Direct Hitachi and the Slit Hitachi. Conventional noble gas discharge sources exhibit typically a limited divergence and large source sizes and are therefore not suited for simultaneous determination of spectral dispersion. In the setup described here, the XUV source is present at the experiment and thereby accounts for the specific modifications at the experimental setup. The spectrometers are mounted to the experimental target chamber to observe the target chamber center (TCC) under different viewing angles of 20°, 90°, and 160° with respect to the incoming laser as shown in the right part of fig. 4.5. At TCC an edge of a target stage, which is made of technical aluminum serves as target material. An alloy of AlMgSi0.5 typical serves as material for drilling, turning and milling in mechanical workshops. Therefore this kind of technical aluminum is typically present close to the focal area, serving as target holder or part of the experimental setup. In contrast to gold and copper it does emit a high number of narrow spectral lines when irradiated with an optical laser of moderate intensity around 10^{14} W/cm^2. These ionic lines in the XUV range originate from Al and Mg [56].

To create the plasma a Ti:Sa laser [57] is focused onto the edge of the Al:Mg target holder. The focal spot has a diameter of approximately 60 μm. At a pulse duration of 70 fs and a pulse energy of 1 mJ an intensity of about 5×10^{14} W/cm^2 is reached at the target surface, where the plasma is created. A plasma plume is formed and expands after the surface plasma is created. Similar to considerations in chapter 3 the visibility of the emission lines is different for different viewing angles of the three spectrometers. Especially the Slit Hitachi will only observe weaker emission from the expanded outer parts of the plasma which are colder than the central parts. Due to the plasma expansion and the extended laser spot size the spectral resolution of Hitrax is limited.

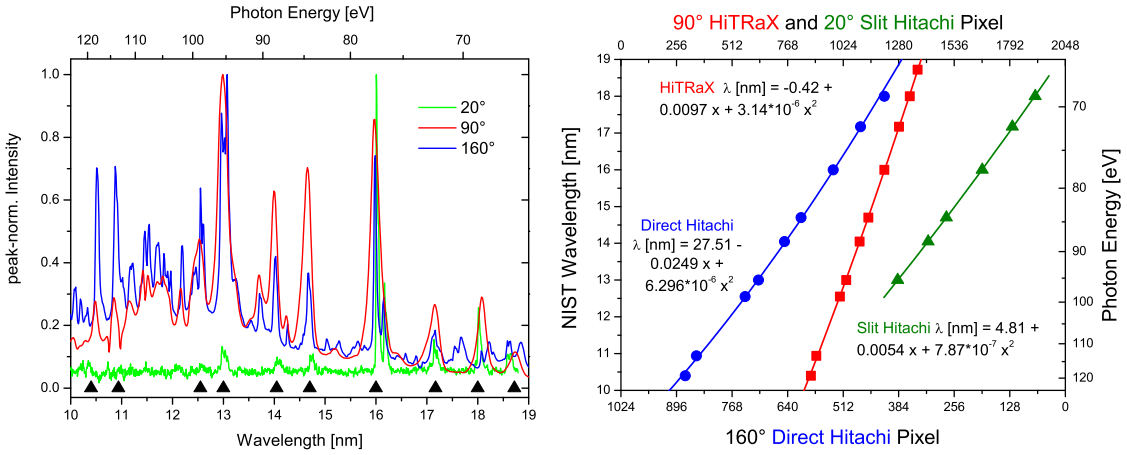

Figure 4.6: *Left:* Normalized intensity of the emission spectra observed under the different viewing angles by the respective spectrometers. To fit the dispersion function the lines marked with a black triangle were used. *Right:* Shown is the dispersion function for each of the spectrometers. Note that the lower x-axis holds for the direct Hitachi with the 1024 pixels, whereas the upper x-axis represents the 2048 pixels CCD for the two other spectrometers. Identified emission lines from the NIST database are marked accordingly [53].

XUV Emission Spectra and Dispersion Functions

XUV plasma emission spectra for the three spectrometers are displayed in fig. 4.6. The spectra comprise of 100 exposures each for a sufficient signal to noise ratio. Since the efficiency of Hitrax decreases below 9 nm and the transmission of the Zr filters decreases for wavelengths longer than 19 nm the spectra are only shown in a wavelength range from 10 nm to 19 nm.

While the Direct Hitachi and Hitrax observe a variety of emission lines from the hot plasma center, the Slit Hitachi detects only a few lines from the colder parts of the plasma plume. This can be explained by the shadowing effect of the target holder for a viewing angle of 20°. In this case also the continuum background is absent. Nevertheless, the doublet at 16 nm [56] is present in all spectra and can be used to estimate the spectral resolution.

To identify the tabulated emission lines and match them with the observed ones, the previously characterized Hitrax was used. Tabulated values are taken from the

atomic spectra database of NIST [51], their position is marked with black triangles in the left part of fig. 4.6. In the right part of fig. 4.6 the pixel position of these identified lines is marked for each spectrometer and a second order polynomial is fitted accordingly to match the observed emission lines. Thus determined dispersion functions are displayed in fig. 4.6, their first and second order coefficients, A_1 and A_2 are:

$$\begin{aligned} \textit{Direct Hitachi}: &\quad A_1 = (-2.49 \pm 0.02) \times 10^{-2} \quad \text{and} \quad A_2 = (6.3 \pm 0.8) \times 10^{-6}. \\ \textit{Slit Hitachi}: &\quad A_1 = (5.4 \pm 0.7) \times 10^{-3} \quad \text{and} \quad A_2 = (0.8 \pm 0.2) \times 10^{-6}. \\ \textit{HiTRaX}: &\quad A_1 = (9.7 \pm 1.5) \times 10^{-3} \quad \text{and} \quad A_2 = (3.1 \pm 0.7) \times 10^{-6}. \end{aligned}$$

Using the respective dispersion functions allows to identify the observed emission lines in the spectral range between 10 nm and 19 nm. Note that within this spectral range there are mainly transitions from Al IV-VI and for Mg I-IV, VII present.

Optimization of Ray Tracing Parameters

a mismatch is found comparing the measured dispersion functions of the Direct Hitachi and the Slit Hitachi to the expected dispersion from ray tracing simulations. The discrepancy is likely introduced by mechanical deviations, which can occur in the fabrication process, i.e. during soldering of tubes and flanges or during the assembly of the spectrometer, i.e. when screwing together support parts for grating and filter. In total, these uncertainties may add up to the order of 1 mm and thereby also influence the dispersion function. As can be seen from the scheme of the Direct Hitachi in fig. 4.5 also the Y-position of the grating should be considered important.

The Hitachi grating was implemented in the ray tracing software ZEMAX [58] and both the Direct and the Slit Hitachi were modeled. Best match between measured and ray traced dispersion can be found if the brightest Al emission lines are used to modify mechanical values in the software as follows.

Starting with the Slit Hitachi, at first the distance between maximum and minimum wavelength $\lambda_{max} = 18\,\text{nm}$ and $\lambda_{max} = 13\,\text{nm}$ was adjusted in the simulation by tilting the grating. The best match was found for an incidence angle of 3.085°. Compared to the design value of 3° there is only a difference of 3 %. After match-

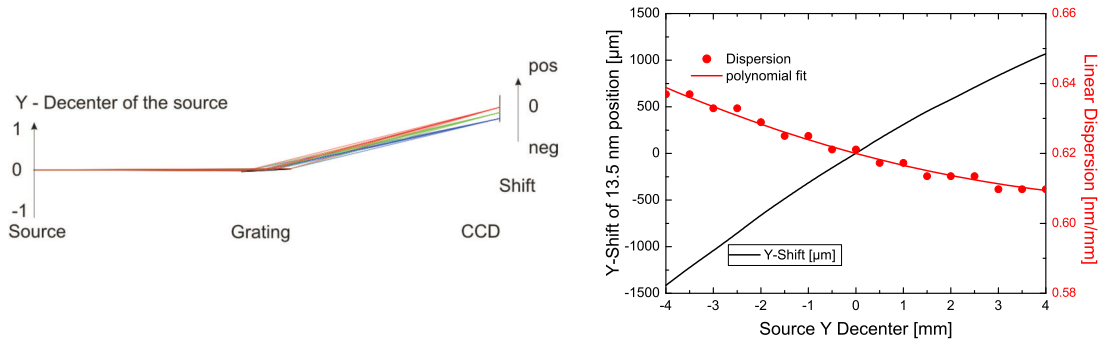

Figure 4.7: *Left:* Simulation of the Direct Hitachi with the ray tracing software ZEMAX. *Right:* Depending on the Y-position of the source also the 13.5 nm position shifts (left axis). The linear dispersion changes accordingly (right axis) [53].

ing the linear dispersion, the relative distances of the strong emission lines where compared and found to be in good agreement with the measured values. Thus, the optimization of the dispersion is complete.

To match the position of the spectrum on the CCD, in a next step the position of the detector itself was moved in the ray tracing software. Using the coordinate system introduced in fig. 4.5, the optimum focal distance is $Z = 256.5\,\text{mm}$ and the optimum translation in dispersion direction is $Y = 59.27\,\text{mm}$. Compared to the design parameters of $Z = 250\,\text{mm}$ and $Y = 58\,\text{mm}$ there is a notable discrepancy of 6.5 mm in Z. The reason lies in the assembly of the spectrometer, when a spacer was introduced under the grating. The spacer was used for fine adjustment of the rotation angle to match the incidence angle of 3°. Along with that comes a small displacement of the grating in Y-direction causing the beam to hit the grating slightly decentered. This leads to a longer beam path between grating center and detector. In this case a lift of only $\Delta Y = 0.35\,\text{mm}$ is needed to achieve the observed effect.

As mentioned, the Y-position of grating for the Direct Hitachi is a crucial parameter. CCD and grating were at fixed positions relative to each other, since no further XYZ-manipulator could be attached to the experimental chamber. Similar as in the aforementioned case, parameters of the simulation are adjusted. The dependency of the Y-parameter of the grating is shown in fig. 4.7. In the right part of fig. 4.7 the

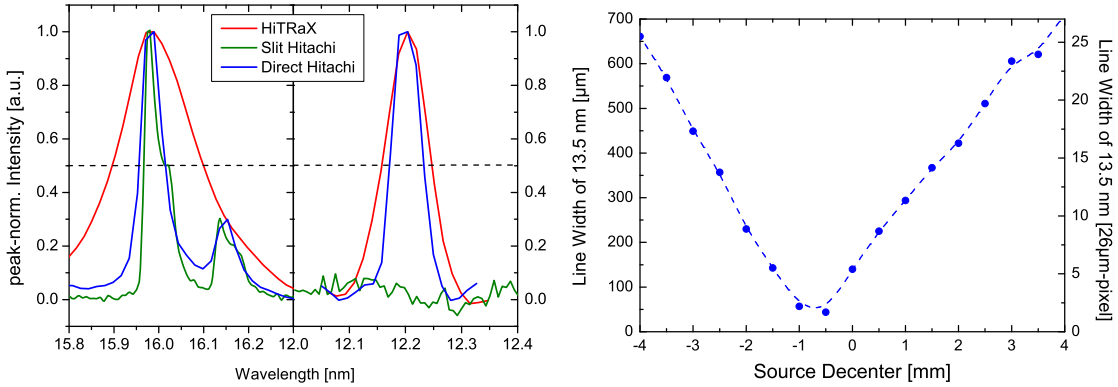

Figure 4.8: *Left:* Spectral resolution of the Al IV doublet at 16 nm (left) and of a single Mg V emission line at 12.2 nm (right). The FWHM is marked with a dashed line. *Right:* Simulation of the spot width as a function of source shift of monochromatic radiation at 13.5 nm for the Direct Hitachi. [53]

shift of the position of 13.5 nm on the CCD is shown for the corresponding Y-shift on the left axis. The right axis displays the change in linear dispersion, respectively. For 13.5 nm a Y-shift of the grating of ± 2 mm results in a $\pm 617\,\mu$m shift at the detector, while the dispersion changes only slightly by $\pm 1.25\,\%$.

For an estimation of the spectral resolution of the Direct Hitachi, the spot size of the 13.5 nm was determined using the ray tracing software. The right part of fig. 4.8 shows the linewidth of the 13.5 nm dependent on the Y-decenter of the source. At $Y = 0.5$ mm the narrowest line can be found, whereas for Y between ± 2 mm the line width varies from 230 μm to 44 μm and back to 422 μm. Since the flat field spectrometer is optimized for numerous wavelengths, the optimum line width for 13.5 nm is not found at $Y = 0$.

Spectral Resolution

For a benchmark of the spectral resolution of all three spectrometers two plasma lines are used as shown in the left in fig. 4.8. The doublet emission line of Al IV at 16 nm is used to determine the Full-Width-Half-Maximum (FWHM) of the Slit Hitachi $\delta_{\mathrm{SH}}\lambda = 0.05$ nm and the Direct Hitachi $\delta_{\mathrm{DH}}\lambda = 0.06$ nm, while the Hitrax spectrometer cannot resolve the doublet. Therefore, a Mg V emission line at 12.2 nm

is used to estimate a spectral resolution for Hitrax of $\delta_{\mathrm{Hi}}\lambda = 0.09\,\mathrm{nm}$. The Direct Hitachi has a spectral resolution of $\delta_{\mathrm{DH}}\lambda = 0.06\,\mathrm{nm}$ for this line, whereas the line is to weak to be seen by the Slit Hitachi in forward direction.

For the Direct Hitachi both lines at 12.2 nm and at 16 nm exhibit the same spectral resolution of $\delta_{\mathrm{DH}}\lambda = 0.06\,\mathrm{nm}$. The same increment of spectral resolution is therefore estimated for the Direct Hitachi. In case of the Hitrax spectrometer the determined resolution at the single 12.2 nm line should be in favor of the unresolved doublet. Since the spectrum is folded with an image of the source, the spectral resolution is reduced due to the source size of $50\,\mu$m and an expanded plasma. To achieve a higher resolution a decreased source size, i.e. by a smaller laser focus ($\leq 10\,\mu$m) is needed.

Finally, for the evaluation of the spectral resolution it should be noted that line broadening mechanisms should be considered. The Mg line and the Al doublet lower levels are ground states. A possible broadening could therefore be introduced by the opacity effect. Another contribution the line broadening could be Stark effect at the present electron densities. The measured spectral resolution of the spectrometers can thus be understood as a lower limit.

4.2.2 Summary of the Section

In this chapter an in-situ and simultaneous method for the cross-calibration of three spectrometers is presented. Resolution and non-linear dispersion of the different XUV spectrometers are determined at experimental conditions.

As an XUV source a laser created plasma from technical aluminum is used. The Al:Mg alloy is typically present at experimental setups in form of target holders, support stations, and others. In this case a moderate intense Ti:Sa laser was used. It should be noted, that the choice of the laser and certain parameters such as highest intensities or ultrashort pulses is not crucial for the presented method. A moderate intensity of $10^{14}\,\mathrm{W/cm^2}$ to create the plasma can be generated by most of the lasers present at experiments such as FEL experiments with optical probe, high-harmonic generation and plasma experiments. The plasma emission covers a wide spectral

range in the XUV. However, in this case the spectrometers are sensitive to 13.5 nm and around, which is a well explored range for lithographic applications.

The non-linear dispersion function of three different VLS grating spectrometers was determined in the wavelength range between 10 nm and 19 nm. For the Hitrax spectrometer with a toroidal mirror and a reflection grating with 800 l/mm a first order dispersion of 7.2×10^{-4} nm/μm was found. For the Direct Hitachi spectrometer with a curved VLS grating with 1200 l/mm the first order dispersion was measured to be 9.6×10^{-4} nm/μm, and for the Slit Hitachi 4.0×10^{-4} nm/μm was measured. The respective second order terms of the dispersion are more than 1000 times smaller. Furthermore, the spectral resolution was determined for different emission lines and an upper limit of $\delta\lambda = 0.06$ nm was found for the HITACHI gratings and $\delta\lambda = 0.09$ nm for the Hitrax spectrometer with a HORIBA grating.

Such on-site calibrated spectrometers can now directly be used for subsequent laser plasma experiments, without changing the experimental setup.

Table 4.1: The strongest observed XUV lines, as identified from the NIST atomic spectra database (ASD), for Al and Mg ions.

Observed Wavelength [nm]	NIST ASD Wavelength [nm]	Ion	Transition Configurations
10.50 ± 0.06	10.07	Mg VI	$2s^2 2p^3$ - $2s^2 2p^2 ({}^3P) 3d$
10.88 ± 0.06	10.85	Al IV	$2s^2 2p^6$ -$2s^2 2p^5 ({}^2P^\circ_{1/2}) 6d$
	10.89	Al IV	$2s^2 2p^6$ -$2s^2 2p^5 ({}^2P^\circ_{3/2}) 6d$
11.19 ± 0.08	11.15	Mg V	$2s^2 2p^4$ -$2s^2 2p^3 ({}^2P^\circ) 3d$
	11.17	Mg VI	$2s^2 2p^3$ -$2s^2 2p^2 ({}^3P) 3s$
11.45 ± 0.05	11.48	Mg V	$2s^2 2p^4$ -$2s^2 2p^3 ({}^2D^\circ) 3d$
11.54 ± 0.05	11.54	Mg V	$2s^2 2p^4$ -$2s^2 2p^3 ({}^2P^\circ) 3d$
11.71 ± 0.05	11.70	Mg VI	$2s^2 2p^3$ - $2s^2 2p^2 ({}^3P) 3s$
	11.72	Mg VI	$2s^2 2p^3$ - $2s^2 2p^2 ({}^3P) 3s$
12.20 ± 0.05	12.20	Mg V	$2s^2 2p^4$ - $2s^2 2p^3 ({}^4S^\circ) 3d$
12.43 ± 0.05	12.40	Al IV	$2s^2 2p^6$ -$2s^2 2p^5 ({}^2P^\circ_{1/2}) 4s$
	12.46	Al IV	$2s^2 2p^6$ -$2s^2 2p^5 ({}^2P^\circ_{3/2}) 4s$
12.55 ± 0.05	12.55	Al V	$2s^2 2p^5$ - $2s^2 2p^4 ({}^1D) 3s$
	12.61	Al V	$2s^2 2p^5$ - $2s^2 2p^4 ({}^1D) 3s$
	12.56	Mg V	$2s^2 2p^4$ - $2s^2 2p^3 ({}^2D^\circ) 3d$
12.95 ± 0.05	12.97	Al IV	$2s^2 2p^6$ -$2s^2 2p^5 ({}^2P^\circ) 3d$
13.05 ± 0.05	13.04	Al V	$2s^2 2p^5$ - $2s^2 2p^4 ({}^3P) 3s$
	13.08	Al V	$2s^2 2p^5$ - $2s^2 2p^4 ({}^3P) 3s$
13.73 ± 0.05	13.72	Mg V	$2s^2 2p^4$ - $2s^2 2p^3 ({}^2D^\circ) 3s$
	13.74	Mg V	$2s^2 2p^4$ - $2s^2 2p^3 ({}^2D^\circ) 3s$
14.04 ± 0.05	14.04	Mg IV	$2s^2 2p^5$ - $2s^2 2p^4 ({}^1D) 3d$
14.70 ± 0.05	14.06	Mg IV	$2s^2 2p^5$ - $2s^2 2p^4 ({}^1D) 3d$
16.00 ± 0.05	16.01	Al IV	$2s^2 2p^6$ - $2s^2 2p^5 ({}^2P^\circ) 3s$
16.14 ± 0.05	16.17	Al IV	$2s^2 2p^6$ - $2s^2 2p^5 ({}^2P^\circ) 3s$
17.15 ± 0.08	17.14	Mg III	$2s^2 2p^6$ - $2s^2 2p^5 ({}^1P^\circ_{3/2}) 4d$
	17.17	Mg IV	$2s^2 2p^5$ - $2s^2 2p^4 ({}^1D) 3s$
18.02 ± 0.08	18.01	Al IV	$2s^2 2p^5$ - $2s^2 2p^4 ({}^3P) 3s$
	18.06	Al IV	$2s^2 2p^5$ - $2s^2 2p^4 ({}^3P) 3s$
18.62 ± 0.10	18.65	Mg III	$2s^2 2p^6$ - $2s^2 2p^5 3d$
	18.72	Mg III	$2s^2 2p^6$ - $2s^2 2p^5 3d$

4.3 Determination of Free Electron Temperature from XUV – Bremsstrahlung Spectroscopy

Data and results in the following chapter have been reported in the publication *"Ultrafast electron kinetics in short pulse laser-driven dense hydrogen"* [59]. The experiment was carried out at the FLASH FEL at DESY (Hamburg).

To evaluate the heating of a cryogenic dense hydrogen target by an intense ultrashort infrared laser pulse, XUV bremsstrahlung spectroscopy can be a useful tool. The following part will report on an experiment that employs XUV spectrosocopy in the spectral range of $8 - 18\,\mathrm{nm}$. Best fit of the corrected spectra can be found by comparison to a simulated two temperature model, with free electron temperatures of $\sim 13\,\mathrm{eV}$ and $\sim 30\,\mathrm{eV}$. The measured temperatures in the dense hydrogen plasma are compared to simulations.

4.3.1 Setup and Experiment

The Hydrogen Target

One of the most demanding tasks in vacuum high repetition rate laser plasma experiments is the supply of a pristine free standing target for every laser pulse. In this experiment a jet of cryogenic liquid hydrogen is used for that purpose. The liquid jet is generated by pressing hydrogen gas at $\sim 2\,\mathrm{bar}$ through a nozzle of $5\,\mu\mathrm{m}$ diameter. A helium flow cryostat is attached to the nozzle to cool down the hydrogen to $\sim 20\,\mathrm{K}$ and thereby liquefy the gas. Surface tension and small fluctuations at the liquid jet will cause an unstable flow. After a certain propagation length the Rayleigh breakup will destroy the jet [60] and the remaining droplets will eventually freeze after a few millimeters by evaporational cooling. For control over the position of the hydrogen jet in the vacuum chamber, the cryostat is attached to a three dimensional manipulator. In this experiment the position of the nozzle is chosen such that the interaction point is about $1 - 2\,\mathrm{mm}$ in front of the nozzle. A residual gas pressure of the order of $10^{-6}\,\mathrm{mbar}$ is measured in the vacuum chamber.

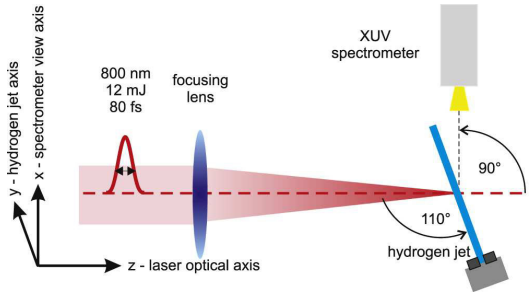

Figure 4.9: Scheme of the setup. The horizontally polarized laser is focused under an angle of 110° onto the hydrogen jet. The XUV spectrometer is fixed at an angle of 90° to the Ti:Sa laser [59].

The Ti:Sa Laser

To create a sufficiently high free electron density and free electron temperature the FLASH pump probe laser system and in particular the Ti:Sa system is used [57]. Laser parameters, relevant for the experiment are as follows. In a first step ultrashort pulses are produced by a Ti:Sa laser oscillator. In a second step these pulses are amplified up to 20 mJ by a chirped pulse amplifier system, consisting of a regenerative and a two-pass amplifier. To compensate for the break up of the beam into filaments due to the propagation in air, the laser pulse is re-compressed using a transmission grating setup after transportation to the experimental chamber. To generate a plasma from the cryogenic droplets, the laser pulses at 800 nm and a repetition rate of 10 Hz are focused with a lens to a spot size of $\sim 30\,\mu$m FWHM. After recompression the laser energy is measured to be ~ 12 mJ and a pulse duration of (80 ± 20) fs is determined by using an auto-correlator setup. The resulting energy on the target can thus be estimated to be $I = 2 \cdot 10^{16}\,\mathrm{Wcm}^{-2}$. Figure 4.9 displays the experimental setup. Optical laser and liquid hydrogen jet merge under an angle of about 110°, where the laser is linearly polarized in the plane of the hydrogen jet.

The XUV Spectrometer

For the detection of soft x-ray radiation the spectrograph HiTRaX [8] was attached to the vacuum chamber under an angle of 90° with respect to the optical laser and the

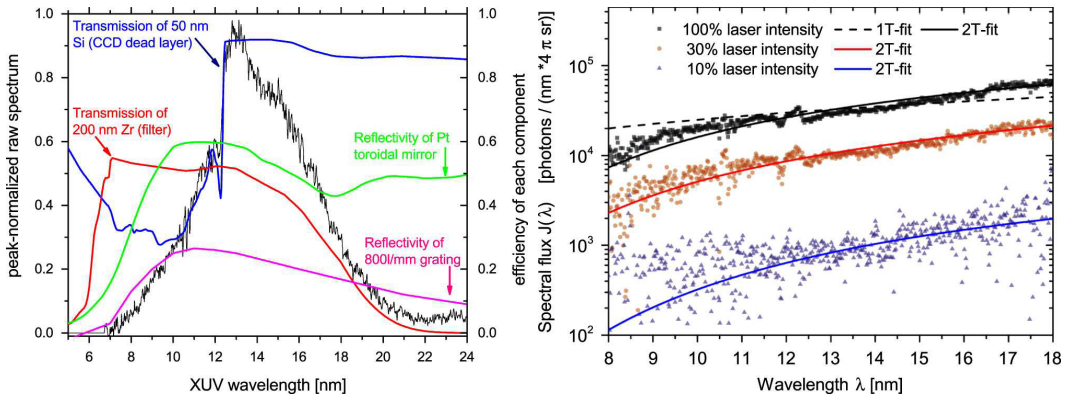

Figure 4.10: *Left:* Background corrected XUV bremsstrahlung emission spectrum (solid black). Coloured lines mark the efficiency of single optical components included in the spectrometer *Right:* The black, blue and red points mark the measured spectral flux of the emitted XUV-bremsstrahlung from the hydrogen target. Solid and dotted lines are bremsstrahlung fits to the data. [59]

hydrogen jet as depicted in fig. 4.9. The spectrometer covers a wavelength range of $5-35\,\mathrm{nm}$ and comprises a toroidal mirror and a variable line space reflection grating. A Princeton Instruments back-illuminated CCD camera with a 2048×512 pixel chip and a pixel size of $13.5\times13.5\,\mu m^2$ serves as a detector. A spectral resolution of $\lambda/\Delta\lambda = 330$ has been measured for this spectrometer [8]. For a detailed description of the determination of the dispersion function see chapter 4.2.

4.3.2 Experimental Results

As mentioned above the optical laser was operated at a repetition rate of 10 Hz. Acquisition time of the detector was set to 60 s to accumulate over 600 spectra. Throughout the experiment the laser was operated in three different modi which were full intensity, i.e. $2\cdot10^{16}\,\mathrm{Wcm^{-2}}$, as well as 30 % and 10 % intensity. The black line in fig. 4.10 (left) shows a background corrected profile for a run with full laser intensity. The left part of fig. 4.10 also shows the wavelength dependence of the different optical components of the spectrometer. A Zr-foil of 200 nm thickness which is introduced in the beam path to block residual optical light from the detector exhibits a transmission range between 6 and 22 nm. The steep step in

the recorded spectra at 12.3 nm can be attributed to a Si L absorption edge which stems from absorption of the silicon CCD chip. A layer thickness of 50 nm Si is deduced from the step size of the Si L edge. After correction for the different optical components of the spectrometer a smoothened spectrum as in fig. 4.10 (right) is obtained. The experimental data for full (black squares) and 30% laser intensity (red circles) from fig. 4.10 still show a small peak in spectral flux around 12 nm, which can be explained as residual feature from the correction of the measured spectra with finite resolution compared to the infinitely sharp edge of the tabulated absorption data. A single temperature bremsstrahlung spectrum is now fitted to the full intensity spectrum and a temperature of $k_{\mathrm{B}}T = 4.9\,\mathrm{eV}$ is determined for the best fit. As can be seen from the dashed line fig. 4.10 (right) the single temperature fit cannot reproduce the characteristics of the measured spectrum in the observed spectral range, especially for low and high photon energies. Using two different independent temperatures T_1 and T_2 to fit the measured data yields an improved agreement between measurements and fit. For the fit of the data both temperatures weighted as T_2/T_1. In fig. 4.10 (right) the resulting spectra are displayed as solid lines. The following temperatures and their respective weight were determined:

Intensity	$k_{\mathrm{B}}T_1$	$k_{\mathrm{B}}T_2$	weight T_2/T_1
10%	14.5 eV	26.5 eV	0.540
30%	12.4 eV	31.9 eV	0.179
100%	14.1 eV	33.3 eV	0.418

These fitted parameters can be interpreted as the superposition of two bremsstrahlung spectra emitted by a free electron plasma at a temperature of $12.4 - 14.5\,\mathrm{eV}$ and a second plasma with electrons at a temperature of $26.5 - 33.3\,\mathrm{eV}$.

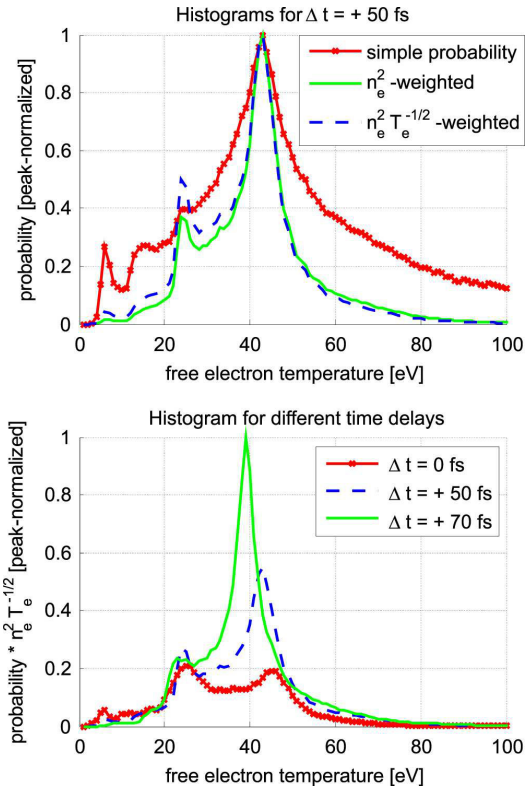

Figure 4.11: *Top:* Shown in red is the probability for an electron to be allocated to a certain temperatue in the histogram. Refer to the text for the weighted probabilities in green and blue. These simulations are calculated for a delay of $\Delta t = +50\,\mathrm{fs}$. *Bottom:* Simulation of a $n_e^2/\sqrt{T_e}$-weighted temperature distribution in the droplet for time delays $\Delta t = 0\,\mathrm{fs}$, $\Delta t = +50\,\mathrm{fs}$, and $\Delta t = +70\,\mathrm{fs}$ [59].

4.3.3 Comparison to Simulations

For a qualified interpretation of the two temperature fit particle-in-cell (PIC) simulations which model the experimental parameters have been carried out [59]. These simulations show that in the beginning of the heating process, when the leading edge of laser pulse hits the hydrogen droplet, only the surface of the droplet is ionized and heated. Due to this surface heating of the electrons within a skin depth of a few tens of nm, ionization and therefore free electron density and free electron temperature is strongly elevated in the outer shell of the droplet yielding a strong free electron temperature and density gradient. With times $> 50\,\mathrm{fs}$ after the laser pulse, heat is

transported towards the center of the droplet by free electrons. Bremsstrahlung is emitted when free electrons collide with protons and electrons. The probability to find electrons of a certain temperature in the droplet at a delay of 50 fs is shown in a histogram with 1 eV bins as the red curve in fig. 4.11 (top). For a temperature of $\sim$ 43 eV the highest probability can be found. The free-free emissivity of the bremsstrahlung scales as $J_{ff} \propto n_e^2/\sqrt{T_e}$ [61]. Hence regions with elevated free electron density contribute stronger to the spectrum when weighted with respect to these as can be seen from the green line in fig. 4.11 (top). Also regions with lower temperatures contribute stronger to the bremsstrahlung spectrum when weighted in addition as can be seen in the blue curve in fig. 4.11 (top). A thus weighted emission spectrum exhibits two major peaks at 25 eV and 43 eV and a decreased contribution of high temperature electrons > 80 eV and low temperature electrons < 20 eV. Interpreting the PIC simulations it can be assumed that the dominant temperature of 40 eV stems from the surface heated electrons within the skin depth, whereas the colder temperature of 25 eV represents an average temperature of equilibrated electrons in the dense regions of the target. In the lower part of fig. 4.11 the free electron density and temperature weighted probabilities of electrons in the droplet are shown for three different time delays. In the simulation the peak intensity of the pulse irradiates the surface of the droplet at $\Delta t = 0$ fs, corresponding to the red curve. With progressing time, the peak of the higher temperature rises by a factor of 5, while the temperature shifts to slightly lower value of 39 eV as in the green curve of fig. 4.11 (bottom). For times > 70 fs there is no further energy transfer from the laser pulse to hydrogen droplet.

Even though the experimental observation of two pronounced temperatures is in agreement with the results from the PIC simulations, the overall temperatures are 25-50% higher in the case of the simulation. In the calculation of the electron temperature from the PIC results, all electrons have been accounted for, including the hot ones which do not contribute to a physically relevant temperature in the sense of a Maxwell distribution. These yield an overestimation of the plasma temperature. Also, the PIC simulations do not account for Coulomb collisions, which alter the

energy partition towards higher free-electron densities and lower electron temperatures. Effects like laser pre-pulses on the few-nanosecond time scale potentially alter the heating mechanism. In the experiment, pre-pulses at $1 - 2$ ns before the main pulse have a measured intensity contrast ratio of a few 10^{-4}, but were neglected in the PIC simulations. The good agreement between experiment and simulation indicates that in this case pre-pulse heating does not seem to play a relevant role for XUV bremsstrahlung spectroscopy as a reliable plasma diagnostics.

4.4 Equilibration Dynamics and Conductivity of Warm Dense Hydrogen

Data and results in the following chapter have been basis for the publications *"Equilibration dynamics and conductivity of warm dense hydrogen"* [62] and *"Resolving Ultrafast Heating of Dense Cryogenic Hydrogen"* [44]. The experiment has been carried out at the FLASH FEL at DESY (Hamburg).

4.4.1 Setup and Experiment

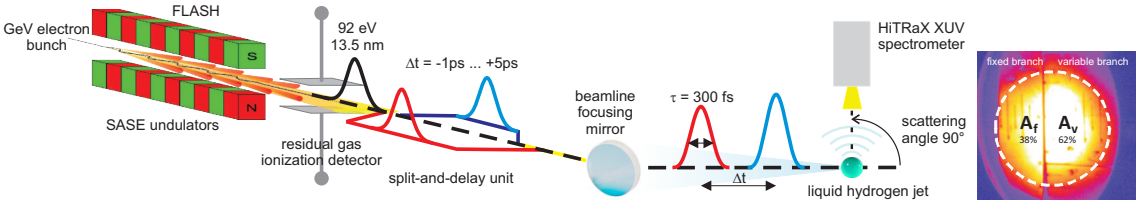

Figure 4.12: *Left:* The experimental setup at the split-and-delay beamline at FLASH [44]. Before focused onto a cryogenic hydrogen jet, the FEL pulse is split in a wavefront division setup. Both parts of the beam can be delayed with respect to each other. Scattering at 90° is observed with an XUV spectrometer. *Right:* The split ratio of the fixed and the variable arm can be determined from the geometrical areas A_f and A_v of the split-and-delay unit [62].

To investigate the evolution of a warm and dense matter state plasma in time, a pump-probe x-ray scattering experiment serves as a versatile tool. Especially the unique properties of FELs, such as ultra short pulse lengths and high repetition rate along with high peak brightness are suitable to create the warm dense matter state via volumetric heating of a cryogenic target. Such an excited state is then probed with a second pulse at a well defined delay time. A schematic of the experimental setup is shown in fig. 4.12 (left). Before focused onto the cryogenic target, the XUV FEL pulses are split and delayed with respect to each other in a split-and-delay unit implemented at the FLASH beamline [63]. The focusing mirror at the end of the split and delay unit focuses both beams to a focal spot area of $20 \times 30\,\mu\text{m}^2$ at the target. Throughout the experiment the FEL was operated at a repetition

rate of 10 Hz and a photon energy of $E = 92\,\mathrm{eV}$. The spectral bandwidth was measured to be $\Delta E/E = 1.6\,\%$ and a pulse length of $\leq 300\,\mathrm{fs}$ is estimated from the electron bunch duration. To measure the XUV pulse energies a residual gas detector is implemented at the beamline upstream the split-and-delay unit. An average pulse energy of $(200 \pm 50)\,\mu\mathrm{J}$ was measured there. Between pump and probe pulse a time delay of few fs-precision is introduced. The relative geometrical areas A_f and A_v of fixed and variable branches as shown in fig. 4.12 (right) give rise to different intensities at the target. Depending on the tabulated transmission of the beamline components, intensities of $(27 \pm 0.6)\,\mathrm{TW/cm^2}$ for the variable branch and $(19 \pm 0.4)\,\mathrm{TW/cm^2}$ for the fixed branch are estimated [9; 63]. As mentioned above cryogenic hydrogen droplets with a radius of $(9 \pm 2)\,\mu\mathrm{m}$ serve as homogeneous targets with a mass density of $0.08\,\mathrm{g/cm^3}$ ($5 \times 10^{22}\,\mathrm{cm^{-3}}$) and a temperature of 20 K. Hydrogen streams out of the cryostat with a velocity of 60 m/s. Therefore, each XUV pulse scatters from a different and thus unperturbed target. The target chamber is at a pressure of 10^{-5} mbar during the experiment. For a more detailed description of the cryogenic hydrogen source refer to section 4.3.1. The scattering signal is collected with an XUV sensitive spectrometer [8] at a scattering angle of $(90 \pm 2.2)^\circ$. For a detailed description of the *in-situ* calibration of the spectral dispersion refer to chapter 4.2.

4.4.2 Experimental Results

To obtain a sufficiently strong signal at the spectrometer detector, spectra for each delay are accumulated over 300 consecutive shots. Since the FEL is horizontally polarized, scattering is observed at a 90° angle in the vertical plane. Scattering spectra are collected for different time delays up to 5 ps. Figure 4.13 shows spectra for different time delays. A significant increase of the total scattered intensity between 0 ps and 5 ps is found. The change of the spectral shape in the higher and lower energy range can be attributed to fluctuations of the incident FEL spectrum. In this case the use of a spectrometer is preferable to distinguish between scattered XUV light and self emission of the plasma which spans over a broader spectral range.

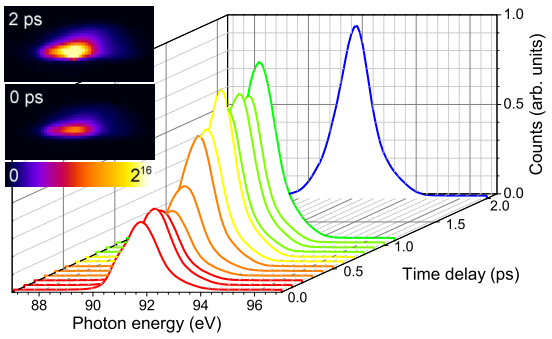

Figure 4.13: Pump-probe scattering spectra in dependence of the time delay. Two 16-bit raw spectra of 25×50 pixels of $(13.5\ \mu\text{m})^2$ size are shown in the inset. The spectral axis is oriented horizontally as in the graph. The spectra in the inset are integrated along the vertical axis to obtain spectral profiles [62].

4.4.3 Interpretation of the Data

Figure 4.14 displays the number of scattered photons per solid angle which was deduced from the estimated incoming photons and the solid angle of the spectrometer including the spectrometer throughput [44; 8]. Each data point represents the mean value of 300 exposures, with the root mean square deviations as their error bars. A strong pump-probe delay dependence for both cases (19 TW/cm^2 pump intensity and 27 TW/cm^2 probe intensity and vice versa) can be observed. For times shorter than 1 ps, the scattered photon fraction rises. For the lower pump intensity time delays up to 5 ps were realized. In this case, the scattering amplitude stopped growing between 1 ps and 2 ps and then decreases between 2 ps and 5 ps.

Photons with an energy of 92 eV arrive with the FEL. Since the ionization energy of hydrogen is 14 eV, photo ionized electrons will have an initial kinetic energy of 78 eV. Already during the pulse duration these electrons will ionize other atoms by impact ionization and thereby lead to a homogeneously heated sample [26]. With progressing time these electrons will transfer their kinetic energy to other particles like atoms, molecules, and ions in the sample. Consequently, depending on the delay, the probe pulse will hit either of the two different regimes. At earlier times a well ordered cryogenic system is present. This system exhibits a predominant particle distance of the intermolecular distance between the two hydrogen atoms. At longer

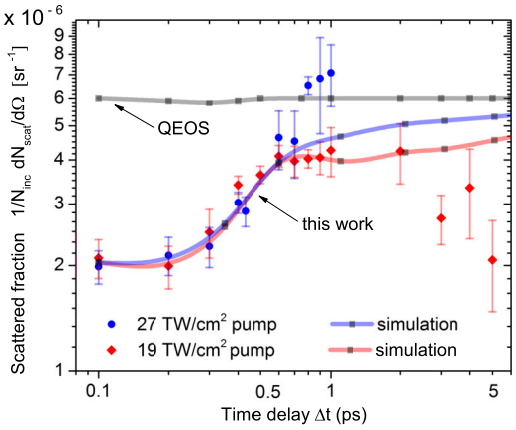

Figure 4.14: Blue points represent measured pump-probe data for a pump intensity of 27 TW/cm^2 and a probe intensity of 19 TW/cm^2, whereas the red points represent the inverse case with less intense pump. The lines compare predictions from simulations. The grey line is based on a quotidian equation of state (QEOS), while the red and blue lines are based on a Saha-like ionization model [62; 44].

delays a rather dissociated system similar to an ideal plasma with uncorrelated randomly distributed particles is probed. For an ideal gas-like plasma the scattered fraction will be larger than for a correlated system as the cryogenic hydrogen [13].

The measured dynamics of scattered photons can be used to benchmark different models of ionization. In this case simulations using a quotidian equation of state (QEOS) including a Thomas-Fermi model, gives rise to a much faster increase of the scattered fraction, which happens during the FEL pulse duration. Simulated results from the QEOS model are represented by the grey line in fig. 4.14. Since the Thomas-Fermi model yields a high ionization rate even at low temperatures, the energy transfer between electrons and ions is drastically increased and thus cannot be applied to cryogenic hydrogen in order to predict the dynamic scattering behavior. Using a Saha-like equation of state to model the ionization of cryogenic hydrogen leads to a slower increase of scattered photons. Simulations for two different pump intensities I_p are shown as red (I_p =19 TW/cm^2) and blue (I_p =27 TW/cm^2) lines in fig. 4.14. The underlying mechanism for the slower decrease is the weaker ionization of the hydrogen due to the Saha model, yielding only a weak transfer of energy between electrons and ions. Consequently, the signal of scattered photons increases slower and resembles the experimental observation.

4.5 Summary of the Spectrometry Chapter

A proof of principle experiment is discussed in chapter 4.1 to demonstrate the applicability of the multi angle spectrometer. The two collection mirrors observe forward and backward emission from a laser generated Al plasma. Numerous Al emission lines can be used to cross calibrate the spectra from either mirrors. Moving the Al-foil, further resolves the interdependency between forward and backward emission. Comparing the spectra to simulated emission spectra obtained by the collisional-radiative code FLYCHK, the spatial extension of different temperature zones in the plasma can be estimated. A central zone of $d = 120\,\mu$m diameter with a free electron temperature of $T_e > 25\,$eV, an intermediate zone of $d = 120 \ldots 200\,\mu$m with $T_e = 15 \ldots 25\,$eV and an outer zone of $d = 200 \ldots 900\,\mu$m with $T_e < 15\,$eV can be identified.

An experiment to simultaneously cross calibrate three different XUV spectrometers is described in chapter 4.2. Using emission lines from a laser generated plasma from a Al:Mg alloy, the non-linear dispersion function of all spectrometers is determined in-situ. The three spectrometers, which are all equipped with a flat-field grating, observe the plasma under angles of 20°, 90°, and 160°, compared to the incidence direction of the optical laser. Due to the shadowing effect of the solid target, the relative intensity of the emission lines varies between the different spectrometers and their observation angles. Emission lines between 10 nm and 19 nm can be identified.

A focusing flat-field XUV spectrometer was used to measure bremsstrahlung from a hydrogen plasma in chapter 4.3. The plasma is created by Ti:Sa Laser at 800 nm that is focused onto cryogenic hydrogen droplets. Characteristics of the optical components are accounted for in the analysis of the spectra. Best fit to the corrected spectra is achieved by a two temperature fit at free-electron temperatures of $T_1 \sim 13\,$eV and $T_2 \sim 30\,$eV. This can be explained by PIC simulations, showing that heating of the electrons is constrained to the droplet skin, leaving a relatively cold core. Weighting the simulated temperature distribution within the droplet with

$n_e^2/\sqrt{T_e}$ shows two dominant temperatures at $\sim 25\,\mathrm{eV}$ and $\sim 40\,\mathrm{eV}$ at delay times of 70 fs after the laser maximum. Both simulation and experiment show indication for different zones with different free-electron temperatures within the plasma. The remaining discrepancy that shows higher temperatures in the simulation can be explained by hot, non-Maxwellian electrons in the calculation, as well as missing energy-loss channels in the simulations.

In chapter 4.4 an XUV FEL pump – XUV FEL probe experiment is described where cryogenic hydrogen with a solid density of $0.08\,\mathrm{g/cm^3}$ is heated isochorically via XUV FEL pulses. The free electron plasma is created by a soft x-ray burst of duration $\leq 300\,\mathrm{fs}$ and probed at variable delays between 0 ps and 5 ps. The sample structure of the plasma causes different total scattered fractions of the probe pulse. Depending on the time delay the probe pulse will mainly be scattered by undissociated molecular hydrogen with a fixed distance between the atoms, or by an uncorrelated randomly distributed plasma. The latter case causes a larger diffusely scattered fraction of the incoming probe beam. The rise time of the scattering signal can be used to benchmark different ionization models. In the case of cryogenic hydrogen, a Saha-like equation of state to model the ionization is in favor of a quotidian equation of state (QEOS) that is based on a Thomas-Fermi model. The rise time of the scattered signal predicted by QEOS is much faster than observed in the experiment. Since the Saha model predicts a lower ionization degree, less free electrons are created in this model. As a consequence there are less collisions and a weaker transfer of energy between electrons and ions. Thus, a more precise rise time is predicted by the Saha model.

5. A Multi-Angle XUV Diode Array

A summary of a diode array (DA) is given in this chapter. With the results and insight from measurements described in chapter 4.4 and in the references [44] and [45] the complementary use of a multi angle diode array and the XMAS is motivated. Besides Thomson scattering from the free-electron plasma also Mie scattering can occur in scattering experiments. Since Mie scattering is a strongly decaying function for larger scattering angles, an angularly resolved measurement of the total scattered fraction is needed to distinguish between the scattering regimes. With the described diode array the scattered XUV-intensity can be measured simultaneously as a function of scattering angle.

5.1 Description of Individual Parts and Geometry

The active area of the diodes is a 10 mm × 10 mm square with a shunt resistance of 10 MΩ and a capacity of 20 nF at 0 V. To block visible wavelengths and prevent mismeasurement the nitrided metal silicide front window of the diode is coated with a 100 nm Si and a 200 nm Zr layer on top. According to [48] for $\lambda = 800\,\mathrm{nm}$ a transmission of $T \approx 10^{-8}$ and for $\lambda = 13.5\,\mathrm{nm}$ a transmission of $T \approx 0.42$ is expected and thus significantly improves the signal-to-noise ratio. A response time of 10 μs for gating between 10 % and 90 % is stated. The diode array comprises 8 diodes arranged on an arc with radius r = 62.5 mm. The angular distance between each diode is $\alpha = 18.1\,^\circ$, so that the DA covers a total angular range of $126.7\,^\circ$ (see

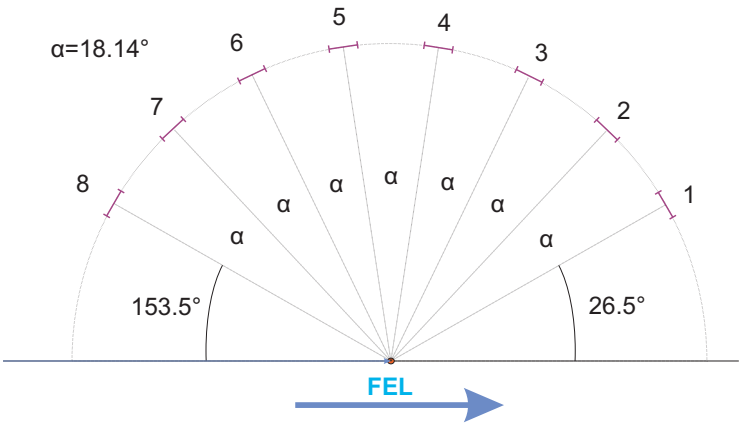

Figure 5.1: A scheme of the diode array. 8 Diodes are arranged on a segment of a circle. each with an angular distance of 18.1 ° to the neighboring diode. The array thus covers total angular range of 126.7 °.

fig.5.1). Two steel meshes are mounted 3.5 mm and 8.5 mm in front of the diodes to repel charged particles, such as electrons emerging from the interaction point. To create an electric field between the meshes, they are connected to a high voltage power supply, that provides a voltage between −1 kV and +1 kV. Depending on the relative position of the meshes with respect to each other there is a shadowing effect. The maximum shadowing amounts up to 36 %, but smaller values are possible. In addition all high voltage cables are electrically shielded to prevent an influence on the diode currents. For a simultaneous readout of the respective voltage over the diodes a multi function data acquisition (DAQ) system for USB is used. The 16 analog inputs each with a resolution of 16 bits and a maximum readout rate of 250 kS/s aggregated for all channels, exhibit an absolute accuracy of 2.69 μV at full scale (-10 V ... +10 V). Upstream of the DAQ a sample and hold (S/H) circuit maintains the diode voltage long enough for the data acquisition to read out. The shunt resistance of the S/H can be changed via jumpers (50 Ω, 1.1 kΩ, 1 MΩ). If the diodes are used in pulsed laser experiments a trigger from the laser source is needed to control the S/H mechanism.

A clamping arm at the diode array can be directly attached to an already existing spectrometer. Spectrometer and DA are aligned towards the same interaction point.

5.2 Calibration

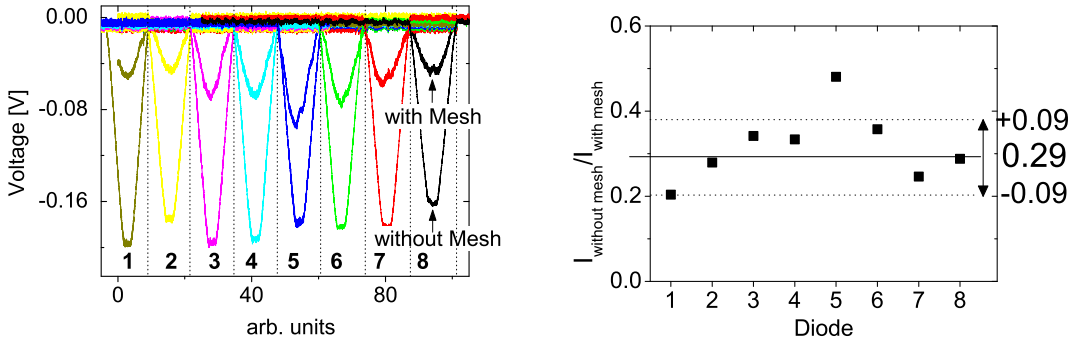

Figure 5.2: *Left:* A comparison of the sensitivity of the XUV diodes with and without the mesh in front of it. Diodes are numbered 1 to 8. Between 50 % and 80 % of the XUV radiation is blocked by the meshes. *Right:* Comparison of I_{max} with and without mesh to evaluate the shadowing of the mesh. The mean transmission of the mesh over all diodes amounts to (29 ± 9) %.

To analyze the influence of the mesh on the measurement a comprehensive calibration experiment was carried out using a microfocus XUV tube at 13.5 nm which is described in section 2.2.1. Due to the continuous emission of the XUV tube, the diode voltage can be read out directly via an oscilloscope. For the experiment the DA was mounted on a rotation stage in such a way, that during rotation each diode faces the XUV source consecutively. Figure 5.2 shows the photovoltage for each diode with and without mesh in front of the diode array. Shadowing of the diodes between 50 % and 80 % due to the two overlaying meshes can be stated. This value lies well above the calculated value of 36 % and can be explained by an inevitable offset of both meshes with respect to each other due to the slightly different radii of the surface curvature.

5.3 A Pump – Probe Experiment Using the Diode Array

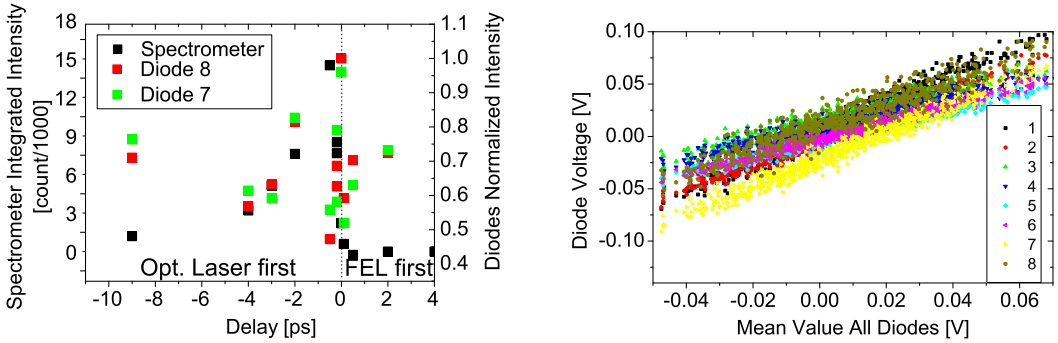

Figure 5.3: *Left:* Comparison of the delay dependent scattered intensity towards the spectrometer and diodes 7 and 8 looking in back scattered direction. *Right:* Correlation of the diode signals. The diode signal for each single diode is plotted against the mean value for all diodes of the corresponding shot.

The DA was applied during a pump-probe experiment at FLASH. Both optical-pump-FEL-probe and FEL-pump-FEL-probe data was taken. The setup of the experiment consisted of a cryogenic copper nozzle, that inserted a stream of liquid hydrogen (lH_2) droplets into a vacuum chamber. Perpendicular to the hydrogen beam, the copropagating pump and probe beams were inserted into the chamber. Due to place issues and other diagnostics in the vacuum chamber the DA is rotated out of the perpendicular plane by 27 °. According to fig. 5.1 the diodes are placed along the FEL direction. The left part of fig. 5.3 shows a comparison of integrated spectrometer intensity and two of the diodes signals. Displayed is delay dependent data for the optical-pump-FEL-probe experiment. Despite of the Zr-coating a strong influence of the optical pulse on the diode signal can be observed. The powerful optical pump pulse of 20 μJ at 120 fs at a wavelength of 800 nm scatters from the hydrogen droplet onto the diodes. At this wavelength the responsivity of the diode is about 1.8 times higher than at the XUV wavelength [64]. Especially for longer delays (> 8 ps) of the XUV-probe pulse the decreased scattering signal from

the spectrometer cannot be reproduced by the DA. However, the steep increase of spectrometer intensity for zero pump-probe delay can also be traced in the diode signal. Therefore the diode may serve as a simple tool to determine the zero point of temporal overlap of pump and probe pulse. There is also a significant diode intensity for FEL-first shots (delay > 0 ps) which stems from the scattered FEL pulse.

In a second experiment the sole influence of the FEL on the DA intensities is observed. Therefore a series of intensity measurements is taken for fixed FEL and lH_2 conditions. Figure 5.3 (right) shows the respective diode signals vs. the mean voltage over all diodes for the same FEL pulse. When the FEL pulse hits the lH_2 droplet, photons are scattered in all directions towards the diodes. Fluctuation of the mean values can be caused by fluctuations of the FEL intensity and by different impact angles on the slightly fluctuating droplet trajectories. As can be seen in the right part of fig. 5.3, there is a clear linear correlation between the single diode voltage and mean voltage over all diodes. This linear correlation holds up for all 8 diodes.

In future experiments the DA can be used for further studies of the scattering process of XUV-FEL radiation at plasmas. Since it enables the measurement over a wide angular range, scattering experiments which extend over several XUV wavelengths are of interest. Rayleigh scattering exhibits different wavelength dependencies over the scattering angles for different target geometries. For Rayleigh scattering the scattered intensity follows a $I \sim \lambda^{-4}$ dependency for scattering off a sphere whereas a $I \sim \lambda^{-3}$ dependency for scattering of a tube or cylindrical object applies. Hence, the DA is a versatile tool to determine an unknown target geometry in experiments.

6. XUV Interferometry

6.1 An XUV Michelson Interferometer

The setup of a Michelson interferometer (MI) designed for 13.5 nm is described in this chapter. This is a wavelength commonly used for stable and efficient operation of the **F**ree-electron **LAS**er in **H**amburg (FLASH) and in extreme ultraviolet (EUV) lithography. The performance of the MI is tested at a synchrotron source, due to its specific requirements in this wavelengths range. Furthermore, the possibility to apply the MI at XUV FELs for potential investigation of excited solid density matter is investigated and in particular its dielectric properties. Data and results in this chapter have been basis for the publication *"An extreme ultraviolet Michelson interferometer for experiments at free-electron lasers"* in *Review of Scientific Instruments* [65].

6.1.1 Basic Interferometer Concept

The most crucial component of an interferometer is typically the beam splitter, which divides the beam so that both parts can propagate separately and lastly be overlapped on a detector. Note that mainly two different methods of beam splitting can be identified. *Wavefront division* geometrically splits the profile of the beam in two halves, while *amplitude division* induces a superposition of the entire beam profile [66]. To achieve wavefront division, total external reflection optics such as Fresnel bi-mirrors [67; 68] can be used in the XUV wavelength regime. The use of total external reflection optics also enables an operation over a wide

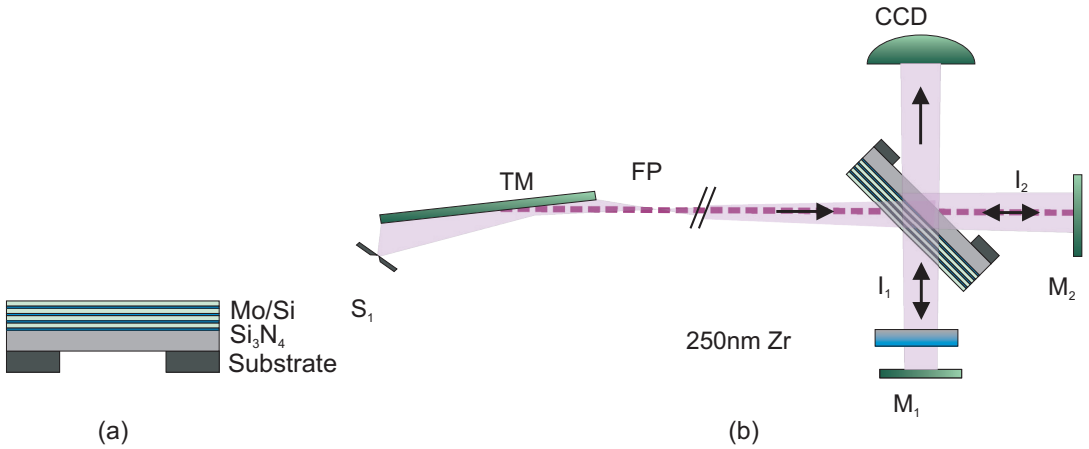

Figure 6.1: *(a)* Layer composition scheme of the beam splitter. Bilayer thickness: (9.890 ± 0.020) nm (Mo 3.46 nm, Si 6.43 nm) *(b)* The interferometer setup at the synchrotron source. S1 - monochromator exit slit, TM - toroidal mirror, FP - focal point, I_1 - intensity from arm with initial forward reflection, I_2 - intensity from arm with initial transmission and rear side reflection, M - multilayer mirrors - not to scale. [65]

spectral range. Alternatively, phase-shifting point diffraction [69] or zone plates [70] are suitable approaches. Wavefront division techniques require a certain spatial coherence for interference, since different parts of the beam profile are overlapped. Amplitude division interferometers instead, create two identical wavefront replica, which is a significant advantage compared to wavefront division techniques [71], since it enables a complete disentanglement of temporal and spatial coherence. To realize amplitude division separate diffraction orders of a grating [71] or thin-film beam splitters as in Mach-Zehnder [72] or Michelson [73] interferometers can be used. Separate adjustment of the respective arm lengths is in particular achieved by the compact Michelson scheme. So far XUV Fourier-transform spectroscopy [74; 75] measurements of the longitudinal coherence of x-ray lasers [76; 77] have been demonstrated based on this concept.

6.1.2 Interferometer Setup

The Beam Splitter

Several difficulties arise when designing an XUV interferometer. An XUV beam splitter in particular will exhibit comparatively low reflectivity and strong absorption in transmission. For this purpose a multilayer beam splitter is favorable and was used here. It consists of a silicon frame of 10 mm×10 mm. The center comprises a free standing membrane of silicon nitride (Si_3N_4) of 4 mm×4 mm. The thickness was measured via x-ray reflectometry by the manufacturer to be (142.0 ± 0.5) nm. In a next step a stack of 4 molybdenum-silicon (Mo/Si) bilayers are coated onto the membrane to achieve equal splitting of the beam at 45° incidence. A scheme of the beam splitter is shown in fig. 6.1a. Since the favorable incidence angle is also close to the Brewster angle for this wavelength, the reflection of p-polarized light is strongly suppressed. Thus operation of the beam splitter in s-polarization is inevitable at a linearly polarized FEL. I will refer to the multilayer side as the *front side* and to the membrane as the *rear side* in the following. Using tabulated values for reflection and absorption [48], the reflection in s-polarization can be calculated for 45° incidence and is depicted as a black line and a red asterisk in fig. 6.2. At 13.5 nm a front side reflectivity of 21.1 % and a rear side reflectivity of 1.1 % is found. Figure 6.2 shows also measurements carried out by the "Physikalisch Technische Bundesanstalt" in magenta and blue. Compared to the theoretical values, these measurements show a lower reflectivity of $R_{s-pol} = (16.7 \pm 0.3)\%$ at 13.5 nm. A transmission of $T_{s-pol} = (17.2 \pm 0.5)\%$, which is in the order of the reflection, is measured. In contrary to front side reflection, where light is impinging directly onto the multilayer stack, light that is reflected from the rear side passes the membrane twice. Therefore, absorption is accumulated over two paths through the membrane and rear side reflectivity is lower than front side reflectivity. Considering a MI the intensity from one of the arms would be much lower, due to this asymmetric reflection of the beam splitter. A reduced contrast of the interference fringes would be the result. To overcome this problem an additional absorbing foil of 250 nm Zr is

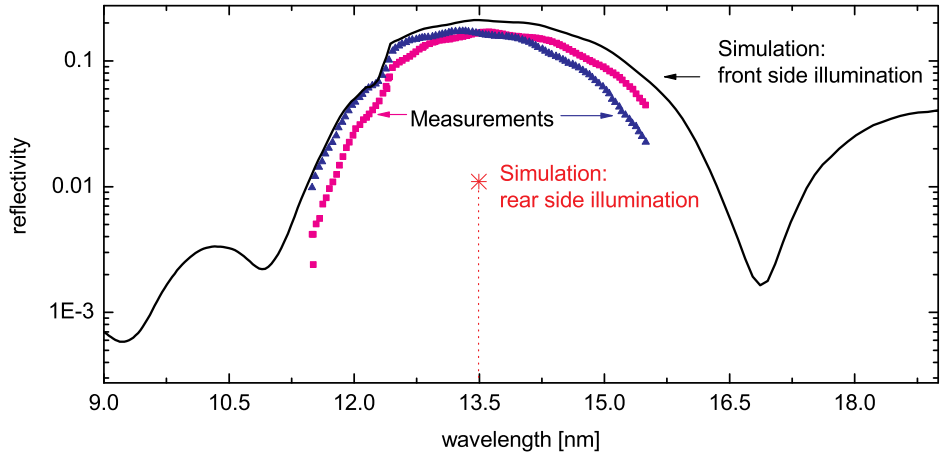

Figure 6.2: Blue and magenta data show reflectivity measurements for two beam splitters both with incoming light from the multilayer side (front side illumination). The spectral reflectivity varies due to deviations in the layer thickness. A calculated reflectivity curve for front side illumination is shown in black. Rear side reflectivity is calculated only for one point (red) at 13.5 nm. The absorption of the membrane causes a decrease by roughly one order of magnitude for the rear side reflection. [65]

inserted in the brighter arm. A scheme of this is shown in fig. 6.1b. Insertion of the foil yields an improved intensity ratio of $I_1/I_2 \approx 1.2$. From the well known thickness of the membrane and the Zr foil and the measured intensity of either interferometer arm, the density of the membrane can be estimated to $\varrho = (2.76 \pm 0.1)$ g/cm^3. Compared to tabulated values [48], this amounts to $(80 \pm 3)\%$ of the value for bulk material. Similar results have also been reported in [78].

Interferometer Components

To achieve high stability and sufficient alignment accuracy of a fraction of the wavelength, a few-nm precision positioning system with good thermal and vibrational stability is needed. In particular for this MI the optical components are attached to short posts which are fixed to the same solid base plate as shown in fig. 6.3. A combination of a translation piezo stage and a tip-tilt stage from *Piezosystem Jena* enables positioning of the variable arm at high precision. The travel range of the translation stage covers 400 μm and the angular tilting range of the tip-tilt stage covers ± 1 mrad. In fig. 6.3 M_1 and M_2 mark the position of the multilayer mirrors

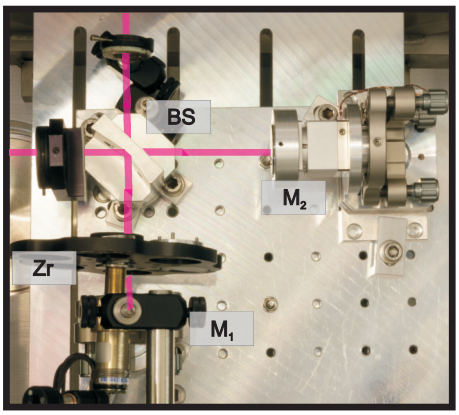

Figure 6.3: Setup of the interferometer. A filter revolver is placed in front of one mirror (M_1), which allows blocking of this path, to distinguish between both arms. Not shown in this photograph is the CCD detector on the top. [65]

at the end of the interferometer arms. Under perpendicular incidence the mirrors exhibit a reflectivity of $R > 65\%$ at a bandwith of (13.50 ± 0.05) nm. An Andor iKon CCD is used as a detector. Its sensitive area contains 2048×2048 pixels of 13.5×13.5 μm^2 size.

6.1.3 Experimental Proof of Principle

For a first proof of principle experiment the MI is set up at a the synchrotron source DORIS at DESY (Hamburg) [49]. Beamline BW3 is chosen for the experiment, because it comprises a plane grating monochromator and a variable exit slit. A wavelength of 13.5 nm ((92 ± 0.2) eV) is chosen. For this wavelength a photon flux of 10^{10} photons/s is estimated from the beamline parameters. Since the incoming radiation is s-polarized, a vertical orientation is chosen for the interferometer, where the detector is pointing upwards. As indicated in fig. 6.1b the interferometer is placed downstream of the beamline focus. The position of the beam splitter is approximately 60 cm behind the focus and thus it is illuminated entirely in vertical direction and 1.3 mm in horizontal direction. A typical interference pattern is shown in fig. 6.6.

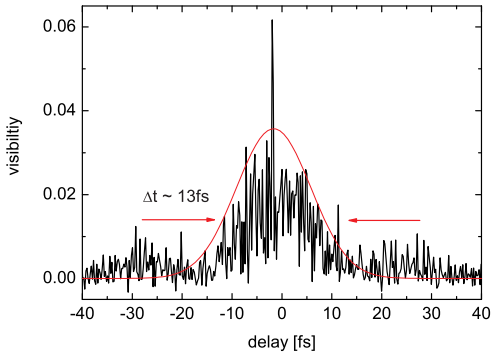

Figure 6.4: Measured visibility in dependence of delay time between the two interferometer arms. To guide the eye, the red line enclose values of maximum visibility. During the acquisition of an interferogram (17 ms), the position drift of the piezo actuated mirror in one arm causes a relatively low overall visibility. [65]

Temporal Coherence Measurement

A detailed analysis of the visibility within the interference pattern gives information about the temporal coherence of the radiation [30]. The visibility is therefore measured in dependence of the relative arm lengths of the interferometer. The visibility is measured as

$$V = \frac{I_{max} - I_{min}}{I_{max} + I_{min}} \,, \tag{6.1}$$

with the maximum and the minimum intensity I_{max} and I_{min} of the pattern.

A measurement of the temporal coherence is shown in fig. 6.4. Interferograms are recorded with the minimum acquisition time of the detector of 17 ms. Synchrotron radiation constantly impinges onto the detector during the acquisition and thereby a drift of the piezo-actuated mirror may also decrease the fringe contrast of the interferograms. In a potential application of the MI at an FEL this problem can be overcome by single shot mode, where the drift can be neglected for ultra short pulses. To increase the performance of the MI for cw-sources, the use of feedback stabilized actuators could prevent the drift of the mirror position. The red line in fig. 6.4 marks an envelope of the measured visibility. From this envelope a coherence time of 13 fs is determined. This amounts to 65% of the bandwidth-limited coherence time of 20 fs, which is expected from $\Delta E/E = 0.02$ % behind the beamline monochromator.

6.1.4 Membrane Surface Curvature

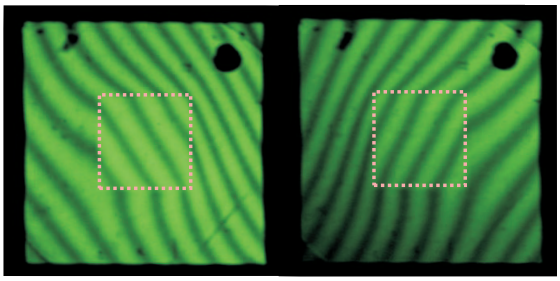

Figure 6.5: Interference comparator image to study the surface curvature of the beam splitter. The pattern results from interference between the beam splitter and an optical flat. It is observed at a wavelength of $\lambda = 541.6\,\text{nm}$. A pink square marks the position of the membrane. A flat interference pattern is observed across the multilayer area. The flatness can thus be estimated to be better than about $\lambda/4 \approx 150$ nm which is the detection limit in this case. [65]

To estimate the surface curvature of the beam splitter, the interference between the beam splitter and an optical flat is measured. Figure 6.5 shows no distinct curvature in the fringe pattern, which suggests an upper limit of $\approx 150\,\text{nm}$ for the flatness. An interference pattern at equal arm lengths is shown in fig. 6.6a. The tip-tilt station of one of the mirrors is adjusted to minimize the amount of fringes at maximum fringe contrast. Thus, the observed pattern stems from the surface curvature of the membrane. Interfering wavefronts in a MI are reflected on opposing sides of the beam splitter. Consequently, they are reflected at surfaces with inverted curvature signs. In a next step a simulation using the experimental parameters was performed in a ray tracing program. The observed fringe pattern can be adequately reproduced when assuming a quadratic function of the membrane surface curvature. The best matched simulated pattern is shown in fig. 6.6b. For such a pattern a 3D surface curvature as shown in fig. 6.6c is calculated. Figure 6.6c shows a maximum amplitude of the curvature of 150 nm (peak-to-valley). This is in agreement with the estimation from fig. 6.5 and also with the number of observed fringes.

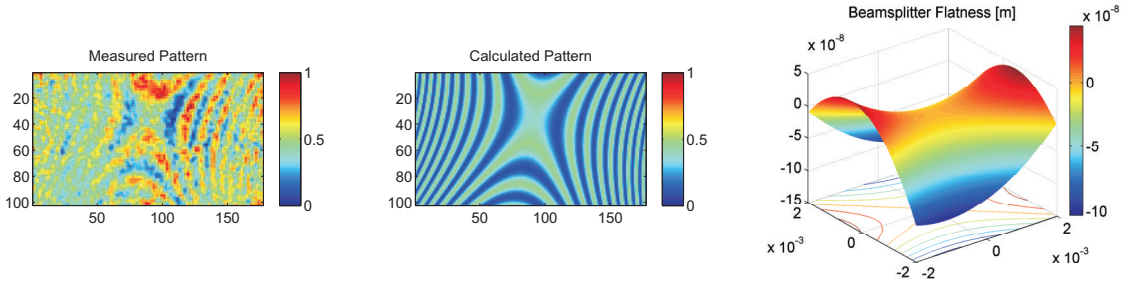

Figure 6.6: (a) Captured interference pattern at a size of of 2.4 mm×1.4 mm. To obtain an image that does not depend on a possible inhomogeneous illumination the captured signal is corrected by a reference (REF) taken at unequal arm lengths. REF is background (BGR) subtracted (T = 100 % × (Signal − BGR) / REF). A thus determined Transmittance T (in %) deviating from 100 % corresponds to decreased (blue) and increased (red) intensity due to interference. (b) Simulated fringe pattern, inferring a wave front curvature from the curved beam splitter. (c) Surface profile of the best matched beam splitter. [65]

6.1.5 Potential Applications at XUV FELs

Damage Threshold

In preparation for a possible application of the MI at a free electron laser, it has to be taken into account that high intensities of the FEL may locally ionize the solid material and generate a plasma [14; 42]. Permanent changes of the material properties should be excluded beforehand the experiment to avoid damage of the fragile beam splitter. For this purpose one-dimensional radiation hydrodynamics simulations are carried out using the HELIOS-CR code [79; 80]. Since the beam splitter is the first optical component struck by the FEL pulse it will be the object of inquiry for this simulation. Both the membrane and the overlaying Mo/Si stack are modeled. The starting temperature is set to an ambient value of 25 meV. The melting point for Si is at 1683 K (0.145 eV) and for Mo at 2896 K (0.25 eV), respectively. For lower ion temperatures the hydrodynamic motion is suppressed. For Si_3N_4 the sublimation point is at ≈ 2200 K. To simulate a typical scenario at a FEL, the parameters of irradiation are chosen as follows: 1 m behind the focus, a spot size 1.5 × 1.5 mm^2 is expected. Using typical pulse parameters such as 50 fs, 100 μJ, λ = 13.5 nm the

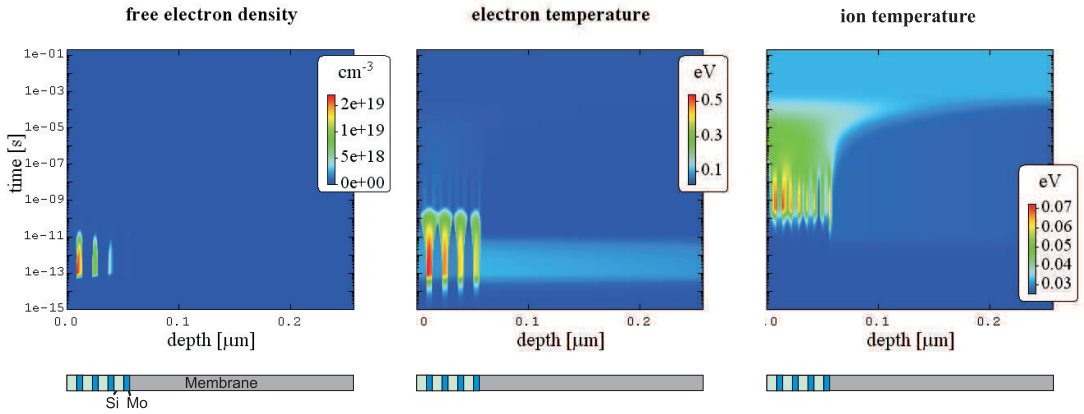

Figure 6.7: Hydrodynamic simulation with HELIOS-CR. In this setup a pulse impinges from the left onto the multilayer stack. The pulse duration is 50 fs, the wavelength 13.5 nm, pulse energy 100 μJ, intensity 0.1 TW/cm^2. The abscissa marks space and is linear scaled, whereas the ordinate marks the time and is scaled logarithmic. The free electron density n_e is shown on the left. n_e rises mostly on the surface during a few ten picoseconds. The center part shows the electron temperature T_e. T_e is increased over a few ten picoseconds. Afterwards the electrons thermalize with the ions, which is shown on the right, where the ion temperature is shown. It rises with a delay of a few ten to hundred picoseconds. [65]

beam splitter will be irradiated with an intensity of 0.1 TW/cm^2. Results of the simulation are shown in fig. 6.7. Space is marked on a linear scale on the abscissa, where the FEL impinges at the time of 100 fs from the left onto the Mo/Si stack. Time is marked on a logarithmic scale on the ordinate and reaches from 1 fs to 0.1 s, which is the time between two FEL pulses at the common FLASH repetition rate of 10 Hz. The left part of fig. 6.7 shows how the free-electron density n_e rises within the pulse duration mainly in the upper two Mo layers up to a few 10^{19} cm^{-3}. In the center part of the figure it is evident that during the same time the electron temperature T_e rises mainly in the upper Mo layers up to 0.5 eV. Meanwhile the Si layers and the Si_3N_4 membrane remain at electron temperatures around 0.1 eV, since they absorb less energy. The right part of fig. 6.7 shows that the energy transfer between ions and atoms is completed after a few tens of picoseconds. Approximately 1 ns after illumination, a maximum ion temperature of 70 meV is reached at the boundary of the upper Mo/Si transition, which corresponds to a temperature of less than 800 K and hence is below the melting temperature. 1 ms after irradiation the temperature

profile is smoothly distributed over the entire beam splitter and is almost cooled down to the initial temperature. It can be claimed that the energy introduced by a moderate-intense defocused FEL pulse is not sufficient to melt or even destroy the beam splitter. Considering back reflection by the mirrors in the MI arms which will be delayed by 100 ps due to the propagation distance of 2×15 mm along the MI arm, it can be concluded that at this time n_e has already decreased to the initial value (see fig. 6.7 (left)). Simulations infer a damage threshold of approximately $18\,\mathrm{mJ/cm^2}$, which corresponds to $0.35\,\mathrm{TW/cm^2}$ at a 350 mJ, 50 fs pulse. For conditions above the threshold, the melting point of Si is exceeded and the Mo/Si stack is likely to be destroyed. For illumination at $> (45 \pm 7)\,\mathrm{mJ/cm^2}$ and similar experimental conditions, deterioration of the multilayer was observed elsewhere [81]. Note that those simulations generally apply for the multilayer optics in the described interferometer and apart from that for any Mo/Si multilayer mirror applied at a similar FEL beam of any experiment. Due to the increased ion temperature during and after the FEL pulse, diffusion rates at the interfaces of the Si and Mo layers are increased. This may hamper the performance of any multilayer optical element, after extensive use in FEL experiments.

Pseudo-Nomarski XUV Interferometry

In the following a setup to use the MI as a pseudo-Nomarski interferometer is presented. If employed downstream of the target it can possibly be used in strongly-driven dense matter experiments to uncover phase changes. The method which is similar to visible light Nomarski interferometry [83] relies on sufficiently high spatial coherence of the incoming light. Optical Nomarski interferometry was used to observe plasma plumes expanding from laser irradiated solids with temporal resolution [82; 84]. Note that for the high laser frequencies ω of XUV radiation, the critical density $n_c = \omega^2 \epsilon_0 m / e^2$, with ϵ_0 the vacuum permittivity, and e the electron charge is much higher than for optical laser frequencies. This allows deeper penetration and study of solid-density matter with $n_c > 10^{24}\ \mathrm{cm^{-3}}$, whereas optical light is limited to densities of $n_c < 10^{21}\ \mathrm{cm^{-3}}$.

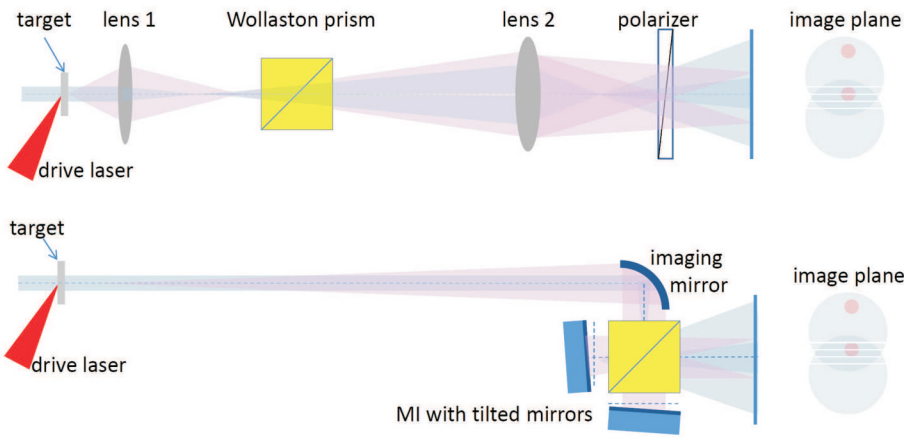

Figure 6.8: Two Nomarski-schemes to determine the free-electron density of a plasma. A standard scheme of optical Nomarski interferometry was proposed in Ref. [82] and is shown on the top. An XUV pseudo-Nomarski interferometry scheme is shown in comparison in the lower part. Laser beams are displayed in blue, while red lines represent optical imaging properties. [65]

The upper part of fig. 6.8 shows an interferometer of the Nomarksi-type. Shown in blue is the collimated laser pulse in the optical wavelength range, transmitted through a laser driven target. A configuration of lens 1 and lens 2 magnifies an image of the target plane onto a detector. In between both lenses a Wollaston prism separates both extra-ordinary and ordinary components and introduces an angular offset between them. The perpendicular polarized beams overlap on the detector since their angular offset is small. Interference of both beams can be achieved by the use of a polarizer. To adapt this setup for the XUV regime, the lenses 1 and 2 can be replaced by an imaging mirror. The lower part of fig. 6.8 shows a scheme of the XUV pseudo-Nomarski interferometer where the blue beam marks the unfocused FEL probe. Similar to the Wollaston prism, the MI is now used to separate the beam and overlap an undisturbed part of the profile with a distorted one. No polarizer is needed in the setup, since the beams are polarized identically. Phase shifts caused by the observed solid density matter will alter the fringe pattern in the image plane. Interference fringes are expected to be observed for wavefront separation $< 1\,\mathrm{mm}$, since the expected spatial coherence of FLASH is well above this value [32].

6.2 Coherence of the Free Electron Laser FLASH

The Michelson interferometer (MI) described in chapter 6.1 is now used to determine temporal and spatial coherence properties of an XUV free electron laser. Data and results in this chapter have been basis for the publication *"Spatio-temporal coherence of free-electron laser radiation in the extreme ultraviolet determined by a Michelson interferometer"* in *Applied Physics Letters* [85].

To measure the temporal coherence of a free electron laser the arm length of one interferometer arm is scanned, while at the same time interferograms are recorded. To determine the coherence length, the visibility of the fringes is analyzed as a function of time delay, i.e. arm length. A similar procedure is applied in the field of Fourier transform spectroscopy. Here, the autocorrelation function (AC) is measured and the spectrum of a light source is derived from the Fourier transformed signal. If the bandwidth of a given radiation source is very narrow, the corresponding AC or the fringe visibility will decay very slow, since they are Fourier pairs. Correspondingly, a high spectral resolution can be achieved if the slope of the AC is measured very accurately with the Fourier transform spectrometer. Measuring the temporal AC using a Michelson interferometer is thus of high importance for experiments making use of high precision XUV spectroscopy. These can involve FELs, high harmonic sources, and plasma line emissions.

A lateral shear between the interferometer arms needs to be introduced, to measure the spatial coherence of a free electron laser. Hence, at the detector two different points of the same wavefront are overlapped. Analyzing the fringe visibility and its successive decay for larger offset of the wavefronts, leads to the spatial coherence of the beam. Comparing the MI to previous interferometric techniques, there are some advantages of the MI over these techniques.

A so called *wavefront division* approach was used in past investigations of XUV free electron laser coherence. Therefore, the beam is split into two halfs, which are delayed in time with respect to each other. Lastly, both beams are overlapped on a detector [86]. This approach requires a certain spatial coherence of the analyzed

beam, since non identical parts of the beam profile are overlapped to create the fringe pattern. As a consequence for a full analysis of the temporal coherence, a relatively high spatial coherence is needed. Generally, a MI avoids this limitation, by applying transmissive optics. Hence, each of the MI arms contains the identical entire beam profile. The *amplitude divided* beam is recombined at the detector. Consequently, spatial and temporal coherence can be measured independently. Especially for beams with a low spatial coherence, the temporal coherence can still be determined.

6.2.1 Setup at the Free Electron Laser

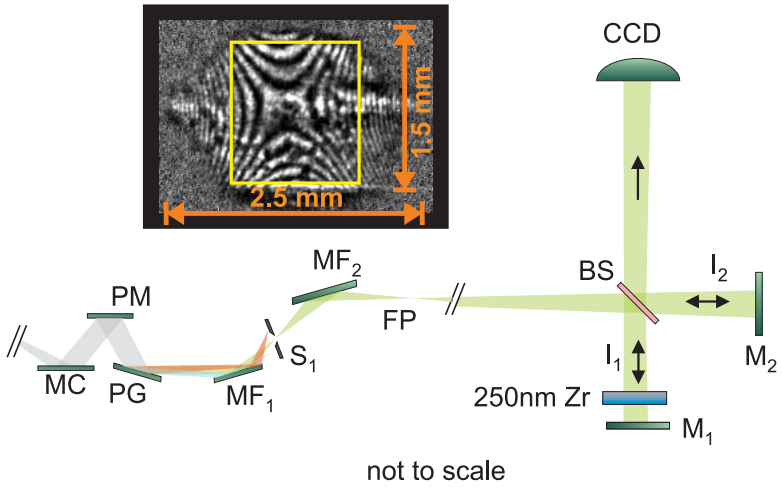

Figure 6.9: Setup of the MI at the beamline PG2 at the free electron laser. The monochromator comprises: MC - collimating mirror, PM - plane mirror, PG - plane grating, MF_1 - focusing mirror, S_1 - adjustable slit, MF_2 - focusing mirror. The MI consists of a beam splitter (BS) and multilayer mirrors (M_1, M_2) at the end of each interferometer arm. To compensate different intensities (I_1, I_2) in each arm, a 250 nm thick Zr foil is inserted in the brighter arm. The inset shows a typical interferogram with an x-shaped pattern. The pattern is formed by the aberrated wavefront of the FEL and by the curvature of the beam splitters membrane surface [65; 85; 73].

The coherence measurements are carried out at PG2 [87; 88; 89], the monochromator beamline at FLASH [6; 90]. A setup of the experiment is shown in fig. 6.9. PG2 comprises a collimating mirror, a plane mirror which is followed by a plane

grating and a focusing mirror. A variable slit in the end allows for precise adjustment of the bandwidth via the slit width [91]. The plane grating is operated in first order diffraction and has a line density of 200 l/mm. The variable slit is set to a width of 200 μm which corresponds to a spectral bandwidth of (92 ± 0.058) eV ($E/\Delta E \approx 1590$). Note that the reduced slit size also restricts the energy of the pulse to $\approx 1\,\mu$J. The exit slit is then imaged by the toroidal mirror to a focal spot of $\approx$ 200 μm $\times$ 50 μm spot size. The divergence amounts to (0.18 ± 0.02) mrad. The quality factor of the given beam can now be compared to a diffraction limited Gaussian beam. The resulting M^2 of ≈ 11 is comparably high and therefore a limited spatial coherence can be expected, which does not extend over the full beam profile.

The Michelson interferometer which is used to determine the coherence properties is described in detail in chapter 6.1. For the experiment the MI is placed ≈ 1.5 m downstream the focal plane. A profile of the beam at the detector is shown in the inset of fig. 6.9. At the detector the beam size amounts to 2.5 mm $\times$ 1.5 mm. The asymmetry of the two respective beam sizes is caused by influence of the monochromator exit on the wavefront and the beam shape. Prealignement of the MI at the beamline is done with an optical laser.

6.2.2 Static Piezos – Correlation VIS-STD

The free electron laser was set to a repetition rate of 10 Hz and a pulse length of about $100 - 150$ fs. In a first step interferograms of single exposures were recorded for 100 consecutive FEL pulses. Therefore, the MI arm lengths were set to equal lengths and best overlap. A typical interferogram for this zero delay setup is shown in the inset of fig. 6.9. Now the visibility of the fringe pattern can be calculated as:

$$V = \frac{\mathrm{I_{max}} - \mathrm{I_{min}}}{\mathrm{I_{max}} + \mathrm{I_{min}}} \,, \tag{6.2}$$

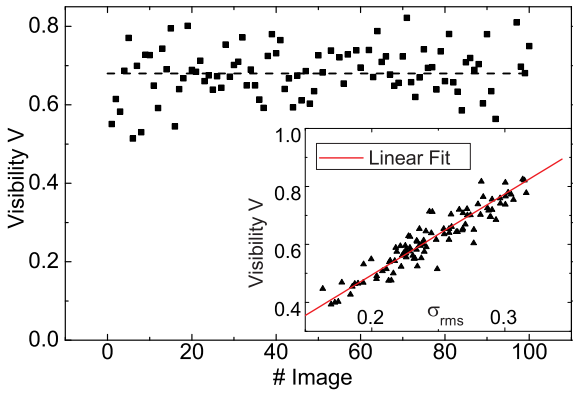

Figure 6.10: At equal interferometer arm lengths the visibility of the FEL is determined for 100 consecutive pulses. The mean visibility ($V_{mean} = (0.68 \pm 0.07)$) is indicated by the dashed black line. The correlation of standard deviation σ_{rms} and visibility of the analyzed area is shown in the inset. A linear fit with $\mathrm{V} = -(0.035 \pm 0.026) + \sigma_{rms}(2.80 \pm 0.10)$ of this correlation is shown as a red line in the inset. [85]

with $\mathrm{I_{max}}$ and $\mathrm{I_{min}}$ being the maximum and minimum intensity, respectively. The degree of coherence $\gamma_{12}(\tau, \vec{r})$ is directly related to the visibility via

$$V = |\gamma_{12}(\tau, \vec{r})| \, \frac{2\sqrt{I_1 I_2}}{(I_1 + I_2)} \ , \tag{6.3}$$

where I_1 and I_2 are the intensities in the respective arms, τ denotes the temporal separation, and $\vec{r}$ is the transverse spatial separation of the beams [66].

A series of 100 consecutive laser pulses was acquired for equal MI arm lengths, i.e. zero delay and their visibility is shown in fig. 6.10. For data analysis a region of interest (ROI) is defined and marked in yellow in fig. 6.9. As shown in fig. 6.10, there is a jitter of 10 % in visibility V, when analyzing a profile along the curved fringe pattern for consecutive measurements at fixed delay. In turn, a comparatively stable measure of the overall fringe contrast yields the evaluation of the standard deviation σ_{rms} within the designated ROI. The inset of fig. 6.10 shows the linear correlation between visibility V and standard deviation σ_{rms}. Henceforth, σ_{rms} will be used in this work to determine coherence properties from a curved fringe pattern. Thereby improved statistics minimize intensity fluctuations. Note that

using σ_{rms} instead of V still leaves some fluctuations which can be attributed to the stochastic nature of the SASE radiation [37]. Through the 58 meV bandpass of the monochromator, typically only a single spectral (longitudinal) mode is transmitted. Hence the statistical coherence of single modes is probed, which show an average visibility of 0.68 ± 0.07 with maximum values reaching 0.8.

6.2.3 Temporal and Spatial Coherence

Temporal coherence

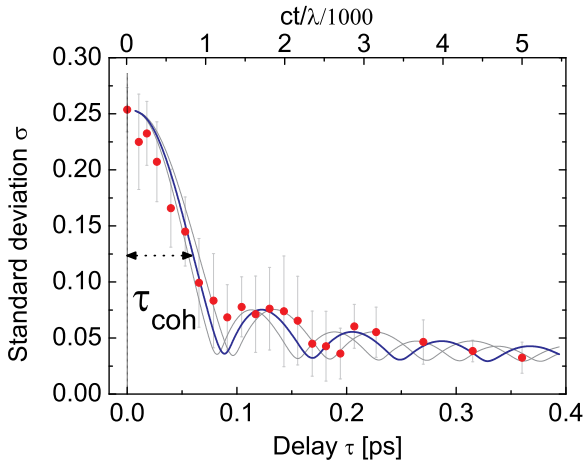

Figure 6.11: Temporal coherence measurement at PG2 at FLASH. Each data point of a standard deviation σ_{rms} represents an average over ten measurements. A *sinc*-fit for a spectral window of 55 meV of the measured data is added in blue. Spectral windows of (55 ± 5) meV and their corresponding *sinc*-fits are marked in grey. The curve width is measured to be (118 ± 18) fs, corresponding to a temporal coherence of $\tau_{coh} = (59 \pm 9)$ fs. [85]

To determine the temporal coherence, the variable arm of the MI is scanned, while single shot interferograms are recorded correspondingly. The optical path length is changed in steps of $0.54\,\mu$m (1.8 fs) and a total range of $814\,\mu$m (2713 fs) can be covered by the translation stage of the piezo. Results of this measurement are presented in fig. 6.11. The temporal autocorrelation corresponds to the Fourier transform of the spectral distribution of the FEL pulse. Consequently, the sinc-like structure

of the measured autocorrelation in 6.11 is transformed into a rectangular spectral distribution. Such a distribution can also be expected from the monochromator exit slit of the beamline. To achieve the best fit to the acquired data, a sinc-function with an rms half-width of $\tau_{coh} = 59\,\text{fs}$ is introduced. The corresponding coherence length $l_{coh} = \tau_{coh} \cdot c$ is then $l_{coh} = 17.7\,\mu\text{m}$ or about 1300 optical cycles. Note that an interference pattern encloses ≈ 26 fringes, which gives rise to a time lapse of $\tau_{lap} = 1.2$ fs along the image. Compared to the coherence length this is only $\tau_{lap}/\tau_{coh} \sim 0.02$ and the influence on the measurement is neglected. Furthermore, the periodicity of the sinc-function can be used to determine the bandwidth of the rectangular shaped spectrum of (55 ± 5) meV. This is in very good agreement with the spectral width of the radiation which should pass through the monochromator exit slit for the applied settings. The MI has thus been proven to be a suitable scanning Fourier transform spectrometer. The resolving power is $E/\Delta E = 92$ eV/10 meV ≈ 9000.

Spatial Coherence

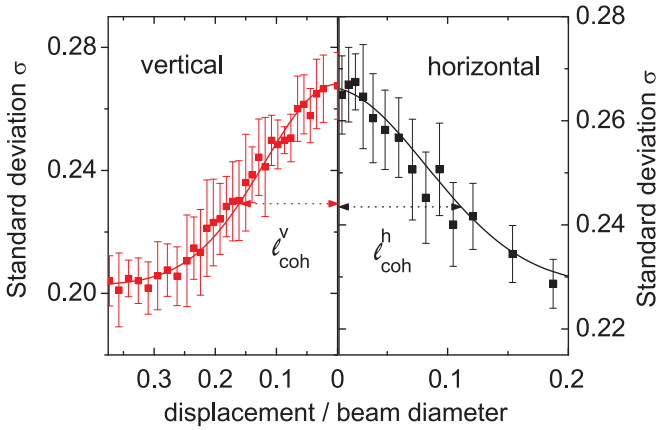

Figure 6.12: Spatial coherence measurement of the FEL pulses. Shown is σ_{rms} as a function of displacement relative to the beam size. The horizontal coherence is shown in black and the vertical coherence in red. Each data point represents an average over ten FEL pulses. Both measurements are fit to a Gaussian (solid lines). The arrows indicate the half width at half maximum. A coherence of $l^h_{coh} = (11.6 \pm 0.4)\%$ of the beam diameter is determined in horizontal direction and $l^v_{coh} = (14.9 \pm 0.5)\%$ in vertical direction. [85]

To measure the spatial coherence, the beam profiles are displaced in lateral di-

rection on the detector. This is achieved by tilting one of the mirrors of the MI, while both arms are kept at equal arm lengths. Using the minimum step size of the tip-tilt piezo a displacement of (1.86 ± 0.06) μm per step is achieved on the detector. The maximum displacement is 558 μm or 22 % of the beam diameter. Similar as described above, single shot interferograms are captured for different displacements and their respective standard deviation is determined as a measure of the visibility. Results are presented in fig. 6.12, where the standard deviation depending on the relative beam displacement is shown. Both curves are fitted with a Gaussian function and the respective transversal coherence is determined to be (290 ± 10) μm in the horizontal and (224 ± 8) μm in the vertical direction. This corresponds to (11.6 ± 0.4)% (horizontal) and (14.9 ± 0.5)% (vertical) of the beam diameter. An extra longitudinal shift is introduced by the lateral displacement of the profiles, which amounts to 1.6 μm at maximum. Compared to the longitudinal coherence this is a relatively small value and thus can be neglected for the determination of the spatial coherence. A wave front error is also introduced by the Zr foil in one of the interferometer arms. It is related to the figure error and extimated to be $< 4\,\mathrm{nm}$. Thereby a maximum phase shift of $\lambda/40$ (refractive index $n = 1 - 0.0408$) is introduced. Thus, the Zr foil is considered to have a negligible influence on the spatial coherence.

6.3 Summary of the Interferometry Chapter

The spatial and temporal coherence of XUV radiation from FELs is a unique and significant property, which can be measured via autocorrelation using a Michelson interferometer. The possibility to measure the coherence properties gives rise to improved machine operation of the FEL and thereby pushes experimental studies decisively.

In chapter 6.1 a Michelson interferometer setup which is optimized for a wavelength of 13.5 nm is described. A comprehensive test of this interferometer was carried out at a synchrotron source. Analysis of the fringe pattern yields a temporal coherence of 13 fs. Furthermore, the thin film beam splitters curvature is determined to be 150 nm in the peak-to-valley amplitude. 1D-hydrodynamics simulations were performed to estimate a possible damage of the multilayer optical components by intensive XUV radiation from FELs. Considering a typical irradiation flux of $0.1\,\mathrm{TW/cm^2}$, the obtained ion temperature does not reach the melting point. Further simulations infer a damage threshold of about $18\,\mathrm{mJ/cm^2}$. Excluding possible damage in a FEL experiment increases the potential use of the Michelson interferometer alongside solid density plasma experiments. A pseudo-Nomarski-interferometry setup is proposed. This technique could be applied at FELs to determine transient dielectric properties of opaque matter that is optically driven.

The Michelson interferometer was subsequently applied at the PG2 beamline of FLASH to determine the temporal and spatial coherence. This experiment is described in chapter 6.2. Using the monochromator of the beamline, the bandwidth was decreased to $\Delta E/E = 0.063\,\%$, corresponding to a coherence time of τ_{coh} =70 fs. A coherence time of $\tau_{coh} = (59 \pm 9)\,\mathrm{fs}$ was measured in the experiment, which is in good agreement to the expected value from the bandwidth given by the monochromator. A Fourier transformation of the autocorrelation reveals a spectral resolution of approximately 9000 in Fourier-transform spectroscopy.

A spatial coherence of $l_{coh} \approx 15\,\%$ in vertical and $l_{coh} \approx 12\,\%$ in horizontal direction was measured. These values agree with previously reported values. According

to theoretical considerations, the spatial coherence depends on the electron bunch currents of the FEL. During this experiment, bunch currents exceeding 2 kA were present to achieve high pulse energies. Hence, the spatial coherence is decreased with respect to its potential maximum [92]. This can be explained by a short gain length of the fundamental transverse mode TEM_{00} compared to the undulator length. Consequently, competing higher order modes are growing within the undulator and thereby reduce the spatial coherence.

7. Conclusion and Outlook

This thesis presents design, characterization and various applications of unique, innovative XUV sensitive diagnostics. Initially the specific demands towards optical components in this wavelength range are framed and their applicability and performance is tested in experiments or simulations. Subsequently the diagnostic tools are designed, built, calibrated and finally applied at both FELs and optical laser plasma experiments, where they provide valuable insight into liquid up to solid density plasmas.

In order to investigate solid-density plasmas, in a first step an XUV sensitive spectrometer was built and its optical components were characterized extensively. To optimize the positions of the optical components, ray tracing simulations were carried out to predict spectral resolution and performance. In a proof of principle experiment, XUV emission from a laser generated Al plasma was analyzed under different angles simultaneously. Relative intensities of characteristic spectral lines were compared to hydrodynamic simulations. Thus different temperature zones and their respective expansion of a few 10 μm to a few 100 μm could be identified. Continuing these spectrometer studies, a method for the simultaneous cross calibration of three different XUV sensitive spectrometers is presented. The interaction point, which is in this case a laser generated plasma, is observed by the spectrometers under different viewing angles. The presented method of in-situ simultaneous determination of dispersion can be transferred to any laser plasma experiment offering moderate laser intensities.

In earlier experiments on dense hydrogen plasma, the free-electron temperature could only be simulated by hydrodynamic codes, since experimental temperature

measurements belong to the most challenging tasks. In this work the temperature of a laser generated plasma is determined experimentally via time-integrated bremsstrahlung spectroscopy of a plasma in self emission. To achieve this, dense cryogenic hydrogen is heated by ultrashort intense infrared laser pulses. XUV bremsstrahlung is spectrally resolved and compared to predictions from simulations. Since the method is most sensitive to sections with a high free electron density, it is strongly weighted towards time scales shorter than hydrodynamic expansion. In future experiments this technique may be used complementary to well established x-ray absorption near edge spectroscopy or collective x-ray scattering techniques.

In contrast to heating via optical laser radiation, which creates a critical free electron density at the droplet surface and thus limits the penetration depth to a few 10 nm, isochoric heating can be achieved via XUV laser pulses. Such an experiment was conducted at the FLASH FEL in Hamburg. Ultrashort XUV pulses isochorically heated a cryogenic hydrogen target on timescales which are shorter than the hydrodynamic expansion. Consequently, the properties of the transient plasma can be probed by a delayed second XUV pulse, and a time resolved observation of the ultrafast phase transition becomes possible. The investigation of the change from molecular liquid hydrogen to a dense free-electron plasma sheds light on transport properties of dense plasmas, such as electron heating, plasma conductivity, and equilibration dynamics. From this perspective, the experiment provides a valuable contribution to the validation of different ionization models.

Moreover, a diode array consisting of eight XUV sensitive diodes, which are arranged on a semicircle at an angular pitch of 18.1° is presented. The applicability of the diode array is proven in an optical-pump-FEL-probe experiment. Since it enables the measurement over a wide angular range the diode array can be applied in future experiments to further study the scattering process of FEL radiation at plasmas.

This work also covers the development of an XUV Michelson interferometer (MI) which is specifically designed for plasma physics experiments at XUV FELs. A comprehensive test was carried out at a 13.5 nm synchrotron source. A temporal coherence of 13 fs was determined from the fringe visibility. Furthermore, the fringe

pattern was analyzed and yielded a beam splitter membrane curvature of 150 nm in peak-to-valley only. To explore the possible application of the MI at FELs, 1D-hydrodynamics simulations with typical values of FEL pulse energies were carried out. Thus, possible damage can be excluded due to an expected ion temperature below the melting point. A damage threshold of $\approx 18\,\mathrm{mJ/cm^2}$ was determined. Eventually, the possible application of the MI in plasma investigations is highlighted. A setup for pseudo-Nomarski-interferometry at XUV FELs is proposed. Development if this technique in the XUV wavelength range opens new perspectives for the determination of transient dielectric properties of strongly driven optically opaque matter.

In a next step the XUV-MI is used to perform an experiment at the FLASH facility at DESY, Hamburg. The issue of spatial and temporal coherence properties of the FEL is addressed in this experiment. Spectral properties can be controlled by the experimenter, via instrumental adjustments of the monochromator beamline PG2. A prediction of the temporal coherence properties is possible from the well known spectral distribution of the FEL pulse and can thus be compared to the measurements. Intensity fluctuations and noise in the recorded interferograms pose a challenge in the interpretation of the data. Therefore, in this work data analysis is carried out via evaluation of the standard deviation instead of the visibility, which gives rise to improved statistics. The measured spatial coherence lies well within the range of reported values and can be explained via recently published theoretical conclusions. In this framework this work represents an important contribution to the understanding of the self-amplified spontaneous emission (SASE) nature of FEL radiation and its impact on the spatio-temporal coherence properties.

With respect to future experiments, the high spectral resolution of 9000 of the MI in Fourier transformation spectroscopy could be further exploited. High precision spectroscopy of high harmonics in gases or at plasma mirrors could be fields of research. Those harmonics reveal a substructure in the spectrum, which contains information about the generation process and the underlying ultrafast electron dynamics. Fourier transform spectroscopy could promote high precision measurements of the spectral substructure of high harmonic radiation.

Bibliography

[1] B. A. Remington, R. M. Cavallo, M. J. Edwards, D. D.-M. Ho, B. F. Lasinski, K. T. Lorenz, H. E. Lorenzana, J. M. Mcnaney, S. M. Pollaine, and R. F. Smith. Accessing high pressure states relevant to core conditions in the giant planets. *Astrophysics and Space Science*, 298(1):235–240, 2005.

[2] R. P. Drake. Perspectives on high-energy-density physicsa. *Physics of Plasmas*, 16(5):055501, 2009.

[3] J. M. M. McMahon, M. A. Morales, C. Pierleoni, and D. M. Ceperley. The properties of hydrogen and helium under extreme conditions. *Reviews of Modern Physics*, 84:1607–1653, 2012.

[4] I. Baraffe, G. Chabrier, and T. Barman. The physical properties of extra-solar planets. *Reports on Progress in Physics*, 73(1):016901, 2010.

[5] R. J. Hemley. Percy W. Bridgman's second century. *High Pressure Research*, 30(4):581–619, 2010.

[6] W. Ackermann, G. Asova, V. Ayvazyan, A. Azima, N. Baboi, J. Bähr, V. Balandin, B. Beutner, A. Brandt, A. Bolzmann, et al. Operation of a free-electron laser from the extreme ultraviolet to the water window. *Nature photonics*, 1(6):336–342, 2007.

[7] E. Allaria, C. Callegari, D. Cocco, W.M. Fawley, M. Kiskinova, C. Masciovecchio, and F. Parmigiani. The fermi@ elettra free-electron-laser source for coher-

ent x-ray physics: photon properties, beam transport system and applications. *New Journal of Physics*, 12(7):075002, 2010.

[8] R. R. Fäustlin, U. Zastrau, S. Toleikis, I. Uschmann, E. Förster, and Th. Tschentscher. A compact soft x-ray spectrograph combining high efficiency and resolution. *Journal of Instrumentation*, 5(02):P02004, 2010.

[9] R. Mitzner, A.A. Sorokin, B. Siemer, S. Roling, M. Rutkowski, H. Zacharias, M. Neeb, T. Noll, F. Siewert, W. Eberhardt, et al. Direct autocorrelation of soft-x-ray free-electron-laser pulses by time-resolved two-photon double ionization of he. *Physical Review A*, 80(2):025402, 2009.

[10] S. H. Glenzer, O. L. Landen, P Neumayer, R. W. Lee, K. Widmann, S. W. Pollaine, R. J. Wallace, G. Gregori, A. Höll, T. Bornath, and other.s. Observations of plasmons in warm dense matter. *Physical Review Letters*, 98:065002–065005, 2007.

[11] G. Gregori, S. H. Glenzer, K. B. Fournier, K. M. Campbell, E. L. Dewald, O. S. Jones, J. H. Hammer, S.B. Hansen, R. J. Wallace, and O. L. Landen. X-ray measurements of radiative heating and cooling dynamics. *Physical Review Letters*, 101:045003–045006, 2008.

[12] A. Kritcher, P Neumayer, J. Castor, T. Döppner, R.W. Falcone, O. Landen, H.J. Lee, R.W. Lee, E.C. Morse, A. Ng, S. Pollaine, D. Price, and S.H. Glenzer. Ultrafast x-ray thomson scattering of shock-compressed matter. *Science*, 322:69–71, 2008.

[13] S. H. Glenzer and R. Redmer. X-ray thomson scattering in high energy density plasmas. *Reviews of Modern Physics*, 81(4):1625–1663, 2009.

[14] B. Nagler, U. Zastrau, R.R. Fäustlin, S. Vinko, T. Whitcher, A.J. Nelson, R. Sobierajski, J. Krzywinski, J. Chalupsky, E. Abreu, et al. Turning solid aluminum transparent by intense soft x-ray photoionization. *Nature Physics*, 5:693–696, 2009.

[15] S. M. Vinko, O. Ciricosta, B. I. Cho, K. Engelhorn, H. K. Chung, C. R. D. Brown, T. Burian, J. Chalupskỳ, R. W. Falcone, C. Graves, et al. Creation and diagnosis of a solid-density plasma with an x-ray free-electron laser. *Nature*, 482(7383):59–62, 2012.

[16] F. Dorchies, A. Lévy, C. Goyon, P. Combis, D. Descamps, C. Fourment, M. Harmand, S. Hulin, P. M. Leguay, S. Petit, et al. Unraveling the solid-liquid-vapor phase transition dynamics at the atomic level with ultrafast x-ray absorption near-edge spectroscopy. *Physical Review Letters*, 107(24):245006, 2011.

[17] Z. Lin, L. V. Zhigilei, and Vittorio C. Electron-phonon coupling and electron heat capacity of metals under conditions of strong electron-phonon nonequilibrium. *Physical Review B*, 77(7):075133, 2008.

[18] N. Nettelmann, B. Holst, A. Kietzmann, M. French, R. Redmer, and D. Blaschke. Ab initio equation of state data for hydrogen, helium, and water and the internal structure of Jupiter. *The Astrophysical Journal*, 683:1217 – 1228, 2008.

[19] J. D. Lindl, P. Amendt, R. L. Berger, S. Glendinning, S. H. Glenzer, S. W. Haan, R. L. Kauffman, O. L. Landen, and L. J. Suter. The physics basis for ignition using indirect-drive targets in the National Ignition Facility. *Physics of Plasmas*, 11:339–491, 2004.

[20] J. Leconte and G. Chabrier. A new vision of giant planet interiors: Impact of double diffusive convection. *Astronomy and Astrophysics*, 540:A20, 2012.

[21] A. J. Mackinnon, J. L. Kline, S. N. Dixit, S. H. Glenzer, M. J. Edwards, D. A. Callahan, N. B. Meezan, S. W. Haan, J. D. Kilkenny, T. Döppner, et al. Assembly of high-areal-density deuterium-tritium fuel from indirectly driven cryogenic implosions. *Physical Review Letters*, 108:215005, May 2012.

[22] S. H. Glenzer, D. A. Callahan, A. J. MacKinnon, J. L. Kline, G. Grim, E. T. Alger, R. L. Berger, L. A. Bernstein, R. Betti, D. L. Bleuel, et al. Cryogenic

thermonuclear fuel implosions on the national ignition facility. *Physics of Plasmas*, 19:056318–056332, 2012.

[23] C. Wagner and N. Harned. EUV lithography: Lithography gets extreme. *Nature Photonics*, 4:24–26, 2010.

[24] P. Gibbon. *Short Pulse Laser Interactions with Matter: An Introduction*. World Scientific Publishing Company, 2005.

[25] P. Mulser and D. Bauer. *High Power Laser - Matter Interaction*. Springer, 2010.

[26] R. R. Fäustlin, Th. Bornath, T. Döppner, S. Düsterer, E. Förster, C. Fortmann, S. H. Glenzer, S. Göde, G. Gregori, R. Irsig, et al. Observation of ultrafast nonequilibrium collective dynamics in warm dense hydrogen. *Physical Review Letters*, 104(12):125002, 2010.

[27] P. Sperling, U. Zastrau, S. Toleikis, S. H. Glenzer, and R. Redmer. X-ray thomson scattering diagnostics of impact ionization in laser-driven carbon foils. *Journal of Physics B: Atomic, Molecular and Optical Physics*, 48(12):125701, 2015.

[28] Th. Bornath, P. Hilse, and M. Schlanges. Ionization dynamics in nanometer-sized clusters interacting with intense laser fields. *Laser Physics*, 17(5):591–603, 2007.

[29] T. Fennel, L. Ramunno, and T. Brabec. Highly charged ions from laser-cluster interactions: Local-field-enhanced impact ionization and frustrated electron-ion recombination. *Physical Review Letters*, 99:233401, 2007.

[30] W.F. Schlotter, F. Sorgenfrei, T. Beeck, M. Beye, S. Gieschen, H. Meyer, M. Nagasono, A. Föhlisch, and W. Wurth. Longitudinal coherence measurements of an extreme-ultraviolet free-electron laser. *Optics Letters*, 35(3):372–374, 2010.

[31] A. Singer, I.A. Vartanyants, M. Kuhlmann, S. Duesterer, R. Treusch, and J. Feldhaus. Transverse-coherence properties of the free-electron-laser flash at desy. *Physical Review Letters*, 101(25):254801, 2008.

[32] S. Roling, B. Siemer, M. Wöstmann, H. Zacharias, R. Mitzner, A. Singer, K. Tiedtke, and I.A. Vartanyants. Temporal and spatial coherence properties of free-electron-laser pulses in the extreme ultraviolet regime. *Physical Review Special Topics-Accelerators and Beams*, 14(8):080701, 2011.

[33] P. Zeitoun, M. Fajardo, and G. Lambert. X-ray lasers: Coherent and compact. *Nature Photonics*, 4(11):739–740, 2010.

[34] L.B. Da Silva, T.W. Barbee Jr., R. Cauble, P. Celliers, J. Harder, H.R. Lee, R.A. London, D.L. Matthews, S. Mrowka, J.C. Moreno, et al. X-ray lasers for high density plasma diagnostics. *Review of Scientific Instruments*, 66(1):574–578, 1995.

[35] I. Robinson, G. Gruebel, and S. Mochrie. Focus on x-ray beams with high coherence. *New Journal of Physics*, 12(3):035002, 2010.

[36] L.B. Da Silva, T.W. Barbee, R. Cauble, P. Celliers, D. Ciarlo, J.C. Moreno, S. Mrowka, J.E. Trebes, A.S. Wan, and F. Weber. Extreme-ultraviolet interferometry at 15.5 nm using multilayer optics. *Applied Optics*, 34(28):6389–6392, 1995.

[37] E. L. Saldin, E. A. Schneidmiller, and M. V. Yurkov. *The Physics of Free Electron Lasers*. Springer-Verlag, Berlin Heidelberg, 2000.

[38] E. Allaria, R. Appio, L. Badano, W.A. Barletta, S. Bassanese, S.G. Biedron, A. Borga, E. Busetto, D. Castronovo, Cinquegrana, et al. Highly coherent and stable pulses from the fermi seeded free-electron laser in the extreme ultraviolet. *Nature Photonics*, 6(10):699–704, 2012.

[39] David Attwood. *Soft x-rays and extreme ultraviolet radiation: principles and applications*. Cambridge university press, 1999.

[40] P. Schmüser, M. Dohlus, J. Rossbach, and C. Behrens. *X-Ray Free-Electron Lasers: Technical Realization and Experimental Results*. Springer, 2014.

[41] A. Egbert and S. Becker. *Manual of the Microfocus EUV Tube*. Phoenix EUV Systems, Wunstorf, Germany, 2008.

[42] U. Zastrau, C. Fortmann, R.R. Fäustlin, L.F. Cao, T. Döppner, S. Düsterer, S.H. Glenzer, G. Gregori, T. Laarmann, H.J. Lee, et al. Bremsstrahlung and line spectroscopy of warm dense aluminum plasma heated by xuv free-electron-laser radiation. *Physical Review E*, 78(6):066406, 2008.

[43] A. L'Huillier and Ph. Balcou. High-order harmonic generation in rare gases with a 1-ps 1053-nm laser. *Physical Review Letters*, 70:774–777, 1993.

[44] U. Zastrau, P. Sperling, M. Harmand, A. Becker, T. Bornath, R. Bredow, S. Dziarzhytski, T. Fennel, B. Fletcher, L. V. Hilbert, et al. Resolving ultrafast heating of dense cryogenic hydrogen. *Physical Review Letters*, 112:105002, 2014.

[45] R. R. Fäustlin, Th. Bornath, T. Döppner, S. Düsterer, E. Förster, C. Fortmann, S. H. Glenzer, S. Göde, G. Gregori, R. Irsig, et al. Observation of ultrafast nonequilibrium collective dynamics in warm dense hydrogen. *Physical Review Letters*, 104:125002, 2010.

[46] R. Thiele, P. Sperling, M. Chen, Th. Bornath, R.R. Fäustlin, C. Fortmann, S.H. Glenzer, W.-D. Kraeft, A. Pukhov, S. Toleikis, et al. Thomson scattering on inhomogeneous targets. *Physical Review E*, 82(5):056404, 2010.

[47] T. Kita, T. Harada, N. Nakano, and H. Kuoda. Mechanically ruled aberration-corrected concave gratings for a flat-field grazing-incidence spectrograph. *Applied Optics*, 22:512–513, 1983.

[48] The center for x-ray optics http://henke.lbl.gov, February 2012.

[49] O. Björneholm, F. Federmann, C. Larsson, U. Hahn, A. Rieck, S. Kakar, T. Möller, A. Beutler, and F. Fössing. Performance of the extreme ultraviolet high resolution undulator beamline bw3 at hasylab: First results and

time-of-flight spectroscopy. *Review of Scientific Instruments*, 66(2):1732–1734, 1995.

[50] J. Edelstein, M.C. Hettrick, S. Mrowka, P. Jelinsky, and C. Martin. Extreme uv measurements of a varied line-space hitachi reflection grating: efficiency and scattering. *Applied Optics*, 23(19):3267–3270, 1984.

[51] Y. Ralchenko et al. Nist atomic spectra database, 2011.

[52] H.-K. Chung, M.H. Chen, W.L. Morgan, Y. Ralchenko, and R.W. Lee. Flychk: Generalized population kinetics and spectral model for rapid spectroscopic analysis for all elements. *High Energy Density Physics*, 1(1):3 – 12, 2005.

[53] U. Zastrau, Hilbert V., C. Brown, T. Döppner, S. Dziarzhytski, E. Förster, S. H. Glenzer, S. Göde, G. Gregori, M. Harmand, et al. In-situ determination of dispersion and resolving power in simultaneous multiple-angle xuv spectroscopy. *Journal of Instrumentation*, 6(10):P10001, 2011.

[54] S. Toleikis, R.R. Fäustlin, L. Cao, T. Döppner, S. Düsterer, E. Förster, C. Fortmann, S.H. Glenzer, S. Göde, G. Gregori, et al. Soft x-ray scattering using fel radiation for probing near-solid density plasmas at few electron volt temperatures. *High Energy Density Physics*, 6(1):15–20, 2010.

[55] N. Nakano, H. Kuroda, T. Kita, and T. Harada. Development of a flat-field grazing-incidence xuv spectrometer and its application in picosecond xuv spectroscopy. *Applied Optics*, 23:2386–2392, 1984.

[56] U. Teubner, G. Kuehnle, and F. P. Schaefer. Detailed study of the effect of a short prepulse on soft X-ray spectra generated by a high-intensity KrF(*) laser pulse. *Applied Physics B Photophysics Laser Chemistry*, 54:493–499, 1992.

[57] H. Redlin, A. Al-Shemmary, A. Azima, N. Stojanovic, F. Tavella, I. Will, and S. Düsterer. The flash pump-probe laser system: Setup, characterization and optical beamlines. *Nuclear Instruments and Methods in Physics Research*

Section A: Accelerators, Spectrometers, Detectors and Associated Equipment, 635(1, Supplement):S88 – S93, 2011.

[58] Zemax: Software for optical system design.

[59] U. Zastrau, P. Sperling, C. Fortmann-Grote, A. Becker, T. Bornath, R. Bredow, T. Döppner, T. Fennel, L. B. Fletcher, and V. others Hilbert. Ultrafast electron kinetics in short pulse laser-driven dense hydrogen. *Journal of Physics B: Atomic, Molecular and Optical Physics*, 48(22):224004, 2015.

[60] Lord Rayleigh. On the capillary phenomena of jets. In *Proceedings of the Royal Society of London*, volume 29, pages 71–97, 1879.

[61] H. A. Kramers. On the theory of x-ray absorption and the continuous x-ray spectrum. *Philosophical Magazine*, 46:836, 1923.

[62] U. Zastrau, P. Sperling, A. Becker, T. Bornath, R. Bredow, T. Döppner, S. Dziarzhytski, T. Fennel, L. B. Fletcher, V. Hilbert, et al. Equilibration dynamics and conductivity of warm dense hydrogen. *Physical Review E*, 90:013104, 2014.

[63] M. Wöstmann, R. Mitzner, T. Noll, S. Roling, B. Siemer, F. Siewert, S. Eppenhoff, F. Wahlert, and H. Zacharias. The xuv split-and-delay unit at beamline bl2 at flash. *Journal of Physics B: Atomic, Molecular and Optical Physics*, 46(16):164005, 2013.

[64] 2004. Datasheet of the XUV diode, IRD inc.

[65] V. Hilbert, A. Blinne, S. Fuchs, T. Feigl, T. Kämpfer, C. Rödel, I. Uschmann, M. Wünsche, G.G. Paulus, E. Förster, and U. Zastrau. An extreme ultraviolet michelson interferometer for experiments at free-electron lasers. *Review of Scientific Instruments*, 84(9):095111, 2013.

[66] B. Born and E. Wolf. *Priciples of Optics*. Cambridge University Press, 1999.

[67] F. Albert, D. Joyeux, P. Jaegle, A. Carillon, J.P. Chauvineau, G. Jamelot, A. Klisnick, J.C. Lagron, D. Phalippou, D. Ros, et al. Interferograms obtained with a x-ray laser by means of a wavefront division interferometer. *Optics Communications*, 142:184–188, 1997.

[68] J. Svatos, F. Polack, D. Joyeux, and D. Phalippou. Soft-x-ray interferometer for measuring the refractive index of materials. *Optics Letters*, 18:1367–1369, 1993.

[69] H. Medecki, E. Tejnil, K.A. Goldberg, and J. Bokor. Phase-shifting point diffraction interferometer. *Optics Letters*, 21(19):1526–1528, 1996.

[70] M. Wieland, T. Wilhein, Ch. Spielmann, and U. Kleineberg. Zone-plate interferometry at 13 nm wavelength. *Applied Physics B*, 76(8):885–889, 2003.

[71] J. Filevich, K. Kanizay, M.C. Marconi, J.L.A. Chilla, and J. Rocca. Dense plasma diagnostics with an amplitude-division soft-x-ray laser interferometer based on diffraction gratings. *Optics Letters*, 25(5):356–358, 2000.

[72] P. Celliers, F. Weber, L.B. Da Silva, T.W. Barbee, R. Cauble, A.S. Wan, and J.C. Moreno. Fringe formation and coherence of a soft-x-ray laser beam illuminating a mach-zehnder interferometer. *Optics Letters*, 20:1907–1909, 1995.

[73] A. Morlens, P. Zeitoun, L. Vanbostal, P. Mercere, G. Faivre, S. Hubert, P. Troussel, C. Remond, R. Marmoret, F. Delmotte, et al. Study of xuv beam splitter flatness for use on a michelson interferometer. *Laser and Particle Beams*, 22(03):279–284, 2004.

[74] Ph. Zeitoun, Ph. Balcou, S. Bucourt, F. Delmotte, G. Dovillaire, D. Douillet, J. Dunn, G. Faivre, M. Fajardo, K.A. Goldberg, et al. Recent developments in XUV optics and XUV diagnostics. *Applied Physics B*, 78:983–988, 2004.

[75] P. Zeitoun, P. Balcou, S. Bucourt, D. Benredjem, F. Delmotte, G. Dovillaire, D. Douillet, J. Dunn, G. Faivre, M. Fajardo, et al. New techniques for the

measurement of x-ray beam or x-ray optics quality. *Proc. SPIE, Soft X-Ray Lasers and Applications V*, 5197:194–204, 2003.

[76] R.F. Smith, J. Dunn, J. Hunter, J. Nilsen, S. Hubert, S. Jacquemot, C. Remond, R. Marmoret, M. Fajardo, P. Zeitoun, et al. Longitudinal coherence measurements of a transient collisional x-ray laser. *Optics Letters*, 28(22):2261–2263, 2003.

[77] J. Dunn, R. F. Smith, S. Hubert, M. Fajardo, P. Zeitoun, J. R. Hunter, C. Remond, L. Vanbostal, S. Jacquemot, J. Nilsen, et al. Coherence measurements of a transient 14.7-nm x-ray laser. *Proc. SPIE, Soft X-Ray Lasers and Applications V*, 5197:43–50, 2003.

[78] F. Delmotte, M. F. Ravet, F. Bridou, F. Varniere, P. Zeitoun, S. Hubert, L. Vanbostal, and G. Soullie. X-ray–ultraviolet beam splitters for the michelson interferometer. *Applied Optics*, 41(28):5905–5912, 2002.

[79] J. J. MacFarlane, I. E. Golovkin, and P. R. Woodruff. Helios-cr–a 1-d radiation-magnetohydrodynamics code with inline atomic kinetics modeling. *Journal of Quantitative Spectroscopy and Radiative Transfer*, 99(1):381–397, 2006.

[80] J. D. Johnson and S. Lyon. Sesame 2984. *SESAME 2984, Los Alamos National Laboratory*, 1997.

[81] A.R. Khorsand, R. Sobierajski, E. Louis, S. Bruijn, E.D. Van Hattum, R.W.E. Van De Kruijs, M. Jurek, D. Klinger, J.B. Pelka, L. Juha, et al. Single shot damage mechanism of mo/si multilayer optics under intense pulsed xuv-exposure. *Optics Express*, 18(2):700–712, 2010.

[82] L.F. Cao, I. Uschmann, F. Zamponi, T. Kämpfer, A. Fuhrmann, E. Förster, A. Höll, R. Redmer, S. Toleikis, T. Tschentscher, et al. Space-time characterization of laser plasma interactions in the warm dense matter regime. *Laser and Particle Beams*, 25:239–244, 5 2007.

[83] G. Nomarski. Microinterféromètre différentiel à ondes polarisées. *Journal de Physique et le Radium*, 16(7):S9–S13, 1955.

[84] R. Benattar, C. Popovics, and R. Sigel. Polarized light interferometer for laser fusion studies. *Review of Scientific Instruments*, 50(12):1583–1586, 1979.

[85] V. Hilbert, C. Rödel, G. Brenner, T. Döppner, S. Düsterer, S. Dziarzhytski, L. Fletcher, E. Förster, S. H. Glenzer, M. Harmand, et al. Spatio-temporal coherence of free-electron laser radiation in the extreme ultraviolet determined by a michelson interferometer. *Applied Physics Letters*, 105(10):101102, 2014.

[86] R. Mitzner, B. Siemer, M. Neeb, T. Noll, F. Siewert, S. Roling, M. Rutkowski, A.A. Sorokin, M. Richter, P. Juranic, et al. Spatio-temporal coherence of free electron laser pulses in the soft x-ray regime. *Optics Express*, 16(24):19909–19919, 2008.

[87] M. Martins, M. Wellhöfer, J. T. Hoeft, W. Wurth, J. Feldhaus, and R. Follath. Monochromator beamline for flash. *Review of Scientific Instruments*, 77(11):115108, 2006.

[88] M. Wellhöfer, M. Martins, W. Wurth, A. A. Sorokin, and M. Richter. Performance of the monochromator beamline at flash. *Journal of Optics A: Pure and Applied Optics*, 9(7):749, 2007.

[89] N. Gerasimova, S. Dziarzhytski, and J. Feldhaus. The monochromator beamline at flash: performance, capabilities and upgrade plans. *Journal of Modern Optics*, 58(16):1480–1485, 2011.

[90] K. Tiedtke, A. Azima, N. Von Bargen, L. Bittner, S. Bonfigt, S. Düsterer, B. Faatz, U. Frühling, M. Gensch, Ch. Gerth, et al. The soft x-ray free-electron laser flash at desy: beamlines, diagnostics and end-stations. *New Journal of Physics*, 11(2):023029, 2009.

[91] H. Petersen. The plane grating and elliptical mirror: A new optical configuration for monochromators. *Optics Communications*, 40(6):402 – 406, 1982.

[92] E. A. Schneidmiller and M. V. Yurkov. Coherence properties of the radiation from flash. *Proceedings of FEL2013, New York, USA*, 2013.

Ehrenwörtliche Erklärung

Ich erkläre hiermit ehrenwörtlich, dass ich die vorliegende Arbeit selbständig, ohne unzulässige Hilfe Dritter und ohne Benutzung anderer als der angegebenen Hilfsmittel und Literatur angefertigt habe. Die aus anderen Quellen direkt oder indirekt übernommenen Daten und Konzepte sind unter Angabe der Quelle gekennzeichnet.

Insbesondere habe ich zur Erstellung der Arbeit nicht die entgeltliche Hilfe von Vermittlungs- bzw. Beratungsdiensten (Promotionsberater oder andere Personen) in Anspruch genommen. Niemand hat von mir unmittelbar oder mittelbar geldwerte Leistungen für Arbeiten erhalten, die im Zusammenhang mit dem Inhalt der vorgelegten Dissertation stehen.

Die Arbeit wurde bisher weder im In- noch im Ausland in gleicher oder ähnlicher Form einer anderen Prüfungsbehörde vorgelegt.

Die geltende Promotionsordnung der Physikalisch-Astronomischen Fakultät ist mir bekannt.

Ich versichere ehrenwörtlich, dass ich nach bestem Wissen die Wahrheit gesagt und nichts verschwiegen habe.

Ort, Datum Vinzenz Hilbert

Danksagung

Mein großer Dank gilt Ulf Zastrau, für die fachlich kompetente und menschlich angenehme Begleitung während meiner Promotionszeit. Außerdem bedanke ich mich für die vielen persönlichen und fachlichen Gespräche und Anregungen, die gemeinsamen aufregenden Experimente an FLASH und SLAC und auch für ein stets offenes Ohr bei Fragen und Problemen.

Ausdrücklich danke ich auch Prof. E. Förster für die Betreuung meiner Promotion und für die warmherzige Aufnahme in die Röntgenoptik Arbeitsgruppe. Auch für die stets konstruktive Kritik und fachlichen Ratschläge möchte ich mich bedanken.

Meinen Kollegen, den Mitarbeitern der Röntgenoptik Arbeitsgruppe, danke ich für die konstruktive und entspannte Zusammenarbeit. Euer Feedback und die stets wohlmeinende Kritik gaben mir Anregungen und Bestätigung. Mein Dank gilt hier besonders: Ingo Uschmann, Sebastian Höfer, Robert Lötzsch, Hendrik Bernhardt, Berit Marx-Glowna, Kai-Sven Schulze, Benjamin Grabinger, Tino Kämpfer, Heike Marschner.

Für finanzielle Unterstützung bedanke ich mich beim BMBF und beim Helmholtz-Institut Jena.

Für die gemeinsame Zeit an DORIS und BESSY danke ich C. Rödel, M. Wünsche, S. Fuchs, A. Blinne.

Für zahlreiche gemeinsame FLASH-Experimente danke ich den Kollegen der Peak-Brightness Collaboration. Mein Dank gilt insbesondere Sven Toleikis, von dem ich viel über den Betrieb eines FEL gelernt habe.

Bei den Mitarbeitern der wissenschaftlichen Werkstätten unter der Leitung von B. Klumbies, P. Hanse und R. Bark, sowie den Konstrukteuren S. Laukner und T. Köhler möchte ich mich für die kollegiale Zusammenarbeit und die exzellente Ausführung bei der Planung und dem Bau der Spektrometer, des Dioden Arrays und des Interferometers bedanken.

S. Ebert, J. Hopfe, J. Brusberg und B. Kirchner danke ich für die stets gute Zusammenarbeit und freundliche Betreuung und Beratung bei organisatorischen Dingen.

Ein besonderer Dank gilt meinen Eltern und Geschwistern, die mich während meines Studiums und meiner Promotionsphase immer wieder unterstützt und ermutigt haben meinen persönlichen Weg zu gehen.
Meinen Freunden danke ich für zahlreiche fröhliche Stunden, heitere und ernste Gespräche und die willkommene Ablenkung, die sie mir so oft bereitet haben. Zuletzt, danke meine liebste Karolin, dass du mir die Zeit so wunderbar versüßt.